Titre: Title:	Theoretical and Experimental Investigation of Near-Field Multi-Focusing Systems
Auteur: Author:	Ruizhi Liu
Date:	2019
Type:	Mémoire ou thèse / Dissertation or Thesis
Référence: Citation:	Liu, R. (2019). Theoretical and Experimental Investigation of Near-Field Multi-Focusing Systems [Thèse de doctorat, Polytechnique Montréal]. PolyPublie. https://publications.polymtl.ca/4060/

Document en libre accès dans PolyPublie
Open Access document in PolyPublie

URL de PolyPublie: PolyPublie URL:	https://publications.polymtl.ca/4060/
Directeurs de recherche: Advisors:	Ke Wu
Programme: Program:	génie électrique

POLYTECHNIQUE MONTRÉAL

affiliée à l'Université de Montréal

Theoretical and experimental investigation of near-field multi-focusing systems

RUIZHI LIU

Département de génie électrique

Thèse présentée en vue de l'obtention du diplôme de *Philosophiæ Doctor*

Génie électrique

Octobre 2019

POLYTECHNIQUE MONTRÉAL

affiliée à l'Université de Montréal

Cette thèse intitulée :

Theoretical and experimental investigation of near-field multi-focusing systems

présentée par **Ruizhi LIU**

en vue de l'obtention du diplôme de *Philosophiæ Doctor*

a été dûment acceptée par le jury d'examen constitué de :

Jean-Jacques LAURIN, président

Ke WU, membre et directeur de recherche

Julien COHEN-ADAD, membre

Ahmed KISHK, membre externe

DEDICATION

To my beloved family.

ACKNOWLEDGEMENTS

RÉSUMÉ

Dans les systèmes de communication modernes, les fonctionnalités d'efficacité énergétique et d'efficacité du spectre sont mises en évidence, attirant de plus en plus l'attention dans la conception des systèmes et des appareils grâce à la demande croissante en débit de données, densité et nombre de terminaux utilisateurs. La technique multi-faisceaux est une caractéristique essentielle de la conception du réseau d'antennes pour systèmes sans fil, qui peut être utilisée pour prendre en charge plusieurs utilisateurs et plusieurs spots avec une grande efficacité. Dans ce travail de recherche, une série de méthodes de développement d'un réseau d'antennes comportant multi-faisceaux de rayonnement électromagnétique dans sa région de champ proche est proposée et présentée. Les travaux de recherche sur la mise au point multiple en champ proche couvrent le développement d'algorithmes, la conception de composants associés, la discussion sur les propriétés de focalisation et leurs méthodes d'amélioration, ainsi que le développement de fonctions d'exploitation et de scénarios d'application.

Dans ce travail, un certain nombre d'algorithmes de modélisation du réseau d'antennes prenant en compte le modèle de champ proche, la compensation de phase et la stratégie d'optimisation sont développés afin non seulement d'identifier les emplacements spatiaux de multiples points focaux dans la région de champ proche, mais également de formuler le modèle de faisceau à ou autour de ces points focaux. Dans l'essentiel, les algorithmes proposés visent essentiellement à réaliser une mise en forme de motif dans la région de champ proche en mettant un accent particulier sur les aspects de conception tels que l'ajustement de la localisation spatiale des points focaux, la spécification des distributions d'amplitude et de phase et l'attribution de polarisations.

La réalisation pratique est également une partie importante de ce travail qui s'intéresse au développement de réseaux d'antennes multi-focales dans la région du champ proche. Par conséquent, les composants, notamment les réseaux d'antennes et les réseaux d'alimentation correspondants, sont conçus et fabriqués pour démontrer expérimentalement les propriétés et les applications à focalisation multiple de ce travail de recherche, validant ainsi la modélisation et l'analyse théoriques. Les réseaux d'antennes multi-focales sont conçus et des travaux expérimentaux sont effectués dans les bandes de fréquences radio et ondes millimétriques avec de bonnes performances.

Différent d'une région d'antenne à champ lointain, le champ électromagnétique dans une région à champ proche implique simultanément des composantes d'énergie réactive et radiative. Pour étudier plus en détail les propriétés du multi-focus dans la région de champ proche, certains paramètres sont définis en relation avec des propriétés de champ spéciales dans la région de champ proche. En particulier, un facteur de réseau d'antennes en champ proche et une résolution de focalisation sont définis et déployés pour estimer la capacité de focalisation d'un réseau d'antennes linéaire ou plan. Des caractéristiques telles que le décalage de focale et l'isolation de polarisation croisée sont examinées et une approche d'amélioration correspondante est donc proposée.

De plus, la fonction de multi-focus est étendue dans ce travail de recherche. Avec les algorithmes proposés, le réseau d'antennes est capable non seulement de se focaliser sur plusieurs points focaux, mais également d'éclairer de multiples zones dans la région de champ proche. Par conséquent, la technique multi-faisceaux proposée est étendue au développement de schémas de traitement de signaux spatiaux comprenant la combinaison de puissance, le fractionnement de puissance et le déphasage. Des techniques populaires telles que la diversité de polarisation peut également être réalisées spatialement avec les solutions développées. Grâce à cette recherche, un ensemble de systèmes à focalisation multiple impliquant le traitement de signal spatial et la fourniture de puissance sont développés, montrant une application prometteuse dans le développement de systèmes de communication hautement efficaces.

ABSTRACT

In modern communications systems, the features of energy efficiency and spectrum efficiency are highlighted, attracting more and more attention in the design of systems and devices thanks to the requirement of ever-increasing data rate, density and quantity of user terminals. Multi-beam technique is an essential enabling design feature of antenna array for wireless systems, which can be used in support of multiple users and multiple spots with high efficiency. In this research work, a series of methods for developing an antenna array that features multiple electromagnetic beaming focuses in its near-field region are proposed and presented. The research work on near-field multi-focus covers the development of algorithms, design of related components, discussion about the focusing properties and their improvement methods, and the expansion of operating functions and application scenarios.

In this work, a number of modeling algorithms of antenna array considering near-field model, phase compensation, and optimization strategy are developed in order not only to identify the spatial locations of multiple focal points in the near-field region but also to formulate the beam pattern at or around those focal points. In essentials, the proposed algorithms aim at realizing a pattern shaping in the near-field region with particular emphasis on design aspects such as adjustment of the spatial location of focal points, specification of amplitude and phase distributions, and allocation of polarizations.

The practical realization is also an important part of this work with interest in developing multi-focus arrays in the near-field region. Therefore, components including antenna arrays and related feeding networks are designed and fabricated for experimentally demonstrating the multi-focusing properties and applications in this research work, which also validate the theoretical modeling and analysis. The multi-focusing antenna arrays are designed, and experimental work is carried out in both radio-frequency and millimeter-wave bands with good performance.

Different from a far-field region of antennas, the electromagnetic field in a near-field region involves reactive and radiative energy components simultaneously. To further investigate the properties of multi-focus in the near-field region, some parameters are defined in connection with special field properties in the near-field region. In particular, near-field array factor and focusing resolution are defined and deployed for estimating the focusing ability of a linear or planar antenna

array. Features such as focal shift and cross-polarization isolation are investigated, and thus a corresponding improving approach is brought about by the proposed algorithms.

Furthermore, the function of multi-focus is extended in this research work. With the proposed algorithms, the antenna array is capable of not only focusing on multiple focal points but also illuminating multiple areas in the near-field region. Therefore, the proposed multi-beam technique is extended to the development of spatial signal processing schemes, including power combining, power splitting and phase-shifting. Popular techniques such as polarization diversity can also be realized spatially with the developed solutions. Through this research, a set of multi-focusing systems involving spatial signal processing and power delivery are developed, showing a promising application in the development of highly efficient communication systems.

TABLE OF CONTENTS

LIST OF TABLES

LIST OF FIGURES

LIST OF SYMBOLS AND ABBREVIATIONS

4G	The fourth generation of broadband cellular network technology
5G	The fifth generation cellular network technology
AF	Array factor
GA	Genetic algorithm
LM	Levenberg-Marquardt algorithm
MIMO	Multiple-input and multiple-output
NF	Near field
NFF	Near-field focus
NFMF	Near-field multi-focus
PSO	Particle swarm optimization
RF	Radio frequency
SIW	Substrate integrated waveguide
SLL	Side-lobe level

CHAPTER 1   INTRODUCTION

1.1 Background

For the fifth generation (5G) wireless communication system, the network is supposed to provide up to ten gigabit-per-second average data transmission rates in support of high-speed datalink, autonomous driving and other applications. As a result, networks and devices should be developed to feature high spectrum efficiency, high energy efficiency, high power capacity and low connection latency, which are essential in fulfilling the ultra-high-speed requirement of 5G networks.

As a key technique in the 4G wireless network, the multiple-input multiple-output (MIMO) scheme has been widely used as it offers multipath transmitting and receiving functions, which ensure its high spectral efficiency [1]. In the 5G wireless system, the concept of MIMO is again continued to be applied by adding multiple antennas in both transmitters and receivers on a much larger scale compared to its 4G counterpart, usually tens or even hundreds of antennas. In this case, the spectral efficiency could be enhanced in a significant manner, which is now named massive MIMO system.

Small cells are introduced as base stations to ensure the capability of handling a high data rate of signal transmission, which commonly includes femtocells, picocells and microcells. They feature low power and high geometrical density to cover the communication in a small area compared with the conventional macro base station. A shorter or even line-of-sight distance between small cells leads to higher capacity of the network. In addition, a combined network of macro base stations and small cells is robust and flexible with high spectral efficiency for a complex environment [2].

In the 5G network, another key problem is energy efficiency, as the fading scenario in an environment would influence the quality of communications a lot. With the help of massive MIMO and small cells, indoor scenarios (line-of-sight or pure environment) are connected to outdoor scenarios (noisy environment with multipath interference) with lower penetration loss. By doing so, the spectral and energy resources can be allocated separately in different scenarios in order to save energy. In view of circuit and source types, millimeter-wave and visible light communication techniques would be considered as suitable solutions.

In all 5G and future wireless communication systems, high spectrum efficiency and high energy efficiency are expected to be two important metrics that are usually used to highlight the requirements related to the scenarios of high data rate and multiple user terminals (Figure 1.1).
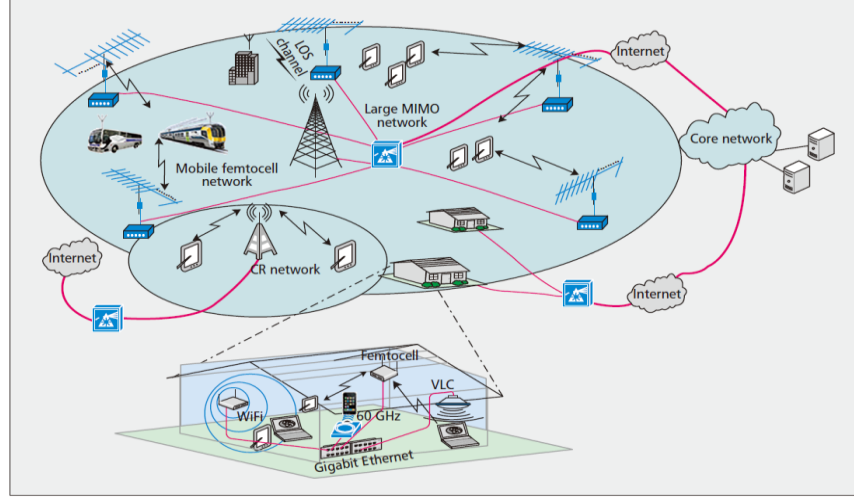
Figure 1.1 Proposed 5G network and key techniques in 5G networks [3]

As a result, proximity or short-range wireless devices and systems have become flourishing thanks to their potential integration with various handheld mobile and flexible or wearable platforms. Therefore, simultaneous wireless power, data transmission and sensing operation within a near-field region may become an indispensable or even a desired choice in support of emerging super-high-speed wireless applications such as 5G and beyond. Depending on the target range and operating wavelength, more signal routing and lower transmission loss can readily be achieved in the Fresnel region (radiative near-field region) compared to the far-field region. In order to increase the power/energy efficiency further and/or to deploy low-loss spatial powering or signal delivery, flexible near-field focusing (NFF) and multi-focus beaming techniques are preferred and should be created.

Similar to the operation of a convex lens used over the visible light band, the power transmission or signal delivery of an antenna array can be concentrated at a focal point or distributed in the area around that point. This can be enabled by the use of an NFF technique. In the NFF technique, a conjugate-phase approach is utilized to designate the phase of an excitation signal for each element in the transmitting array such that the transmitted wave of each antenna is in phase at the focal point [4-6]. Research work related to NFF has been conducted since the last century including the

development of the principles and features of NFF [7-11], the schematic of NFF array based on the conjugate-phase approach and corresponding near-field pattern is displayed in Figure 1.2. The optimization and shaping/synthesis of fields in NFF scenarios have been also considered [12, 13].

(a)   (b)
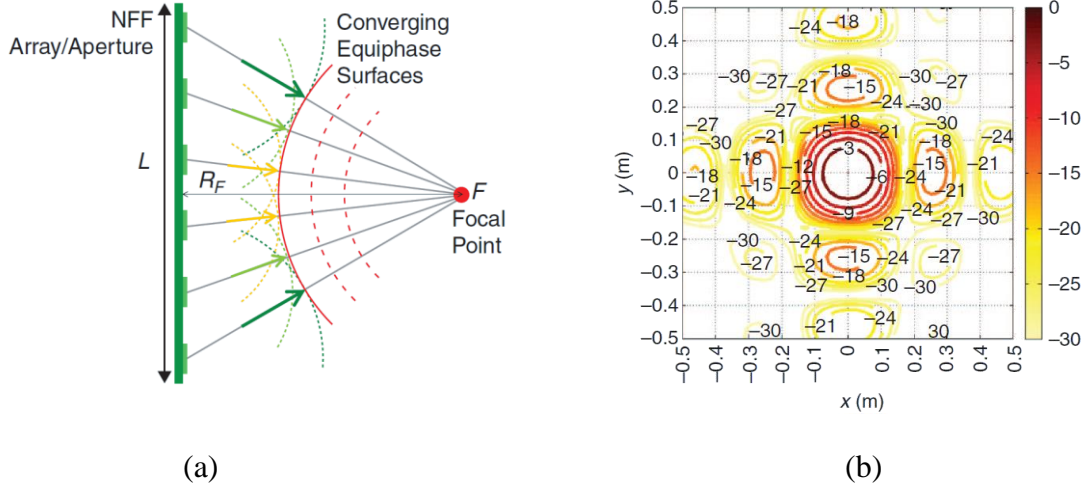
Figure 1.2 NFF technique: (a) planar array for NFF with excitations subjecting to conjugate-phase approach; (b) power pattern in the near-field region realized by an 8×8 NFF array[7]

NFF is known to offer a solution for efficient power transfer, communication and imaging in a short range. Moreover, a near-field technique is now evolving to what should support multiple targets at random locations and/or serves as a wireless power transfer of multiple devices. By assigning an appropriate condition of excitation related to amplitude and phase for each antenna in an array, the resulting antenna array is able to exhibit multiple focal points in a near-field region. This phenomenon is called near-field multi-focus (NFMF), which may provide an alternative approach to the classical power/signal combining and splitting through physically-connected transmission lines. It also offers a solution for the communications of small cells in the case of multi-users. By applying this technique, power/signals from transmitters are concentrated at multiple focal points or areas instead of radiating to the entire space.
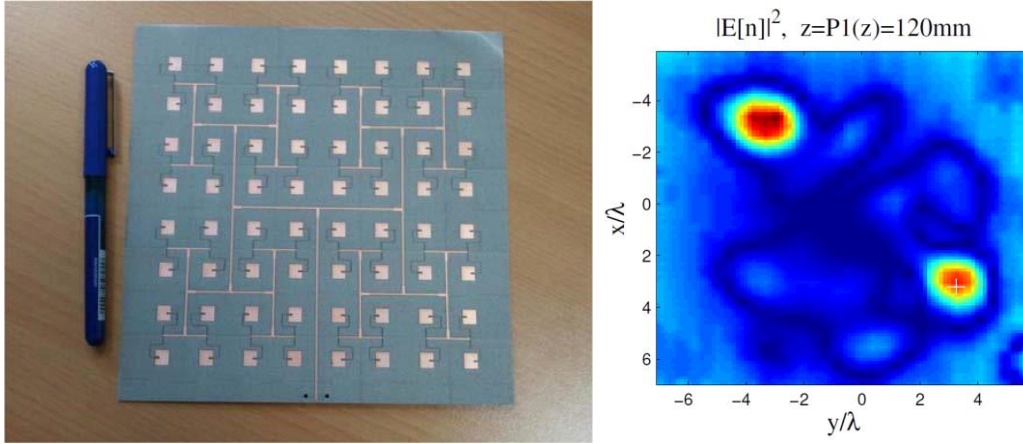
Figure 1.3 8×8 NFMF array (12 GHz) based on numerical algorithm and its corresponding near-field pattern with a focal distance of 4.8λ (120mm) [14]

Earlier works have been carried out about NFMF concerning the focusing algorithm, optimization method, field model, RF front-end and related circuits. Ayestarán et al. realized the focusing of two points with a planar antenna array [14-17], whose prototype and corresponding near-field pattern are shown in Figure 1.3. Feeding weights for amplitude and phase were introduced to define the excitation condition of each antenna. Levenberg-Marquardt algorithm was used for optimizing the values of those weights in order to achieve the desired focusing status. Furthermore, the mutual coupling between antennas was taken into account with neural networks [18, 19]. By employing a coupling matrix in the weight evaluating process, the accuracy of the model and values of excitation can be enhanced. Cheng et al. concentrated on designing the RF front-end design of NFMF, and their leaky-wave antenna is able to accomplish the sweeping beam in the near-field region with continuously varied operating frequency [20]. Not only the antenna array but also the lens placed before the antennas can change the focusing status. Hassan et al. developed a porous dielectric lens for changing the phase condition in the near-field region [21], a symmetrical beam with angle of 40 degrees in both near-field and far-field was successfully proposed and realized.

Previous research work was mainly focusing on defining the spatial locations of multi-focus points, while some key features of multi-focus were merely mentioned such as focal width, focal shift, focusing resolution, polarization, amplitude and phase distribution, and so on. In addition, the algorithms for NFMF are numerical-solution-based, whose computational speed mainly relies on the convergence speed of the optimization method adopted. As a result, the previous solutions are

suitable for NFMF with fixed locations. Functions such as multiple beam tilting and multi-target tracing are hardly realized because the numerical solution is not fast enough.

1.2 Research objectives and methodologies

With the above-mentioned background work in mind, a method for NFMF is proposed and demonstrated in this research work. The method of designing a multi-focus antenna array is developed and improved in different aspects. It is detailed and validated in the thesis through both theoretical and experimental approaches.

The first goal is the development of an analytical algorithm for NFMF. The computational speed of the numerical algorithm adopted in the previous works is mainly constrained by the convergence rate of iteration in the optimization method, which is not suitable for circumstances with multiple movable focal targets or with a large number of focal points. In this work, an analytical algorithm will be developed, which features high computational efficiency.

The second goal is the expansion of focusing abilities. In conventional works, NFMF is only valid at several discrete points in the Fresnel region. While in this work, a large number of focal points can be defined by the proposed method. Moreover, a focusing phenomenon on multiple continuous regions with regular or irregular shapes is exploited and investigated, which performs as a pattern shaping in the near-field region.

The third goal is the understanding and exploitation of unique geometrical features in NFMF. Different from NFF patterns, an NFMF pattern has some unique geometrical features due to the coexistence of multiple focal points. For example, the focusing resolution is defined in NFMF to clarify the minimum spacing between two adjacent focuses that are distinguishable from each other. The relationship between the scale of a near-field antenna array and its corresponding resolution is investigated in this work. Interesting technical features such as focal depth and focal width of NFMF are explored too.

The last goal of this work is related to some concrete applications of NFMF. As NFMF is able to perform pattern shaping, the applications can be expected in many ways such as power combining or splitting, energy delivery and allocation, signal processing, and polarization diversity. These

applications are accomplished in a spatial way, and they are promising for a wide range of system and device applications such as 5G networks.

The framework of this research description through this thesis is arranged as follows.

In Chapter 2, the fundamental theories for developing NFMF antenna arrays are introduced and investigated. Near-field antenna and corresponding field model are studied for analytical estimation of field behavior of the proposed NFMF arrays. Subsequently, the conjugate-phase approach is formulated and improved with a superposition theorem, which serves as the foundation for the proposed analytical algorithm. Furthermore, the concept of near-field array factor is introduced, and then the focusing resolution is developed with the help of a near-field array factor to estimate the proper array scale for a specified NFMF condition. Finally, the procedure of designing an NFMF antenna array is developed and discussed.

In Chapter 3, the NFMF method is further developed by introducing the tuning factor for each antenna element. By introducing the element-based tuning factors, not only locations, but also amplitude and phase of each focal point can be specified with a semi-analytical algorithm with the help of iterative optimization method. With this improved method, the field distribution can be specified on or around the focal points. Array and corresponding microstrip-line based circuits are designed and tested in X-band for demonstration purposes.

In Chapter 4, the function of NFMF arrays is further extended by introducing a pattern based tuning vector. Different from the element-based tuning, pattern-based tuning can be achieved without adopting any optimization method. As a result, the pattern-based tuning algorithm can deal with NFMF having a large number of focal points with a rapid computational speed. With this algorithm, the antenna array is able to focus on not only discrete points, but also continuous regions with specified shapes as an ability of near-field pattern shaping. This feature provides a foundation for accomplishing many circuit and system functions such as power combing, power splitting and signal processing in the near-field region, which is discussed and demonstrated theoretically and experimentally in this thesis.

In Chapter 5, the NFMF method is improved with a function of polarization diversity. In the conventional NFMF method, the antenna array is identically polarized and all the focal points share the same polarization. In this chapter, an algorithm for polarization allocation on multiple focal

points or regions is formulated. Furthermore, cross-polarization isolation of each focal point or region can be controlled by the proposed method. Corresponding dual-polarized array and SIW based circuit are designed and fabricated for demonstration purpose in millimeter-wave band.

In Chapter 6, the research work is concluded, current issues and future work are discussed to appreciate the tremendous values and potential impacts of this research.

CHAPTER 2   THEORY OF NEAR-FIELD ARRAY FOR MULTI-FOCUS

The behavior of antenna arrays is generally determined by their antenna elements. To develop the multi-focus antenna arrays in the near-field region, the properties of an antenna near-field and corresponding model are introduced in this chapter. Furthermore, an analytical algorithm is developed for NFMF, and the procedure of designing an NFMF array is discussed.

2.1 Antenna near field

2.1.1 Near field

Antenna near-field (reactive and Fresnel) region and far-field (Fraunhofer) region are the regions around antenna which are defined by distance. For an antenna or array physically larger than a half-wavelength with maximum geometrical length D, its far-field region is defined with distance $r \geq 2D^2/\lambda$, and the reactive region is located in a range of $r \leq 0.62\left(D^3/\lambda\right)^{1/2}$, while the Fresnel region is defined as the space between them [22] (Figure 2.1).
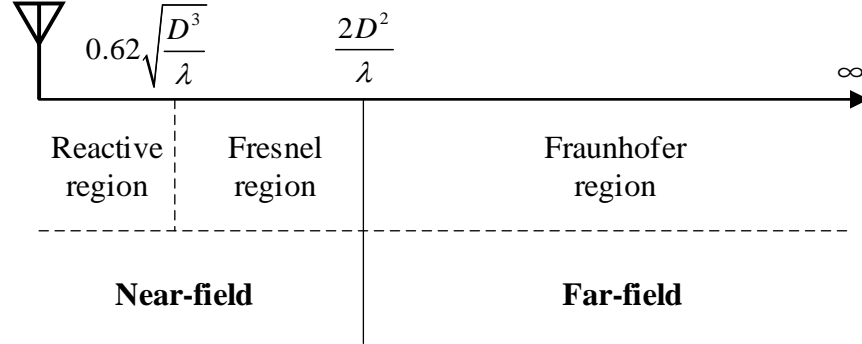
Figure 2.1 Near-field and far-field region of antenna.

In conventional research, performances like pattern and polarization are investigated in connection with the far-field regions as antennas are mainly applied as part of transmitters or receivers with a relatively long distance from the originating radiation source. However, the field property in the near-field region is different from that in the far-field region.

First of all, we need to highlight that when an antenna is utilized within the near-field region, the nature of electromagnetic waves it transmits is different from that in the far-field region. With the

help of a Wilcox expansion [23], the space-expanding electromagnetic waves generated from a source of radiation can generally be expressed by [24]

$$\mathbf{E}(\mathbf{r}) = \frac{e^{-jkr}}{r} \sum_{i=0}^{\infty} \frac{\mathbf{A}_i(\theta,\phi)}{r^i}$$
$$\mathbf{H}(\mathbf{r}) = \frac{e^{-jkr}}{r} \sum_{i=0}^{\infty} \frac{\mathbf{B}_i(\theta,\phi)}{r^i}$$

(2.1)

The above equations cover the entire space around an antenna in question including near-field and far-field regions. It can be observed that in the near-field region the electromagnetic field is formulated as a function of the combination of $1/r^i$ ($i = 1,\ldots\infty$). While in the far-field region, high-order terms of $1/r$ can be neglected with increasing r, which can be simplified as

$$\mathbf{E}(\mathbf{r}) = \frac{e^{-jkr}\mathbf{A}_0(\theta,\phi)}{r}$$
$$\mathbf{H}(\mathbf{r}) = \frac{e^{-jkr}\mathbf{B}_0(\theta,\phi)}{r}$$

(2.2)

The above-described equation is coincident with the classical expression of antenna fields for the far-field region. The difference in expression between the near-field and far-field regions is caused by the different types of energy that these two regions accommodate. In the far-field region, only radiative energy takes place. However, in the near-field region, there exist both radiative energy and reactive energy simultaneously. The higher-order terms of $1/r$ stand for the reactive energy that is maintained or transmitted inside the near-field region. As the distance goes far and far away from the antenna, the reactive energy becomes weaker and weaker. Therefore, only radiative energy exists in the far-field region. However, to estimate or evaluate the field behavior in the near-field region, both reactive and radiative energy should be taken into consideration.

On the other hand, the transmission mode in the near-field region is different from that in the far-field region. In the far-field region, the electromagnetic wave radiates with a TEM mode as there are no longitudinal electric and magnetic components (in the propagation direction) with a boundary condition of free space. However, in the near-field region, the modal behavior is quite astonishing because of reactive energy. By solving the Wilcox expression with spherical harmonics, the electromagnetic waves can be expressed with both TE_r and TM_r modes in the near-field region as follows [24]:

$$\text{TE}_{\text{lm}} \text{ mode} \equiv \begin{cases} \mathbf{r} \cdot \mathbf{H}_{lm}^{TE} = a_E\left(l,m\right)\frac{l(l+1)}{k}h_l^{(1)}\left(kr\right)Y_{lm}\left(\theta,\phi\right) \\ \mathbf{r} \cdot \mathbf{E}_{lm}^{TE} = 0 \end{cases}$$

$$\text{TM}_{\text{lm}} \text{ mode} \equiv \begin{cases} \mathbf{r} \cdot \mathbf{E}_{lm}^{TE} = a_M\left(l,m\right)\frac{l(l+1)}{k}h_l^{(1)}\left(kr\right)Y_{lm}\left(\theta,\phi\right) \\ \mathbf{r} \cdot \mathbf{H}_{lm}^{TE} = 0 \end{cases} \quad (2.3)$$

The equations (2.3) define the transmission modes in the near-field region with spherical Hankel functions. Waves in the near-field region are transmitted with TE_r, TM_r modes or a combination of them as the longitudinal field component exists due to the reactive field in this region [24, 25].

In the end, the behavior of electromagnetic waves in the near-field region is different from those in the far-field region. Therefore, the behavior of electromagnetic fields in the near-field region cannot be evaluated by the conventional approach deployed for the far-field region.

2.1.2 Near-field models

Specific models or methods need to be introduced for the field evaluation related to the near-field region. As a classical approach, the dyadic Green function theorem makes use of the current distribution of antenna to calculate the E-field in the near-field region [26, 27]. Another approach is the use of a far-field-to-near-field (FF-NF) transformation method [24], combining the Wilcox expansion with antenna radiation pattern in the far-field, E-field in the near-field region can then be derived. With reference to each other, the dyadic Green function theorem is used to derive the fields from the source while the FF-NF transformation method relies on the far-field. Both of them require a massive data acquisition to ensure the accuracy of the finally derived fields.

In the previous works, the concept of equivalent source model was adopted in predicting and estimating of the field behavior, which accomplished near-field-to-far-field transformation [28, 29], also some applications in the area of antenna measurement [30, 31]. In order to accelerate the field calculation process while maintaining an excellent accuracy, an infinitesimal dipole equivalent model [32, 33] is studied and adopted as the antenna near-field model in this work. The main idea of this equivalent method is to synthesize a specific radiation pattern of a single antenna with a cluster of infinitesimal dipoles. It combines the background thoughts of the dyadic Green function and the FF-NF transformation method altogether. With regard to the aspect of a current source, an infinitesimal dipole antenna has a simple current distribution, by which a quasi-analytical closed-

form expression of field distribution in both near- and far-field regions can be provided in a concise manner. With regards to radiation pattern, an arbitrary form of antenna can be equivalently thought of as a group of infinitesimal electric or magnetic dipoles or their combinations. Previous researches point out that, the entire field in the exterior region of an antenna can be completely determined from the radiation pattern [23], and a given far-field radiation pattern of antenna can be used to estimate its near-field field distribution except the field close to the source with evanescent modes [24, 27].
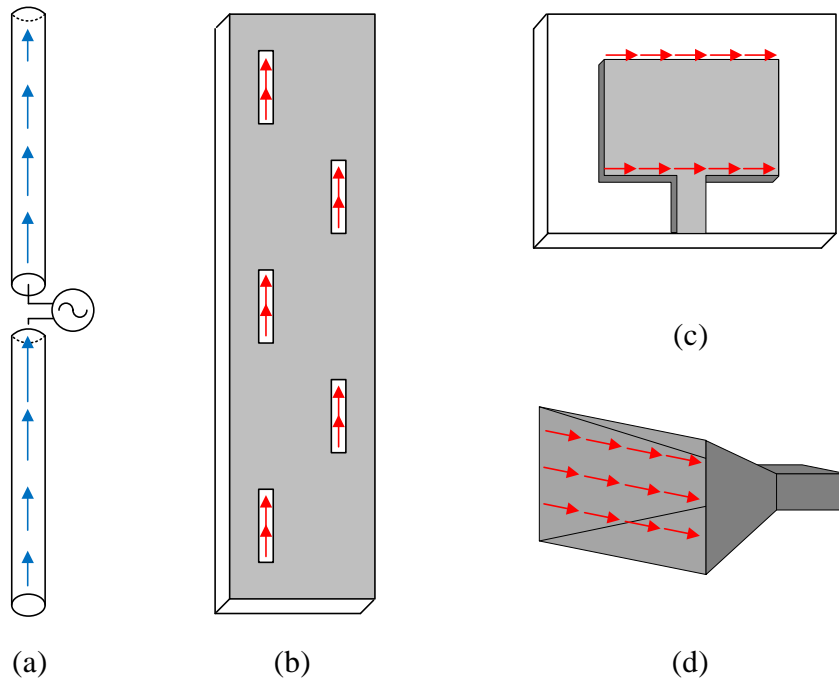
Figure 2.2 Infinitesimal dipole equivalent models for different types of antennas (blue arrows represent infinitesimal electric dipoles, and red arrows represent infinitesimal magnetic dipoles): (a) half-wave dipole; (b) leaky-wave antenna; (c) patch antenna; (d) horn antenna.

For a conventional antenna with a regular shape, the basic forms of an equivalent model based on electric or magnetic infinitesimal dipoles can be predefined. Figure 2.2 shows some models for typical antennas. Dipoles such as half-wave dipole and broadband dipoles or monopoles can be treated as a cluster of infinitesimal electric dipoles, while the slot antenna, horn antenna, leaky-wave antenna and patch antenna can be represented by infinitesimal magnetic dipole as their apertures are mainly slots.

Following the creation of an initial equivalent model, parameters of infinitesimal dipoles such as location, and excitation status and so on require optimization to fit with the radiation pattern of a target antenna. With the optimized parameters, the E-field pattern of an antenna can be written as

$$\mathbf{E}(\mathbf{r}) = \sum_{p=1}^{P} A^{p} \mathbf{E}_{\mathbf{E}}(\mathbf{r_p}) + \sum_{q=1}^{Q} A^{q} \mathbf{E}_{\mathbf{M}}(\mathbf{r_q}),$$ (2.4)

where P and Q are the total numbers of infinitesimal electric and magnetic dipoles defined in the equivalent model, respectively. The number and location of the infinitesimal dipoles are determined by the antenna type and its current distribution. In addition, the parameters such as location, amplitude and phase of infinitesimal dipoles adopted are to be optimized to get an accurate model of the selected antenna. $\mathbf{r_p}$ and $\mathbf{r_q}$ stand for the vectors pointing form infinitesimal dipoles to target point. $\mathbf{E_E}$ ($\mathbf{E_M}$) represents the general E-field of the infinitesimal electric (magnetic) dipoles that are valid for either estimated near-field or synthesized far-field as

$$\mathbf{E}_{\mathbf{E}} = \frac{e^{-jkr}}{4\pi\varepsilon_0} \left\{ \frac{k^2}{r}(\mathbf{n}\times\mathbf{p})\times\mathbf{n} + \left(\frac{1}{r^3} + \frac{jk}{r^2}\right)\left[3\mathbf{n}(\mathbf{n}\cdot\mathbf{p}) - \mathbf{p}\right] \right\}$$

$$\mathbf{E}_{\mathbf{M}} = -Z_o \frac{e^{-jkr}}{4\pi} \frac{k^2}{r}(\mathbf{n}\times\mathbf{m})\left(1 + \frac{1}{jkr}\right)$$ (2.5)

where $\mathbf{n}$ is the unit vector pointing to target point; $\mathbf{p}$ and $\mathbf{m}$ are the electric and magnetic dipole moment, respectively; Z_0 stands for the impedance of free space, and k is the wavenumber.

The detailed procedure of building such an infinitesimal dipole model is shown in Figure 2.3. Let's consider the patch antenna in Figure 2.4(a) as an example. The antenna is located at the center of Cartesian coordinate with its broadside pointing to negative x-direction. This antenna is represented by a 5×2 array of infinitesimal magnetic dipoles which are located at the edges perpendicular to the polarization direction. As mentioned above, the near-field pattern can be estimated by a given far-field pattern. As a result, we can optimize the location, the amplitude and phase of the infinitesimal dipoles to fit with the far-field result of the target antenna obtained by full-wave simulations or experimental tests in order to generate the near-field model of the chosen antenna element.
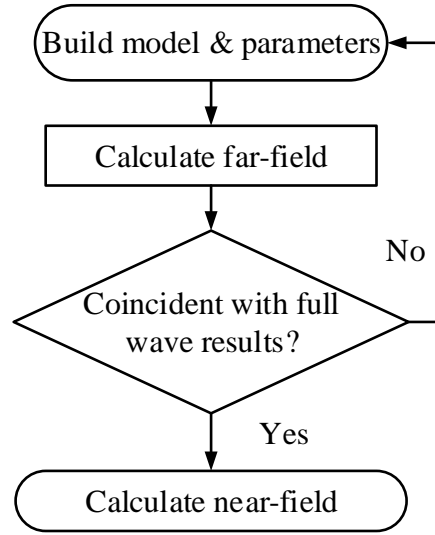
Figure 2.3 Procedure for building an infinitesimal dipole equivalent model for near-field estimation.
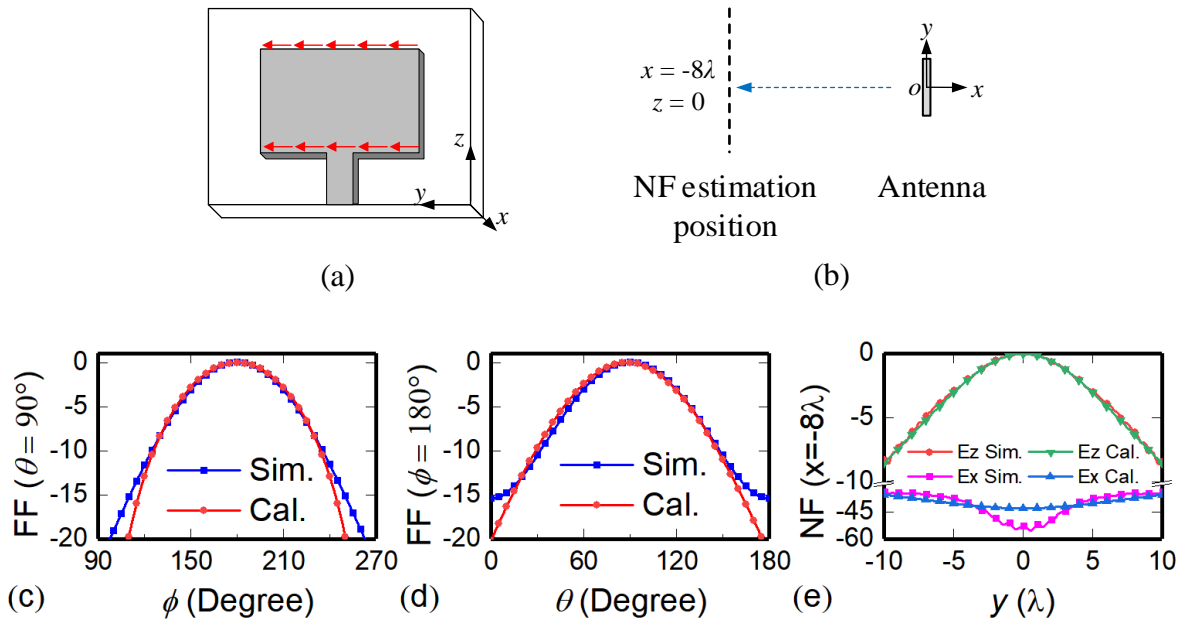
Figure 2.4 Patch antenna and the corresponding infinitesimal dipole model: (a) configuration of infinitesimal dipoles; (b) position for near-field estimation; (c) far-field results on plane $\theta = 90°$; (d) far-field results on plane $\phi = 180°$; (e) near-field estimation ($x = -8\lambda$, $z = 0$)

Figure 2.4 (c) and (d) show the full-wave simulation-based far-field of the antenna and the fitting results of its equivalent model. With the optimized equivalent model, the near-field distribution on

estimation position (Figure 2.4(b)) of the equivalent model is calculated and compared with the full-wave simulation-based near-field of the antenna element in Figure 2.4(e), which shows an agreement between each other with a minor difference.

As mentioned above, the equivalent model adopted for the patch antenna is composed of two group of infinitesimal magnetic dipoles, which represent the ideal case of the patch antenna. While the practical patch would introduce cross-polarization and other radiation caused by finite ground, which leads to the difference between simulated and calculation results. The accuracy of this model can be further improved when introducing more infinitesimal dipoles in the equivalent model [34]. With the near-field equivalent model, we can now calculate fields at certain locations through the quasi-analytical equation discussed above instead of time-consuming full-wave simulations.

2.2 Near-field multi-focus

The physical focusing of transmitted energy by a cluster of antennas is a field interference phenomenon in nature. Physically alternating constructive or destructive interferences can define specific areas with increased or decreased wave/field strength. Furthermore, the antenna array with designated amplitude and phase conditions can form a specified or wanted interference pattern at certain locations in an open space. In order to converge the maximum power at one specified point in the near-field region, a conjugate-phase approach was utilized to designate the phase of an excitation signal for each element in the array [4-6].

In the conjugate-phase approach, the antenna array is composed of N identical elements (Figure 2.5). All the elements are excited with identical amplitude, while the phases of excitations are different for the convergence purpose, which obeys the rule of "conjugate-phase". Electromagnetic wave transmitted from n_{th} antenna to a certain focal point has a phase delay of $-kl_n$, where k is the wavenumber and l_n is the geometrical distance from the n_{th} antenna to the focal point. To make sure that waves from all the elements are converged at the specified focal point with the maximum power level, the waves should be superimposed with an in-phase condition. The in-phase condition can be artificially created by applying conjugate-phase $\varphi_n = kl_n$ ($n = 1, 2\ldots N$) as the phase of excitation. This conjugate-phase compensates the phase difference at the focal point introduced by different positions of antennas, so it serves as the principal design technique for an NFF antenna array having single focal point.

However, in some application cases like multi-target communication and wireless power supply, a designed NFF array may be required to yield two or more focal points for which the conjugate-phase approach is no longer applicable because it is only capable of accounting for one focal point.
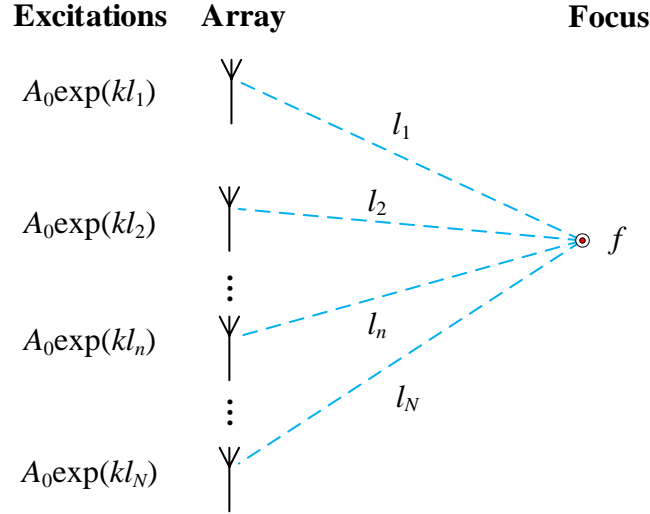
Figure 2.5 Schematic of *N*-element near-field array focusing at point *f* with excitations obeying the conjugate-phase approach.

To realize a multi-focusing function of an antenna array, one should extend the conjugate-phase approach. For instance, the antenna array in Figure 2.6 is constructed to focus at f_1 and f_2 simultaneously. When the conjugate-phase approach is used for each standalone case, the proposed array is able to focus on single point as shown in (a) or (b). We can notice if the two focal points are located at the side-lobe region of each other. According to the superposition theorem, we can superimpose the two groups of excitation $\left\{A_0 e^{\varphi_{11}}, \cdots, A_0 e^{\varphi_{14}}\right\}$ and $\left\{A_0 e^{\varphi_{21}}, \cdots, A_0 e^{\varphi_{24}}\right\}$, this combined excitation $\left\{A_0\left(e^{\varphi_{11}} + e^{\varphi_{21}}\right), \cdots, A_0\left(e^{\varphi_{14}} + e^{\varphi_{24}}\right)\right\}$ is capable of generating two patterns with a superimposed status and yield the dual-focusing results simultaneously in (c).

The proposed method is also applicable to the case of multiple focal points. For *N* elements array with *M* focal points, the phase compensation for element *n* corresponding to focus *m* is

$$\varphi_{mn} = k\sqrt{\left(x_m - x_n\right)^2 + \left(y_m - y_n\right)^2 + \left(z_m - z_n\right)^2} \,. \tag{2.6}$$

By calculating (2.6), M groups of excitations are obtained for the antenna array. Taking the normalized amplitude into account, the excitation signal for each antenna is defined by

$$I_n = A_0 \sum_{m=1}^{M} \exp\left(j\varphi_{mn} \right). \tag{2.7}$$
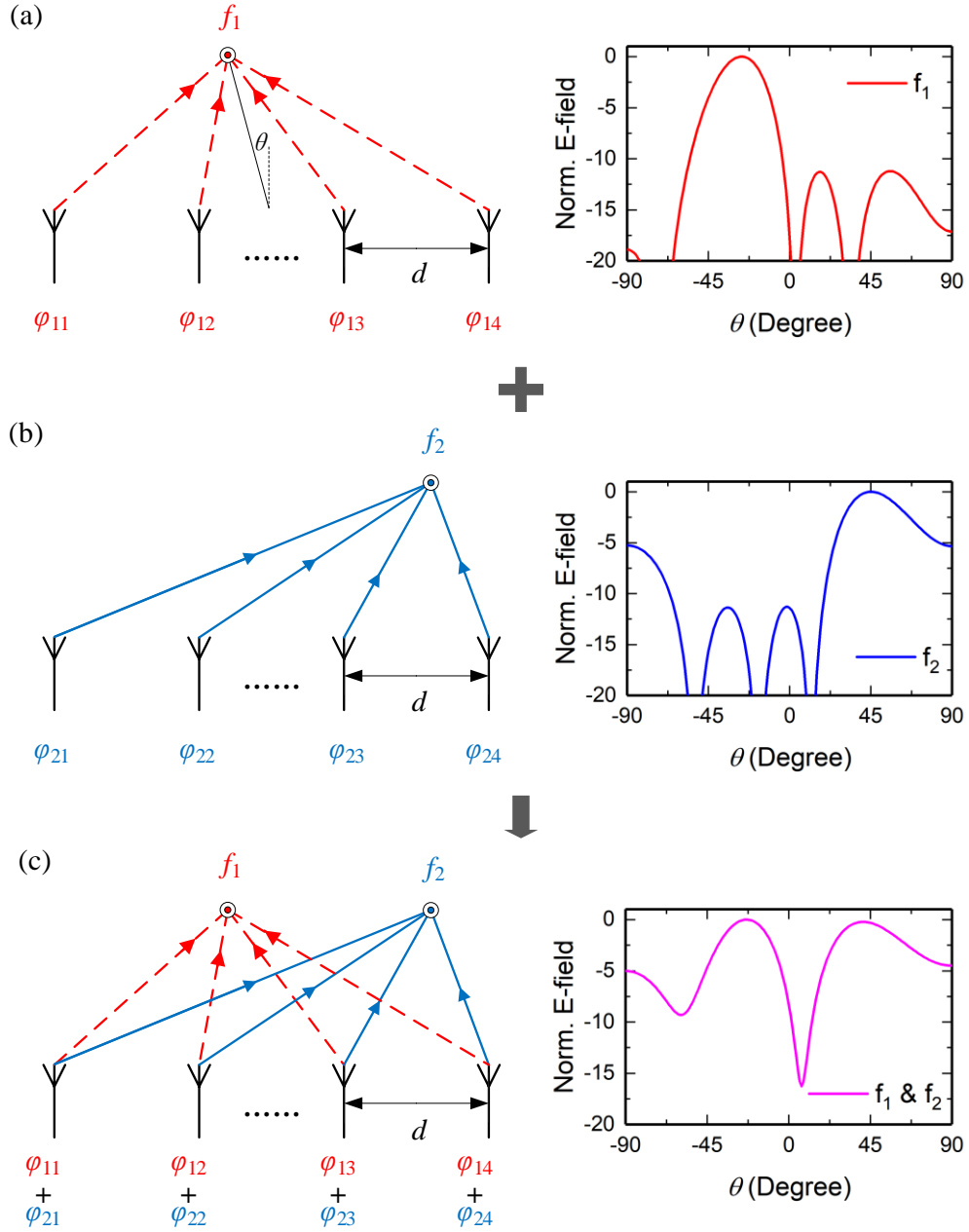
Figure 2.6 Near-field focusing cases: (a) focusing on standalone focal point f_1; (b) focusing on standalone focal point f_2; (c) focusing on focal point f_1 and f_2 simultaneously.

With the above excitations, the field distribution in a near-field region can be written as

$$\mathbf{E}(\mathbf{r}) = \sum_{n=1}^{N} \mathbf{E}(\mathbf{r_n}) I_n \,,$$

(2.8)

where $\mathbf{r_n} = (x - x_n, y - y_n, z - z_n)$. We can see that E-field is calculated for the near-field region where the nature of electromagnetic waves is different from that in the far-field region. The E-field of each antenna can be expressed with the quasi-analytical infinitesimal dipole model as discussed earlier. As a result, the total E-field pattern for NFMF can be written as

$$\mathbf{E}(\mathbf{r}) = \sum_{n=1}^{N} I_n \left[\sum_{p=1}^{P} A^p \mathbf{E_E}(\mathbf{r_p}) + \sum_{q=1}^{Q} A^q \mathbf{E_M}(\mathbf{r_q}) \right].$$

(2.9)

With this equation, the near-field distribution of the antenna array can be formulated for multiple focal points at the target location. The proposed method can realize a multi-focusing feature with designated excitation I_n ($n = 1, 2\dots N$) based on the improved conjugate-phase approach presented above. The infinitesimal dipole equivalent model is adopted for a quasi-analytical near-field expression. As the quasi-analytical expression of an infinitesimal dipole field is known, the estimation of the array's near-field is fast, and the accuracy of the near-field pattern is determined by its equivalent model.

2.3 Focusing properties

The proposed method above offers an analytical derivation of excitations and an estimation of near-field, which targets two or more multi-focus points in the near-field region. While the properties of multi-focusing features rely not only on the excitations but also on the configuration of antenna array itself, such as the width of focal point, resolution, side lobe level etc. which are directly influenced by the array form. Therefore, the relationship between the configuration of the antenna array and the focusing properties will be discussed in this section.

In conventional research works, the antenna is located in a 2D plane with rectangular lattice [4-6, 35-38] as it is convenient to design, calculate and manufacture, and some properties of NFF are investigated and discussed [10, 11]. To simplify the calculation process, antenna elements in the

NFMF antenna array discussed in this work are equally spaced with a linear or rectangular lattice form. With this topology, some typical features will be discussed below.

2.3.1 Near-field array factor

Array factor (AF) is a common tool widely used in estimating the behavior or function of an array utilized in the far-field region as it can represent the general properties of an array with certain configuration and excitation condition. Furthermore, AF serves as an outline in designing the process of a far-field array. As the basic assumption of employing the AF, the array element is omnidirectional and the fields emitted by the array obey the superposition principle. Electromagnetic waves in the Fresnel region share the same properties in superposition as those in the Fraunhofer region even though the energy in the Fresnel region is composed of both radiative and reactive ones. Therefore, in the Fresnel region, the concept of AF is also valid as an index for generally estimating the transmitting features such as main lobe direction, side-lobe level (SLL), beamwidth etc. regardless of the type of element in the near-field array.

In this section, we employ a "near-field AF" as a guiding parameter for designing an NFMF array governed by the proposed method.
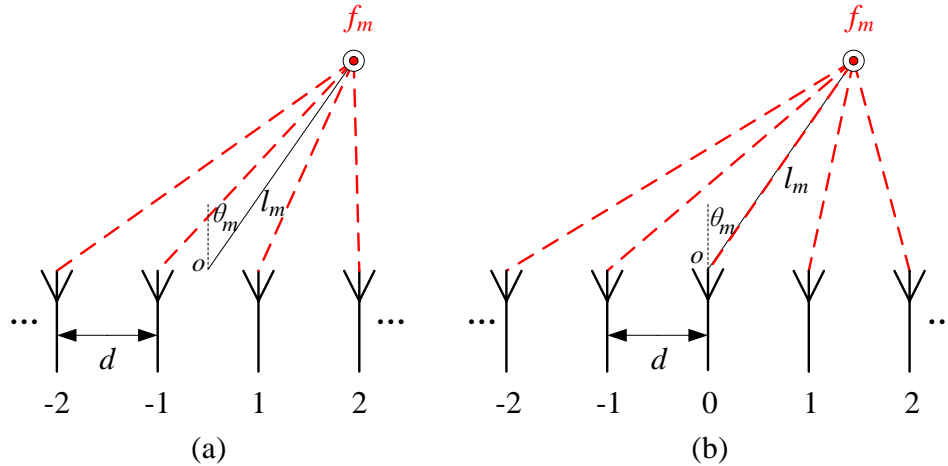
Figure 2.7 N-element linear antenna array focusing at focal point f_m with: (a) even number of antennas; (b) odd number of antennas.

To study the AF of an NFMF array, a linear N-elements array with equal spacing d serves as a typical example here. First of all, let us consider the case of m_{th} focal point with a position of (l_m,

θ_m) as described in Figure 2.7. Using the conjugate-phase approach, the excitation phase of element n is

$$\begin{aligned}\varphi_{omn} &= k\sqrt{l_m^2 + (nd)^2 - 2nl_md\sin\theta_m}\ (N\ odd)\\\varphi_{emn} &= k\sqrt{l_m^2 + \left(\frac{2n-1}{2}d\right)^2 - (2n-1)l_md\sin\theta_m}\ (N\ even)\end{aligned} \tag{2.10}$$

Assuming each element in the array shares the same normalized amplitude, i.e. $A_0{=}1$, we can obtain the AF for the proposed array with the superimposed fields

$$AF_m = \begin{cases}\displaystyle\sum_{-(N-1)/2}^{(N-1)/2} e^{-jk\sqrt{l_m^2+(nd)^2-2nl_md\sin\theta}+j\varphi_{omn}}\ (N\ odd)\\[2em]\displaystyle\sum_{-N/2+1}^{N/2} e^{-jk\sqrt{l_m^2+\left(\frac{2n-1}{2}d\right)^2-(2n-1)l_md\sin\theta}+j\varphi_{emn}}\ (N\ even)\end{cases} \tag{2.11}$$

By employing the Taylor series of first order $\sqrt{1+x}\approx 1+x/2$ with the condition of $l_m > Nd$ (which results in a maximum error of 2% in calculating the AF), where most of the radiative near-field region is considered, and the AF can be simplified as

$$AF_m = \frac{\sin\left(\dfrac{N\psi_m}{2}\right)}{\sin\left(\dfrac{\psi_m}{2}\right)}, \tag{2.12}$$

where $\psi_m = kd(\sin\theta - \sin\theta_m)$. According to the superposition theorem, the general AF for a multi-focusing case

$$AF = \sum_{m=1}^{M} \frac{\sin\left(\dfrac{N\psi_m}{2}\right)}{\sin\left(\dfrac{\psi_m}{2}\right)}. \tag{2.13}$$

It is worthwhile to mention that approximations and assumptions are applied during the derivation of AF in (2.12) and (2.13) with a Taylor expansion in order to obtain a general analytical solution with concise expressions. The reason is that the above near-field AF serves as an approximate reference for deriving the required minimum scale of an antenna array for corresponding multi-

focus conditions in the following part. Therefore, one should refer to the accurate expression (2.9) in evaluating the exact near-field pattern or field distribution instead of considering the near-field AF.

It can also be noticed that the near-field AF derived above has a similar form as the conventional AF applied in the far-field region. However, they are different physically. The far-field AF is defined to calculate the only focal direction while the near-field AF is defined to estimate the focal point including both direction and distance simultaneously. Furthermore, the usage of them is also different. The AF for the far-field is used for calculating a far-field pattern of antenna array while the near-field AF derived above is adopted for estimating the scale of near-field antenna array. As a result, the near-field AF is specified for a near-field focus and cannot be applied to a far-field array even though they share a similar form.

2.3.2 Focusing resolution

With the above-described general near-field AF, we can investigate and estimate the properties of antenna array such as the geometrical parameters of antenna array for NFMF.
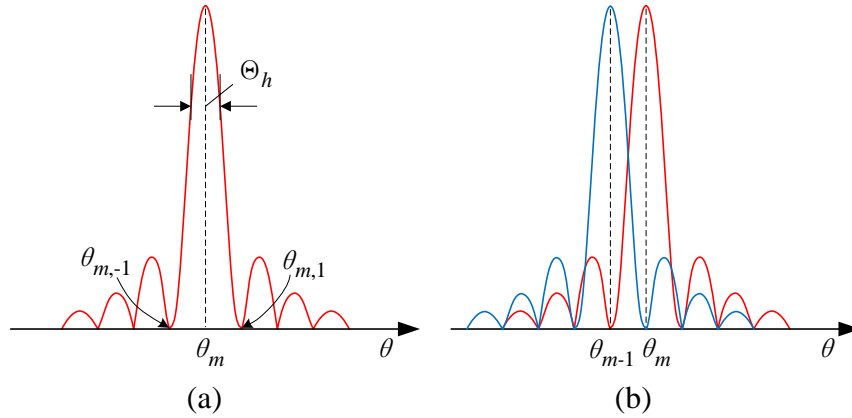
Figure 2.8 AF of antenna array: (a) case of focusing at single focal point; (b) case of focusing at multiple focal points with minimum distance.

For an antenna array with a high transmitting efficiency, the side-lobe or grating lobes should be prevented by adjusting the geometrical parameters of antenna array (Figure 2.8). Considering the case of a single focal point by solving (2.12), we can derive the peak(s) occurring at the direction

$$\theta = \arcsin\left(\frac{2u\pi}{kd} + \sin\theta_m\right)(u \in \mathbb{Z}). \tag{2.14}$$

We impose the AF to have only one peak that occurs at θ_m in the region $\theta \in \left[-\pi/2, \pi/2\right]$ to prevent the grating lobes. Under the circumstance of $u = 0$, and each nonzero u that cannot yield valid θ, we can then derive the range of distance between elements in an array by (2.14) as follows,

$$d \le \max\left(\frac{\lambda}{1 - \sin\theta_m}\right) = \frac{\lambda}{2}. \tag{2.15}$$

Subsequently, we can come to the conclusion that in order to acquire NFF or NFMF in the half-space, the maximum distance d_{max} between neighboring antennas of an array should not be larger than a half free-space wavelength at operating frequency. Meanwhile, the spacing between elements also influences the mutual coupling effect between antennas. In order to reduce the coupling, antennas should be placed far away from each other. Therefore, a distance of half wavelength is mainly adopted as the spacing between antennas in this work.

The near-field AF derived above represents a general focusing property for multi-focus cases. Therefore, the concentrating level around each focal point in the case of NFMF can also be manifested. In the cases of a multi-focus development, depth of focus [7] is defined as the range between locations with -3-dB suppression around focal point along the broadside direction of antenna array; while focal width [7] is the corresponding -3-dB range along the direction parallel to antenna array. According to the expression of the derived near-field AF, it can estimate the trend of focal width at a focal plane for the multi-focus. By solving (2.12), we can derive Θ_h as the parameter representing the size of focal spot in one dimension of a general array with certain numbers of elements. As a result, the focal width of near-field array is positively correlated with Θ_h

$$\text{focal width} \propto \Theta_h = \sum \arcsin\left(\pm\sin\theta_m + \frac{2.782}{kNd}\right). \tag{2.16}$$

This means that the focal width can be controlled by the number of antennas in each row or column in an array with fixed element spacing d. This suggests that a larger array scale should lead to narrower focal width and more concentrated transmitting energy.

As the NFMF feature is obtained by superimposing multiple near-field patterns, one cannot distinguish the two focal points if they are too close to each other. From (2.12), we know that the first zero-crossing response occurs at

$$\theta_{m,\pm1} = \arcsin\left(\pm\frac{2\pi}{kNd} + \sin\theta_m\right). \tag{2.17}$$

In order to minimize the interference between the focal points, the focal point should be located at least away from the first zero-crossing region (Figure 2.8). Thus, we can obtain the minimum spacing between the focal points, i.e. the focusing resolution over the focal plane is

$$R = \max\left\{l_m\cos\theta_m\tan\left[\sin^{-1}\left(\frac{2\pi}{kNd}\pm\sin\theta_m\right)\right]\mp l_m\sin\theta_m\right\}. \tag{2.18}$$

The resolution defined above represents that of a one-dimensional condition, and the minimum spacing is defined as a line segment parallel to the linear array. For a two-dimensional case, the resolution should be calculated in two orthogonal directions according to the arrangement of antenna array. There are four main parameters that influence the focusing resolution R, including l_m, θ_m, N and d. In order to prevent grating lobes as discussed in the last part, d is fixed as a constant. In Figure 2.9(a), θ_m is fixed to be at 0 degree, and the focusing resolution of array with a different number of antennas is displayed. We can draw the conclusion that when more antennas are included in the array, the minimum spacing decreases, i.e. the focusing resolution can be improved by increasing the scale of array. Moreover, the focusing resolution could be better if the focal point is closer to the antenna array.

A similar conclusion can be drawn from Figure 2.9(b). In this figure, the focal plane is located at $x = -8\lambda$ (array locates along yoz plane and faces negative x-direction) in order to detect the influence of θ_m. On one hand, the multi-focusing features are achieved in part of the space which is determined by the scale of antenna array N. For example, an array with four antennas can cover 96º, while an array with eight antennas can cover 120º, which is 25% wider than the former one. As a result, more antennas are employed and the NFMF will be realized in a wider space. On the other hand, with a fix scale N, the focusing resolution gets the best results when a focal point is located at $\theta_m = 0º$, which is just facing the center of antenna array.

The AF derived above can serve as a qualitative guidance of arranging the array geometry and roughly estimate the focusing resolution of NFMF. This is because the above derivation is based on the general case in spite of a specific type of antenna and field distribution in the discussion.

It worth mentioning that, the mention of deriving resolution R is generating a guideline for designing an NFMF array. Through R, we can estimate the multi-focus ability of an existing array. Meanwhile, with the function (2.18), we can use a proper number of antennas to design an NF array with specified multi-focus features to prevent wasting materials, space and energy of system.
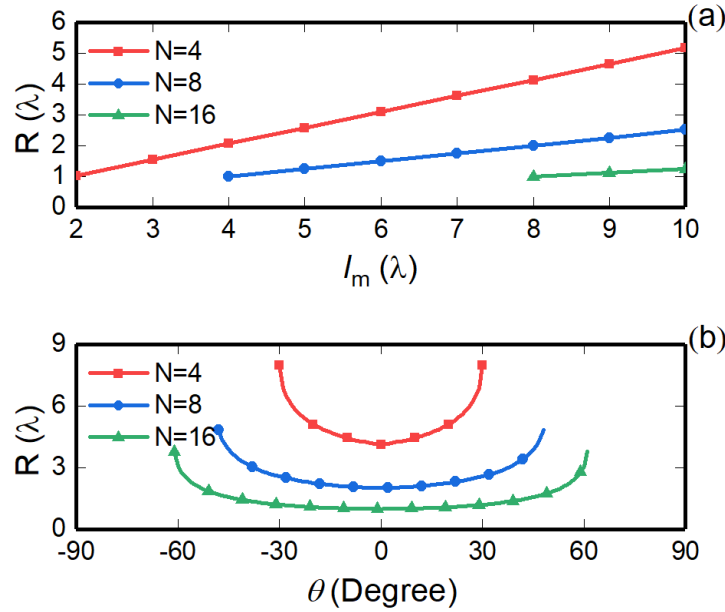
Figure 2.9 N-element linear array: (a) $\theta_m = 0$, relationship between focusing resolution R and l_m; (b) focal plane $x = -8\lambda$, relationship between R and θ_m.

2.4 Design procedure

According to the theoretical derivation, an analytical algorithm for NFMF and its corresponding properties are presented earlier in this chapter. Therefore, we take a planar array as an example to describe the general procedure of the proposed method, which is displayed in Figure 2.10. Referring to this narrative flow chart, steps are described in detail with a practical example, which we adopt in the following demonstration process in this section.

Step 1: The first step is to select a coordinate system according to the requirement of practical applications, then to assign multiple focal points on target locations in the near-field region. In this

demonstration, we adopt the Cartesian coordinate shown in Figure 2.11, where the focal points are located in the -*x* half-space.

Step 2: The second step is the selection of an antenna type among dipole, slot, horn, patch and irregular antennas in accordance with the requirement of polarization and focus width etc. In order to demonstrate the features of the proposed method in a large angular range, we choose the rectangular patch as the elements of antenna array. In Figure 2.11(a), the patch antenna is allocated at *yoz* plane with a polarization along *z*-axis, facing the negative *x*-direction.
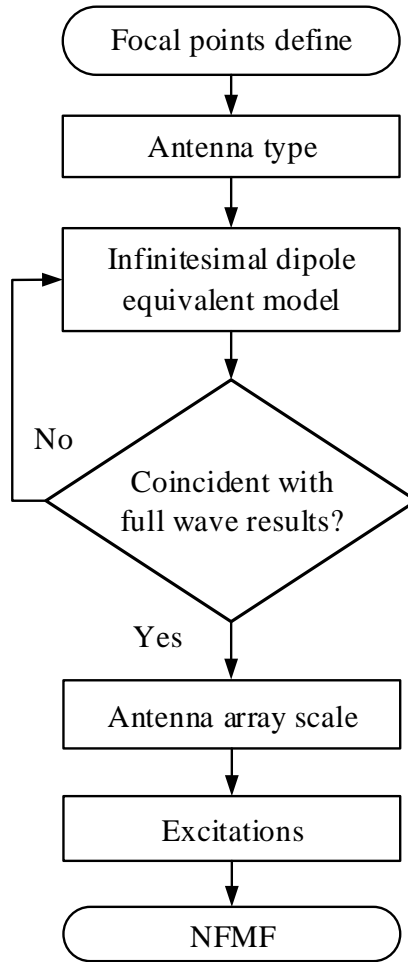
Figure 2.10 General procedure of the proposed NFMF method.

Step 3: Subsequent to the determination of the antenna type, we build the infinitesimal dipole equivalent model of a single antenna with the FF-NF transformation method discussed in section 2.2. The initial guess of the model is based on the physical type of the antenna, and the spatial

locations, amplitude and phase of each infinitesimal dipole serve as the degrees of freedom with the purpose of fitting.

Step 4: The target antenna needs to be simulated with a full-wave methodology or tested to yield the far-field pattern of co-polarization and cross-polarization. As the infinitesimal model is able to calculate both far-field and near-field model, the degrees of freedom mentioned in step 3 are adjusted to make sure that the calculated and simulated far-field patterns are coincident with each other with certain tolerance. As discussed in section 2.1, the equivalent model of target antenna is established for near-field pattern estimation with high accuracy.

Step 5: Once the single element and its infinitesimal dipole equivalent model are determined, the scale of antenna array suitable for the multi-focus circumstance needs to be estimated. As discussed in section 2.3, the scale of antenna is mainly determined by distance l_m, direction θ_m, spacing R and number M of the focal points. With the equations in section 2.3, we can come up with a suitable topology of the antenna array. In this example, we make use of the rectangular lattice form of the planar array with distance $d = \lambda/2$ arranged in both row and column, which is shown in Figure 2.11(b).

(a)   (b)
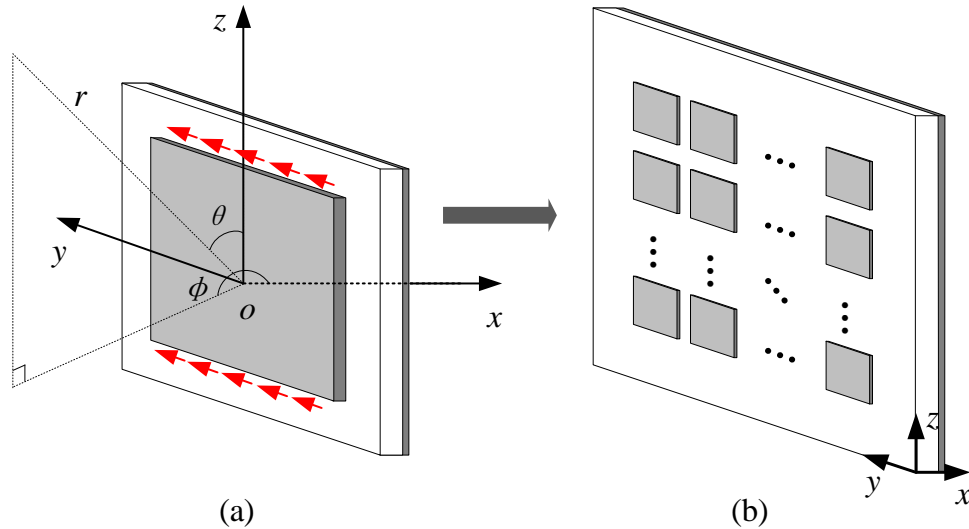
Figure 2.11 Configuration of antenna and array: (a) patch antenna element and the corresponding infinitesimal dipole equivalent model; (b) rectangular lattice array composed of patch antennas for NFMF.

Step 6: As the coordinate of each element in the array is determined, we can use the proposed excitation estimation function (2.7) to derive the values of excitations for all the array elements. The antenna fed by such a state forms a near-field pattern at the locations of predefined focal points.

Step 7: With the excitation obtained, we can derive the near-field pattern of the antenna array and also gain insight into the targeted NFMF features by (2.9). Antenna array with such NFMF features and the corresponding feeding networks can be designed and applied for practical use.

2.5 Examples of NFMF array

To demonstrate the proposed NFMF methods and the corresponding properties, some examples in different conditions are given below.

2.5.1 Matrix-form NFMF

This example is concerned with the focal points distributed in the form of a matrix. The focal points here are located with a shape of 2×4 matrix on $x = -4\lambda$ plane, which is shown in Figure 2.12. The coordinates of the focal points have a spacing of 2λ on y-axis and 1.5λ on z-axis.
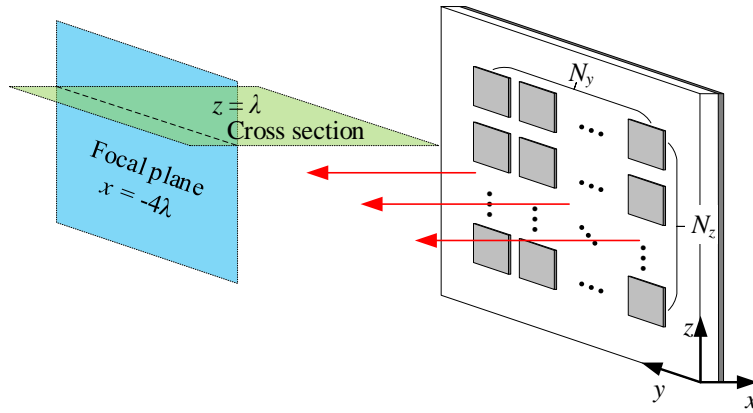
Figure 2.12 Configuration of transmitting antenna array on *yoz* plane and focal plane on *yz*-plane.

According to the focusing resolution function formulated in (2.18), the minimum number of elements in the y-direction $N_{y,min} = 12$ and in the z-direction $N_{z,min} = 12$. To compare the focusing performances between antenna arrays with a different number of elements, pattern of each case is calculated by (2.9) and displayed in Figure 2.13.

Calculation results in Figure 2.13(a) and (b) show the normalized E-field distribution on $x = -4\lambda$ plane ($N_y < N_{y,min}$, $N_z = N_{z,min}$), where the focal points along the y-direction cannot be clearly distinguished especially those centrally located ones. The second case is related to an array with the minimum number of elements in both directions ($N_y = N_{y,min}$, $N_z = N_{z,min}$), which is shown in Figure 2.13 (c) and (d). In this case, the focal points can be clearly distinguished. However, the offset of the outer focal points is larger than the centrally located ones, which is caused by the interference introduced by the superposition of excitation sets. To yield a better focusing resolution, more elements are needed in the y-direction in the third case ($N_y > N_{y,min}$, $N_z = N_{z,min}$). The offset of all focal points becomes smaller and the side-lobe is also reduced, which are shown in Figure 2.13(e) and (f).
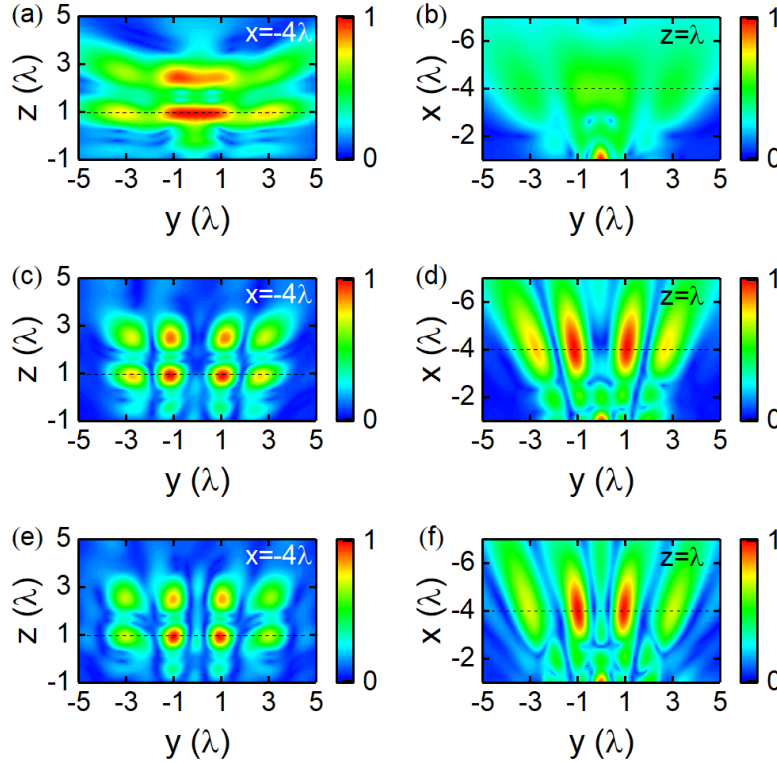
Figure 2.13 Normalized E-field distribution of NFMF on focal plane $x = -4\lambda$ and cross section $z = \lambda$, respectively: (a) & (b) $N_y = 7 < N_{y,min}$, $N_z = 12$; (c) & (d) $N_y = 12 = N_{y,min}$, $N_z = 12$; (e) & (f) $N_y = 16 > N_{y,min}$, $N_z = 12$.

With the above-discussed three cases, we can conclude that in order to realize an NFMF, the minimum number of elements $N_{i,min}$ ($i = x, y, z$) in each direction needs to be satisfied. For higher

accuracy of focusing location and lower side-lobe, the scale of antenna array N_i needs to be enlarged according to the requirements.

2.5.2 Unequally spaced NFMF

In the last example, the spacing between the focal points is the same along the y- or z-direction. To further demonstrate the proposed algorithm, one case where the focal points with an unequal spacing in the y- or z-direction is presented in this section.
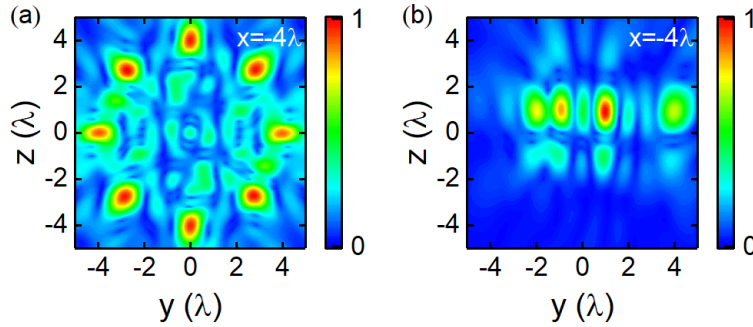
Figure 2.14 Normalized E-field distribution of NFMF on focal plane $x = -4\lambda$: (a) circularly distributed focal points; (b) linearly distributed focal points.

In the first example, 8 focal points are uniformly distributed on a circle (radius $r = 4\lambda$) on $x = -4\lambda$ plane (Figure 2.14), which leads to an unequal spacing along the y- or z-axis. The coordinates are listed in Table 2.1. According to the focusing resolution function (2.18), $N_{y,min} = N_{z,min} = 16$. The field distribution on focal plane $x = -4\lambda$ and cross section $z = 0$ plane is shown in Figure 2.14(a). With the minimum number of elements adopted in two dimensions, the array could achieve the distribution with a displacement of focal points $(\Delta y, \Delta z)$ in Table 2.1 with a 0.06λ variance.

Another example is related to a group of linearly distributed focal points with increasing spacing from negative y- to y-direction, which is described in Table 2.1. The minimum number of elements in the y-direction is 13. In order to get a lower SLL (Figure 2.14(b)), 16 elements are employed here with a 0.06λ variance of displacement.

From the above examples, we can conclude that with certain quantities of elements, the antenna array can achieve an NFMF with specified locations and spacing.

Table 2.1 Unequal spaced NFMF on $x = -4$ (unit: λ)

Circular case					
Preset (y, z)		(-4, 0)	(-2.8, 2.8)	(0, 4)	(2.8, 2.8)
		(4, 0)	(2.8, -2.8)	(0, -4)	(-2.8, -2.8)
N_y, N_z	Var.	Offset (Δy, Δz)			
16, 16	0.06	(0, 0)	(0.1, -0.1)	(0, 0)	(0, -0.1)
		(0, 0)	(-0.1, 0.1)	(0, 0)	(0, -0.1)
Linear case					
Preset (y, z)		(-2, 1)	(-1, 1)	(1, 1)	(4, 1)
N_y, N_z	Var.	Offset (Δy, Δz)			
16, 8	0.06	(0, 0)	(0.1, 0)	(0, -0.1)	(0, -0.1)

2.6 Conclusion

In this chapter, the theory for designing an antenna array with NFMF features is proposed, studied and demonstrated, which leads to the development of a new design method. The principle of the proposed method is concerned with improved conjugate-phase approach and superposition theorem, by which the multi-focusing features on specified locations in the near-field region can be obtained efficiently without resorting to a large-scale iterative optimization process. The method also introduces an infinitesimal dipole equivalent model for antenna element, which augments the accuracy of the array model and at the same time maintains the fast calculations as it avoids tedious full-wave simulations. As a result, this method is promising for a real-time tracing in the near-field cases because of its rapid processing.

Focusing features including resolution and minimum scale of the array for specified targets are discussed, which gives out a guideline for designing an NFMF array with reasonable resources. Multi-focusing with different forms of geometrical distribution illustrates that the proposed method is adequate for various situations.

CHAPTER 3   ELEMENT TUNING-BASED NFMF ARRAY

According to the discussion in the previous chapter, an antenna array for NFMF can be realized theoretically by the above-mentioned analytical algorithm based on the formulated conjugate-phase approach and principle of superposition. However, this simple algorithm lacks the ability of dealing with NFMF with specified electrical and spatial requirements on multiple targets. In this chapter, an element tuning-based algorithm and corresponding design method are developed and demonstrated for designing NFMF array with specified amplitude and phase requirements.

3.1   Element tuning-based algorithm for NFMF

The method discussed in Chapter 2 yields a rapid analytical solution for the multiple focal points with specified locations. While it may come across some issues, for example, it cannot simultaneously specify amplitude and/or phase condition at or around the multiple focal points, meanwhile it may cause a focal shift at the same time. In order to shape the fields in a near-field region and achieve the specified amplitude and phase conditions around the focal points with high efficiency and energy-concentrating characteristics, we improve the proposed method further by introducing one additional degree of freedom to equation (2.7) and the corresponding optimization process in the assigned excitations for antenna elements in a near-field array as

$$I'_n = A_n \sum_{m=1}^{M} \exp\left(j\varphi_{mn} \right). \tag{3.1}$$

In this equation, we replace the normalized amplitude A_0 by tuning factors A_1, A_2 … A_N, which means that the amplitude for each antenna element in an array can be defined independently by these tuning factors. Then the corresponding field distribution in the near-field region is

$$\mathbf{E}\left(\mathbf{r} \right) = \sum_{n=1}^{N} \mathbf{E}\left(\mathbf{r_n} \right) I'_n. \tag{3.2}$$

And the field transmitted by each element $\mathbf{E}(\mathbf{r_n})$ can be derived with the help of infinitesimal dipole model discussed in the last chapter with equation (2.4). By adjusting the values of those tuning factors, the excitation of each element is redefined, and the corresponding field distribution around the focal points can also be changed. Furthermore, we can assign specified amplitude, phase or

field distribution around the focal points and achieve the exact excitations by optimizing the tuning array with a iterative optimization algorithm.

The improved method based on (3.1) presents a number of advantages. On one hand, compared with an analytical solution (see (2.9)) of excitations, the improved version is definitely more flexible, which is able to adjust the fields around the focal points to achieve a special requirement of field distribution. On the other hand, the improved method combines the analytical solution and optimization process together. Therefore, we can optimize the tuning factors with an array of initial value $A_1 = A_2 = \ldots = A_N = C$, where the field is already concentrated at focal points. Under this circumstance, we can get a rapid convergence as the locations of focal points are determined by the initial status, so the optimization targets are only related to the amplitude and phase conditions of certain targets or around. Meanwhile, the scale of optimized parameters is relatively small, as we only need to optimize the amplitude of excitations instead of amplitude and phase together when we compare with the conventional numerical solution, which is another main factor for rapid convergence. In addition, the near-field antenna's equivalent model adopted here offers accurate and fast field estimation without resorting to full-wave simulations, which also accelerates the iteration process of optimization.

The popular iterative optimization methods for solving the field distribution include the Levenberg-Marquardt (LM) algorithm, particle swarm optimization (PSO), and genetic algorithm (GA). These algorithms have different computational features such as convergence rate, optimal solutions etc. Genetic algorithm is adopted as the optimization method in this thesis because of its numerous advantages. First of all, GA is a handy solution as its principle is easy to understand, and it has an integrated library function in popular coding languages such as Matlab. Second, GA is good at solving a problem with multiple parameters that have no clear or analytical relationships with each other. As a variable to be optimized, the amplitude of each antenna A_n has no definitive relationships with each other and GA can offer a large variety of combinations of values to fit the target. As the proposed NFMF method is aiming at real-time focusing and tracing in the near-field region, GA is a good choice thanks to its advantage of rapidity.

The procedure of adopting GA for optimization is listed in Figure 3.1. The first step is related to the initialization of variables to be used for optimization. In our case, amplitudes of antenna A_n ($n = 1, 2 \ldots N$) are defined as the variables with initial values. The second step defines and then

calculates the value of a fitness function. The fitness function is decided by the requirement of a specified case. As the optimization is targeting at the specification of field distribution, amplitude and phase at specified locations can be treated as the optimizing target for defining the fitness function. If the value of the fitness function fulfills the requirement of termination (lower than tolerance), the fitness results are derived. Otherwise, a new generation of variables would be carried out through the process of selection, crossover and mutation and then used for estimation of the fitness function again.
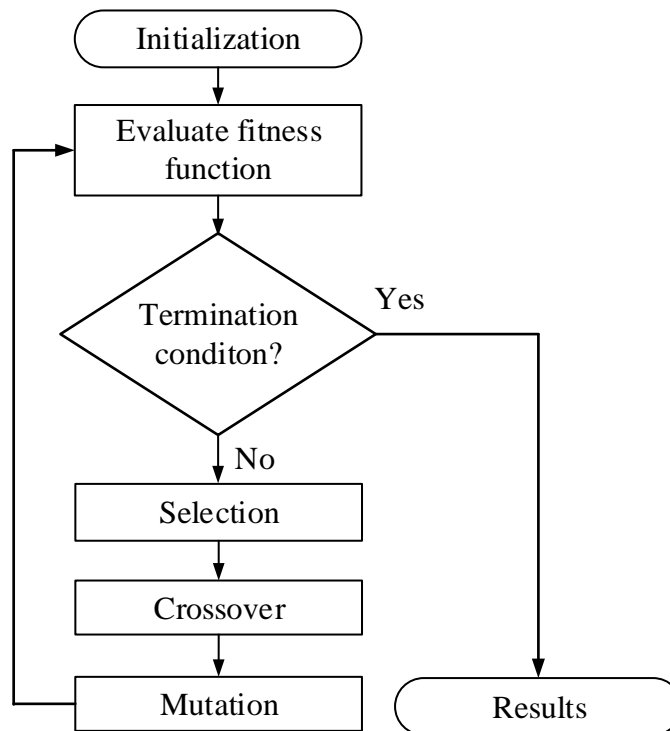
Figure 3.1 Block diagram of a typical genetic algorithm.

With the help of GA, the optimization of the excitations of the array can be realized, which further influences the near-field pattern. The detailed procedure is shown in Figure 3.2. At first, the spatial distribution of focal points needs to be defined. It worth mentioning that the requirements of pattern such as amplitude and (or) phase distribution at or around focal points need to be defined simultaneously as the references for further optimization. For the next step, the antenna type, the near-field model based on infinitesimal dipole equivalent model, and the array scale which is calculated by resolution R are defined, which is similar to the procedure discussed in Chapter 2. Then, the initial excitations with uniform amplitude ($A_1 = A_2 = \ldots = A_N$) and conjugate-phase are

derived in step 3, which serves as the initial values for the optimization. In step 4, the fitness function is defined according to the pattern requirement in step 1 and GA is adopted for optimization of amplitudes of each antenna. For the next steps, when the requirement of pattern is fulfilled with certain tolerance, a group of optimized amplitudes can be derived and then the NFMF pattern can be depicted.

```
┌─────────────────────────┐
│ Focal points & pattern  │
│ requirement define      │
└─────────────────────────┘
            │
            ▼
┌─────────────────────────┐
│ Antenna type/field      │
│ model/array scale       │
└─────────────────────────┘
            │
            ▼
┌─────────────────────────┐
│ Initial excitations     │
└─────────────────────────┘
            │
            ▼
┌─────────────────────────┐
│ GA optimization         │◄──┐
└─────────────────────────┘   │
            │                 │ No
            ▼                 │
      ◇ Coincident with       │
        pattern               │
        requirements? ────────┘
            │
            │ Yes
            ▼
┌─────────────────────────┐
│ Optimized excitations   │
└─────────────────────────┘
            │
            ▼
┌─────────────────────────┐
│ NFMF                    │
└─────────────────────────┘
```
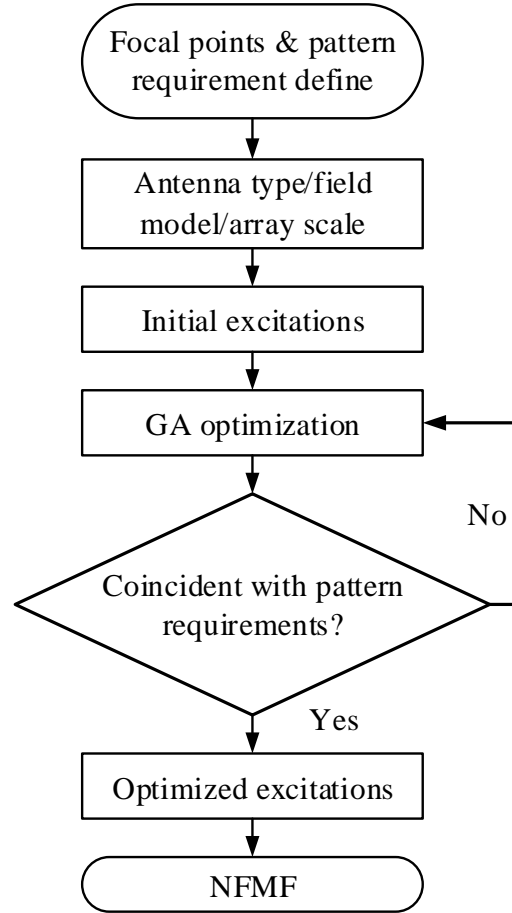
Figure 3.2 Procedure of element tuning-based algorithm for NFMF.

3.2 Focal shift correction

Focal shift is a conventional issue encountered in the research of focusing cases in the near-field region. According to the principle of the conjugate-phase approach, all beams from array are in-phase when they are transmitted to the focal point. This approach ensures the beams would not cancel each other when they superimpose at the focal point. However, the location with maximum power accumulated from all the elements is not exactly located at the focal point. Therefore, the

focal shift indicates the distance from the maximum power point to an actual "in-phase" focal point. In this section, the focal shift of NFMF is investigated, and the method of reducing the focal shift is proposed and developed.

3.2.1 Focal shift and resolution

Different from NFF with a single focal point, the antenna array for NFMF focuses at multiple points simultaneously, and the superimposed patterns influence each other when they are applied together as a single pattern in the near-field region. In this section, the relationship between resolution and focal shift of NFMF is investigated with the help of the definition of focusing resolution R developed in Chapter 2.

To simplifier the following discussion, let us discuss the proposed scheme through an example, which is concerned with the focal points distributed in the form of a matrix. The focal points here are located with a shape of 2×4 matrix on $x = -8\lambda$ plane, which is shown in Figure 3.3. The coordinates of the focal points are listed in Table 3.1, where the spacing between the focal points on the y-axis is 3λ and on the z-axis is 2λ.

Table 3.1 NFMF with matrix form distribution on $x = -8$ (unit: λ)

Preset (y, z)		(-4.5, 3)	(-1.5, 3)	(1.5, 3)	(4.5, 3)
		(-4.5, 1)	(-1.5, 1)	(1.5, 1)	(4.5, 1)
N_y, N_z	Var.	Focal shift (Δy, Δz)			
10, 10	0.49	(0.61, 0.50)	(-0.19, 0.40)	(0.50, 0.53)	(-0.39, 0.51)
		(0.62, -0.51)	(-0.20, -0.61)	(0.39, -0.48)	(-0.50, -0.59)
11, 11	0.22	(-0.09, 0.21)	(-0.18, 0.21)	(0.18, 0.18)	(0.21, 0.22)
		(-0.30, -0.30)	(-0.20, -0.18)	(0.08, -0.29)	(0.30, -0.30)
14, 14	0.09	(0.04, 0.03)	(0.01, 0.10)	(0.11, 0.13)	(0.08, 0.02)
		(-0.13, -0.20)	(0.04, -0.12)	(-0.06, -0.07)	(0.03, -0.19)

According to the focusing resolution function formulated in (2.18), the minimum number of elements in the y-direction $N_{y,min} = 11$ and in the z-direction $N_{z,min} = 11$. To compare the focusing performances among antenna arrays with different number of elements, three cases are calculated with the NFMF method in Chapter 2 without optimization. The results are displayed in Table 3.1.

The first segment of the table is the coordinates of preset focal points. The remaining part of the table is related to the performance of arrays with different scales, the focal shift is calculated on focal plane $x = -8\lambda$ which is parallel to the planar array.
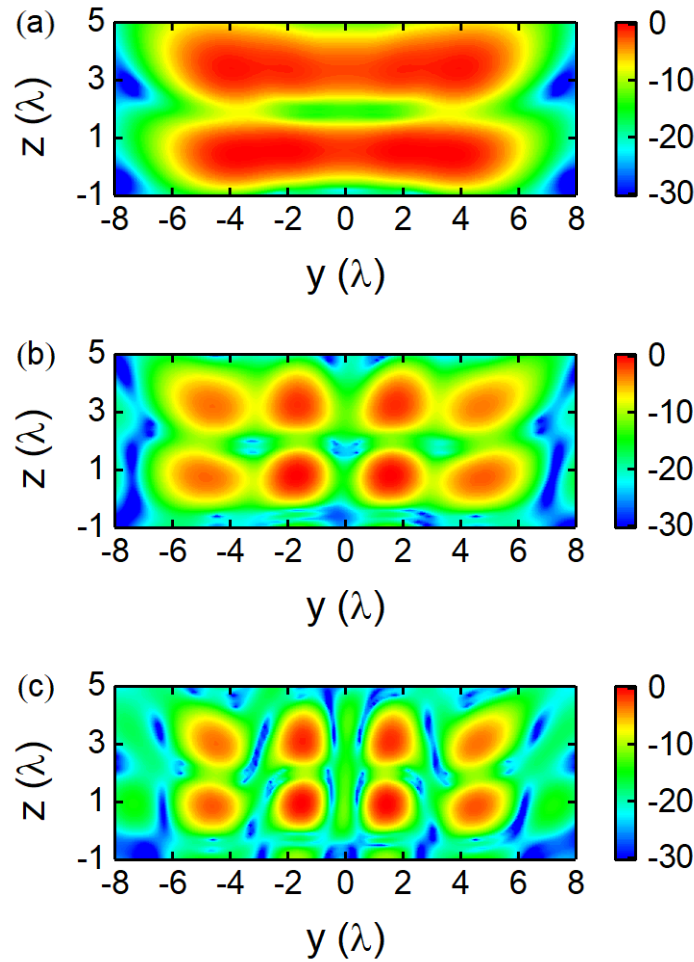
Figure 3.3 Normalized E-field distribution of NFMF on focal plane $x = -8\lambda$: (a) $N_y = N_z = 10$; (b) $N_y = N_z = 11$; (c) $N_y = N_z = 14$.

The first case contains 10 elements in the y- and z-direction, which does not reach the minimum number of elements required ($N_y < N_{y,min}$, $N_z < N_{z,min}$). Calculation results in Figure 3.3(a) show the

normalized E-field distribution on $x = -8\lambda$ plane, where the focal points along the y-direction cannot be clearly distinguished, especially the centrally located ones. The variance of focal shift, in this case, is up to 0.49λ, which is large compared with the spacing between the focal points.

The second case is related to an array with the minimum number of elements in both directions ($N_y = N_{y,min}$, $N_z = N_{z,min}$). In this case, the focal points can be clearly distinguished in Figure 3.3(b). The variance of the focal shift is 0.22λ, which is much smaller than in the previous case. However, the focal shift of the outer focal points is larger than the centrally located ones.

To achieve better multi-focus accuracy, more elements are needed in two directions in the third case ($N_y > N_{y,min}$, $N_z > N_{z,min}$). The field is more concentrated on the focal points with a further reduced focal shift of 0.09. Meanwhile, as the scale of the array goes up, the side-lobe can be suppressed further. The SLL at point (0, 3) is -14.35 dB in Figure 3.3(c), which shows a suppression compared with the same point in Figure 3.3(b) (-12.32 dB).

Therefore, we can conclude that for higher accuracy of multi-focus with lower focal shift, the resolution of antenna array needs to be enlarged according to the requirements.

3.2.2 Correction of multi-focus focal shift

In the last example, the minimum scale of the antenna array can be estimated by the proposed method in Chapter 2 according to the specified multi-focus distribution. Moreover, we can find out that the focal shift in direction parallel to the array plane can be reduced by increasing the number of elements.

It is worthwhile to mention that, with the proposed optimization process, the focal shift of multiple focal points can be corrected simultaneously without increasing the scale of array.

The example here is concerned with the focal shift correction of two points with coordinates of f_1 (-4λ, 0, 0) and f_2 (-4λ, 2λ, 3λ) (see Figure 3.4). With the element tuning-based algorithm, we can specify the amplitude of each focal point, which is the maximum along the spatial vector directing from array center to focal point ($\vec{p}_{f_1} = \hat{x}$ and $\vec{p}_{f_2} = -4\hat{x} + 2\hat{y} + 3\hat{z}$ for f_1 and f_2 respectively in this example). And the corresponding fitness function can be expressed by

$$fitness = \left[\max\left(E_{\vec{p}_{f_1}} \right) - E_{f_1} \right]\left[\max\left(E_{\vec{p}_{f_2}} \right) - E_{f_2} \right] \tag{3.3}$$

When the field values at two focal points approach the maximum value along $\vec{p}_{f_1}$ and $\vec{p}_{f_2}$ respectively, the value of fitness function decreases and approaches zero. Then, the GA optimization is utilized to generate a group of amplitudes corresponding to the minimum value of the fitness function.

As such, the depth of focus which always exists in the conjugate-phase based NFF array can be corrected. At the same time, the amplitudes of two focal points need to be higher than the surroundings on the focal plane x=-4λ to correct the focal shift over the focal plane.
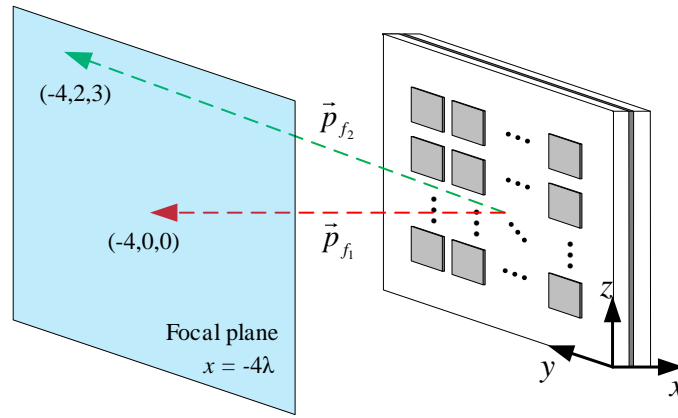
Figure 3.4 Configuration of NFMF array for focal shift correction.

The NFMF array adopted is a 10×10 patch array. The results of field distribution of the initial case (calculated by (2.9) according to the superimposed conjugate phase approach) are shown in Figure 3.5(a) and (c); while the corrected results generated by the optimized method proposed in this chapter (equation (3.1)) are shown in (b) and (c) and compared with the initial case.

On the focal plane parallel to the array plane, we can calculate the focal shift from Table 3.2. For the initial case, Figure 3.5(a) displays that the focal shift is (-0.03λ, -0.06λ) and (-0.10λ, 0.10λ) for two focal points; while that of the optimized case in Figure 3.5(b) is related to (0.02λ, 0.02λ) and (0.04λ, 0.06λ). We can figure out that the focal shift is reduced over the focal plane through the comparison of the results (b) with (a), the optimized case has more accurate focusing at both focal points. In Figure 3.5(c), a normalized E-field along the spatial vector directing from the array center to two focal points as $\vec{p}_{f_1} = \hat{x}$ for f_1 and $\vec{p}_{f_2} = -4\hat{x} + 2\hat{y} + 3\hat{z}$ for f_2 is shown for both initial and optimized cases. We find out that the two maximum points for the initial case have an offset

compared with $x=-4\lambda$, which is a common phenomenon in the NFF circumstance. With the optimization process we proposed, the focal shift along the transmitting direction is reduced for both focal points simultaneously. The optimization also contributes to good SLL suppression. The SLL is -6.79 dB in the initial case. While in the optimization case, it is suppressed to -9.07 dB.

We can conclude that the focal shift of multiple focuses can be corrected with the help of the element tuning-based algorithm from both transmitting direction and its orthogonal direction simultaneously, i.e. the element tuning-based algorithm has the capability of shaping the near-field pattern on or around multiple focal points.
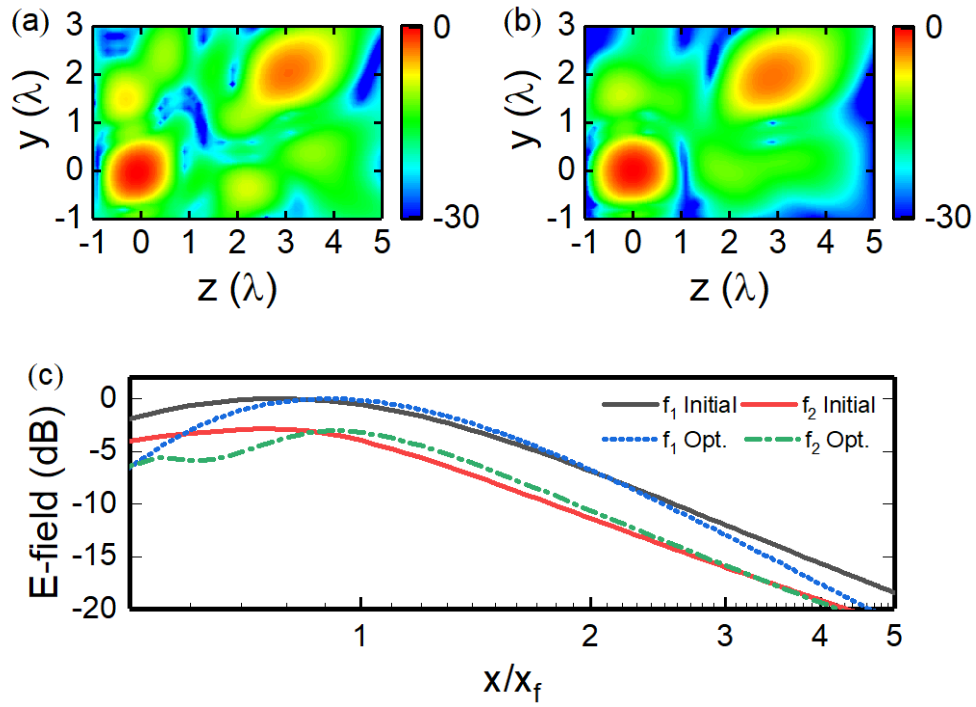
Figure 3.5 Focal shift correction of two focal points simultaneously: (a) normalized E-field for initial case on $x=-4\lambda$; (b) normalized E-field for optimized case on $x=-4\lambda$; (c) Normalized E-field distribution along transmitting direction of each focal points for both initial case and optimized case.

Table 3.2 Focal shift correction (unit: λ)

Preset (x_f, y_f, z_f)	f_1 (-4, 0, 0)	f_2 (-4, 2, 3)
Focusing locations (y_f, z_f) over focal plane $x = -4$		
Initial case	(-0.03, -0.06)	(1.90, 2.90)
Optimized case	(0.02, 0.02)	(2.04, 3.06)
Focusing locations (x_f) along x direction		
Initial case	-3.2	-3.4
Optimized case	-3.7	-3.8

3.3 Amplitude and phase specification

As the element tuning-based algorithm is a solution for optimizing the pattern around specified multiple focal points, it is supposed to adjust the amplitude and (or) the phase condition at these focal points with required values. In this part of the thesis, the scenarios of amplitude and phase specification are discussed.

With the proposed method, the amplitude and phase of each focal point f_m can be obtained and optimized with the procedure discussed above in this chapter. For the cases of amplitude and phase specification, the amplitude and phase on all or selected focal points must obey certain phase difference and power ratio. Let us assume that an NFMF array focuses at M focal points, and the target amplitude and phase condition for each focal point is A_m^f and φ_m^f. Rewriting them in a complex form, we can get $E_m^f = A_m^f \exp\left(\varphi_m^f\right)$ and they can be normalized as $\bar{E}_m^f$ for further calculations in the fitness function.

With the discussion above, the estimated complex field value at each focal point can be derived by (3.2) and expressed as $E\left(f_m\right)$. And the corresponding normalized value is $\bar{E}\left(f_m\right)$. With the normalized target values and estimated values on the focal points, the fitness function for amplitude and phase specification is

$$fitness = \prod_{m=1}^{M} \left| \bar{E}_m^f - \bar{E}(f_m) \right|. \qquad (3.4)$$

When the amplitude and phase of each focal point match the target values, the value of fitness function approaches zero. Then with the help of the GA optimization, the excitations of each antenna element can be derived.

In addition, as a special and commonly existing case of amplitude and phase specification in NFMF, a multi-focus condition with equal-amplitude and in-phase features needs to be mentioned. We specify that the complex E-field $E(f_m)$ at each focal point remains the same. With regard to the optimization, a fitness function with its optimization target is

$$fitness = \mathrm{Var}(E_f), \qquad (3.5)$$

where $E_f = \{E(f_1), E(f_2), \dots, E(f_M)\}$. When the variance among all the focal points approaches zero, the complex field value of each focal point can be seen as uniformly distributed, i.e. equal-amplitude and in-phase distribution. With the above optimization process, an NFMF with equal-amplitude and in-phase features can be achieved by the proposed method.

In order to demonstrate the performance of amplitude and phase specification function, an example of NFMF is given. As is shown in Figure 3.6, an NFMF design involving four focal points with the equal-amplitude and in-phase condition is realized by a near-field planar array with a scale of ten antennas along the y- and z-axis, respectively. The focal points are distributed on focal plane $x = -4\lambda$, and the coordinates of each focal point are listed in Table 3.3.

At first, the initial pattern is obtained by the NFMF method in Chapter 2 with the conjugate-phase approach with a simple superposition, which is shown in Figure 3.6(a). It can be noticed that the amplitudes of four focal points have a difference of 5.29 dB and the maximum phase difference between them is 12.7 degrees.

With the initial excitation derived above, the GA optimization is adopted for in-phase and equal-amplitude NFMF with a fitness function given by (3.5). The optimized patterns of amplitude and phase are shown in Figure 3.6(b). It is obvious that the amplitude of focal points is largely improved with a maximum difference of 0.49 dB, and the maximum phase difference among focal points is

reduced to 5.95 degrees. This comparison between these two cases indicates that the element tuning-based algorithm is fit for the NFMF with specified amplitude and phase conditions.

(a)

(b)
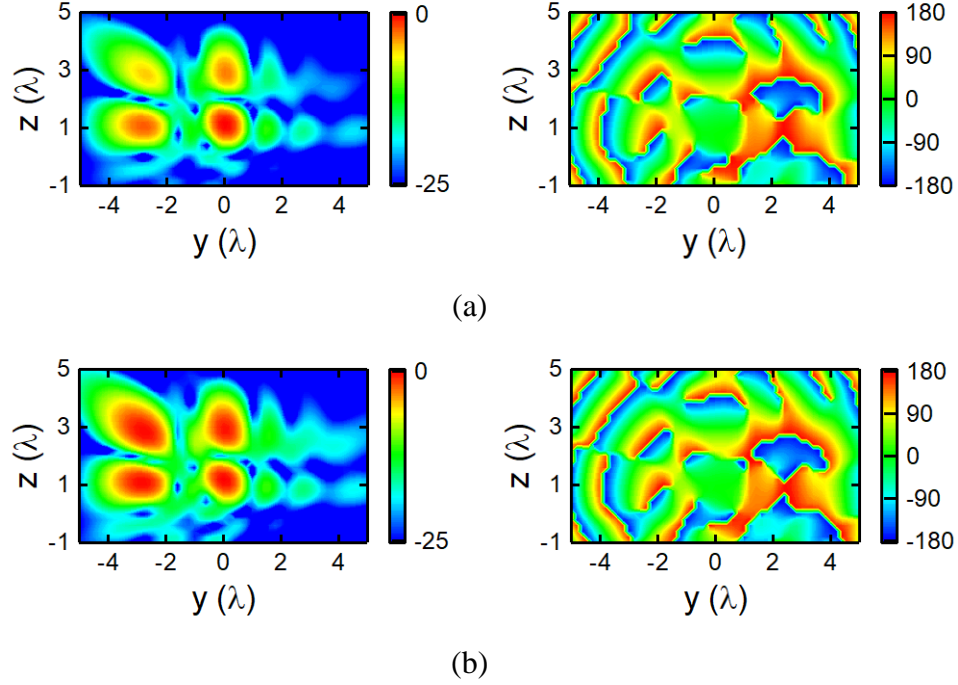
Figure 3.6 Pattern of amplitude (left) and phase (right) of NFMF array with in-phase and equal-amplitude conditions: (a) initial case; (b) optimized case.

Table 3.3 NFMF array with in-phase and equal-amplitude condition on $x = -4\lambda$

(y_f, z_f) (unit: λ)	f_1 (0, 1)	f_2 (0, 3)	f_3 (-3,1)	f_4 (-3,3)
Normalized amplitude (unit: dB)				
Initial case	-0.18	-3.18	-2.58	-5.47
Optimized case	-0.54	-0.28	-0.34	-0.77
Phase (unit: degree)				
Initial case	-5.59	-4.34	6.01	7.07
Optimized case	-1.39	1.98	-1.59	-3.97

3.4 Components design

The above discussion suggests that the antenna array for NFMF can be realized in theory with a linear or planar antenna array with identical elements, together with the excitations calculated or optimized by the NFMF methods proposed in this work. In this section, the physical realization of an NFMF array is discussed including the design of antenna array and the corresponding feeding network which offers unequal power as excitations.

A patch antenna is chosen as the building element of near-field array in the component design as it has a stable performance that has been widely demonstrated in the conventional array design. Patch antenna can be excited easily with a back-fed configuration with a vertical placed coaxial line, where the central pin of coaxial line serves as the feed and the metallic shield is connected to the ground of patch antenna. Meanwhile, microstrip line can serve as the feedline for the patch antenna, where electromagnetic field is coupled through the slot placed on the ground of patch antenna (Figure 3.7). In this way, only antennas are located at the front side of the antenna array without the interference caused by the feeding lines. Patch antenna also has its advantage in the pattern. Similar to the far-field pattern, the near-field pattern of the patch antenna has a wide beamwidth, which is suitable for a focusing task in the near-field region.

(a)   (b)
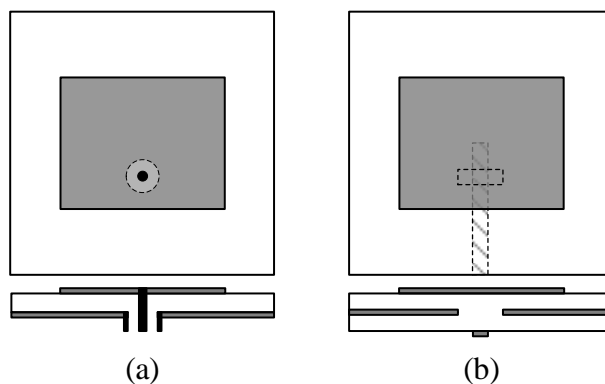
Figure 3.7 Configuration of back-fed patch antenna: (a) patch antenna fed by vertical located coaxial line; (b) patch antenna fed by microstrip line through coupling slot on the ground layer.

Feeding network is another important part to be considered in the designing process of the NFMF array. The antennas in a conventional phased array for far-field applications are commonly fed by excitations with uniform amplitude and equal phase difference. However, the excitations for the

NFMF array are not uniformly distributed for either amplitude or phase. Therefore, the feeding networks offering unequal outputs in both amplitude and phase are required. Conventional feeding networks such as Wilkinson power splitter may not afford this work because it cannot offer unequal distributed amplitude and phase simultaneously with a compact size even though this could be an overstatement. Under this circumstance, a microstrip line-based feeding network is developed with a function of unequal splitting amplitude and phase simultaneously.

The proposed feeding network provides output power with different sets of amplitude and phase at multiple output ports as excitations, which means that multiple phase shifters and impedance transformers need to be applied in the circuit development. Therefore, a microstrip line-based Pi network is introduced for tuning impedance and phase conditions (Figure 3.8). Two open or shorted microstrip stubs serve as the parallel stubs in the Pi network, and one microstrip stub serves as the series stub. All of the stubs have variable length and characteristic impedance according to the requirement of a power allocation between input and output ports. This property of this two-port network can be expressed as

$$Z_S = \frac{Z_1 Z_2 Z_L + Z_1 Z_3 (Z_2 + Z_L)}{(Z_1 + Z_3)(Z_2 + Z_L) + Z_2 Z_L} \tag{3.6}$$

Therefore, by tuning the components of Pi network, certain relationship between the input and output ports can be realized.
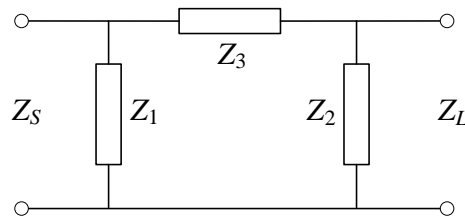
Figure 3.8 Configuration of Pi network as phase and amplitude tuning method.

As the feeding network is proposed to feed multiple antennas simultaneously, the Pi networks are connected in cascade, which is displayed in Figure 3.9. Each block stands for a Pi network, and the output ports are loaded in between these Pi networks to ensure each output has its own Pi network for impedance and phase tuning. In each Pi network, the tuning of Z_1, Z_2 and Z_3 is the main approach

to get proper outputs for all ports. However, this topology can only serve as the feeding network for a linear array. More works should be done to extend it for a planar array.
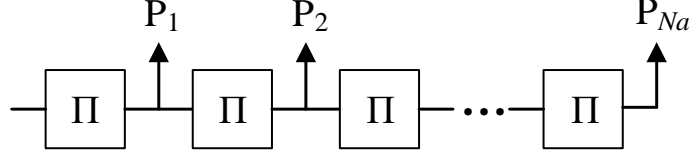
Figure 3.9 Cascaded Pi networks for multiple outputs with unequal distributed amplitude and phase.
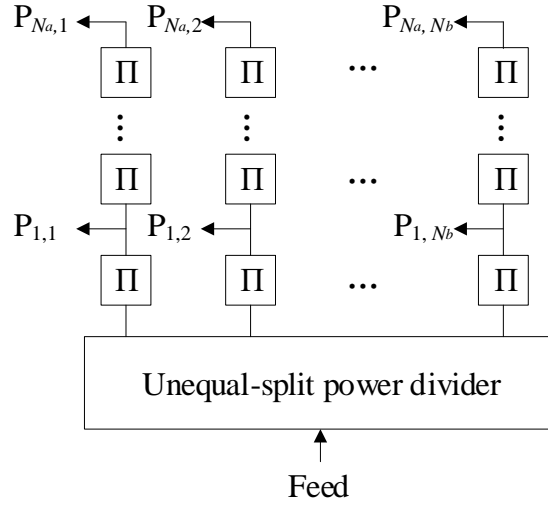
Figure 3.10 Configuration of planar feeding networks for planar array with $N_a \times N_b$ elements.

The feeding networks in Figure 3.9 can be extended for 2D applications when multiple serial structures are adopted simultaneously with proper topology. For a linear array with N_a rows and N_b columns, a linear feeding network (Figure 3.9) with N_a output ports is adopted. By preparing N_b linear feeding networks and placed them in parallel, a planar feeding network based on Pi networks is constructed, as shown in Figure 3.10. Moreover, these linear feeding networks need to be connected by an N_b-way power splitter to ensure an accurate power allocation at all the output ports. It can be observed that the output power at each output port is not uniformly distributed. Then, the power consumption of each column or each linear feeding network is not necessarily equal, and it is decided by

$$P_{n_b} = \sum_{n_a=1}^{N_a} P_{n_a,n_b} \quad n_b \in [1, N_b] \tag{3.7}$$

Therefore, the N_b-way power splitter with a function of unequal power allocation is developed and shown in Figure 3.11. The power splitter has several levels which are decided by the number of columns of the planar array. For each level, the proposed splitter has two output routes, and the power allocation is decided by the linear cascaded network (Figure 3.9) it would supply. The unequal power splitting is realized by tuning the characteristic impedance of microstrip line, denoted as Z_{11}, Z_{23} etc. By doing so, proper power is supplied to each linear feeding network for further allocation.
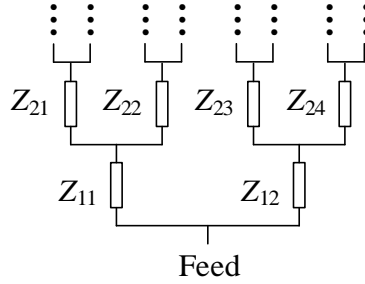
Figure 3.11 Configuration of unequal-split power divider.

3.5 Fabrication and experiments

In order to experimentally demonstrate the validity of the proposed algorithm and the corresponding design method, an experimental prototype is fabricated and tested in this work. A 2×8 (in the z and y directions) antenna array on yoz plane facing the negative x-direction is adopted to realize an equal-amplitude and in-phase focusing with 3 focal points on the plane $z = -8\lambda$. Detailed parameters of the focal points are listed in Table 3.4 (preset), and the results of focusing in different conditions are also listed and compared. It is worthwhile mentioning that the normalization reference of amplitude and phase is that of focal point no. 2.

Initial case: First, we calculate the initial excitations with the superimposed conjugate phase approach described by (2.7). With this approach, the E-field distribution is shown in Figure 3.15(a); location, amplitude and phase of the target locations are displayed in Table 3.4. We can find that

the initial values of excitations can only ensure the location of the targets, but not their amplitudes and phases.

Optimized case: Based on the above results, we apply the optimization approach to optimize the amplitude and phase of the focal points, the results in Figure 3.15(b) and Table 3.4 show that the maximum error of consistency of amplitude is 1% and that of phase is 0.23°. Therefore, we can conclude that with the help of the proposed optimized approach, the NFMF with equal-amplitude and in-phase features can be obtained.

Table 3.4 Equal-amplitude and in-phase NFMF $z = -8$ (unit: λ)

Case　　　　No.	1	2	3
Preset (x_f, y_f)	(-8, 0) A_0/φ_0	(-8, 3) A_0/φ_0 (Ref)	(-8, 7) A_0/φ_0
Initial case	(-8, 0) 1.04/51.61°	(-8, 3) 1/0°	(-8, 7) 1.12/36.03°
Optimized case	(-8, 0) 1.00/-0.01°	(-8, 3) 1/0°	(-8, 7) 1.01/-0.23°
Full-wave Simulation	(-8, 0) 0.99/-1.30°	(-8, 2.8) 1/0°	(-8, 6.8) 0.86/-0.40°
Test (optimized case)	(-8, -0.2) 1.04/-2.59°	(-8, 3) 1/0°	(-8, 7) 0.96/-0.05°

Full-wave simulation: This is carried out by the use of CST Microwave Studio. For each antenna element, the excitation is assigned according to the results derived by the optimized case above. The results are displayed in Figure 3.15(c). The location, phase, and amplitude of the focal points are listed in Table 3.4, which are coincident with the calculation results of the optimized case.

Experimental test: To further verify the optimized proposed method, practical experiments are developed and conducted in the work. In this case, a three-layer technique used in the development of our experimental prototype is displayed in Figure 3.12. The first layer is the antenna layer

composed of printed planar patch antennas operating at 10 GHz made on RT/duroid® 6002 with a dimension of 0.324/0.420 inches. The second layer is the metallic ground that serves as the ground plane for each antenna on the antenna layer. The third layer is the feeding network, where an eight-way unequal-split power divider is used to allocate power to each column (Figure 3.12). For each column, two output ports are serially connected by Pi networks, which is used for adjusting the output phase and amplitude of each port. The proposed feeding network can split the power of feeding to 16 ports with not only different phases but also different amplitudes specified by requirements. Each output port is aligned with corresponding patch antenna with a pin through the ground plane, which forms the pin-fed array. The Pi network adopted in the proposed prototype is a microstrip based unequal feeding network printed on RT/duroid® 6002 with 1 input and 16 output ports.
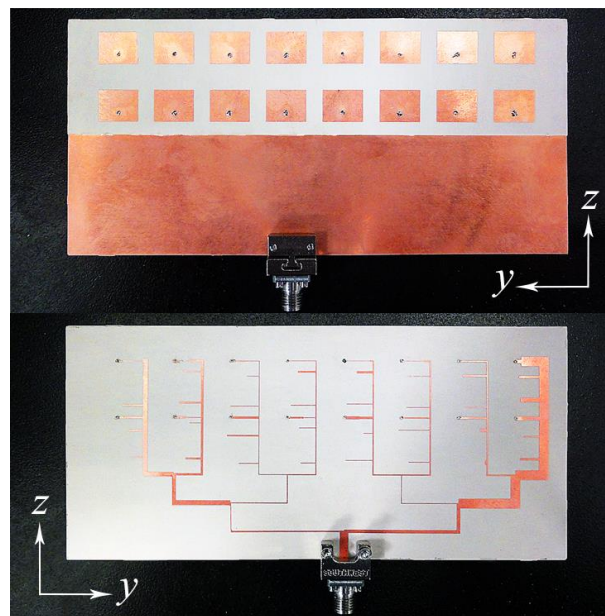
Figure 3.12 Prototype of antenna array for NFMF: antenna layer, ground layer, and layer for feeding network.

Our testing environment is pictured in Figure 3.13. The whole system consists of several parts, including a testing platform with a plane scanning function, a linearly polarized waveguide probe for field collection at X-band with dimension of 0.899/0.402 inches, a 2-port Anritsu VNA 37369D, and one PC.
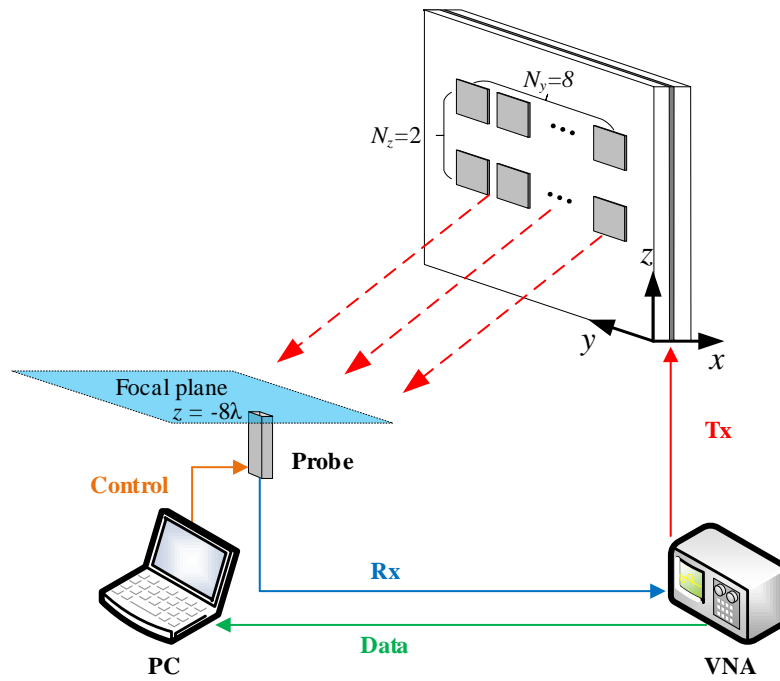
Figure 3.13 Configuration of testing environment and signal flow.
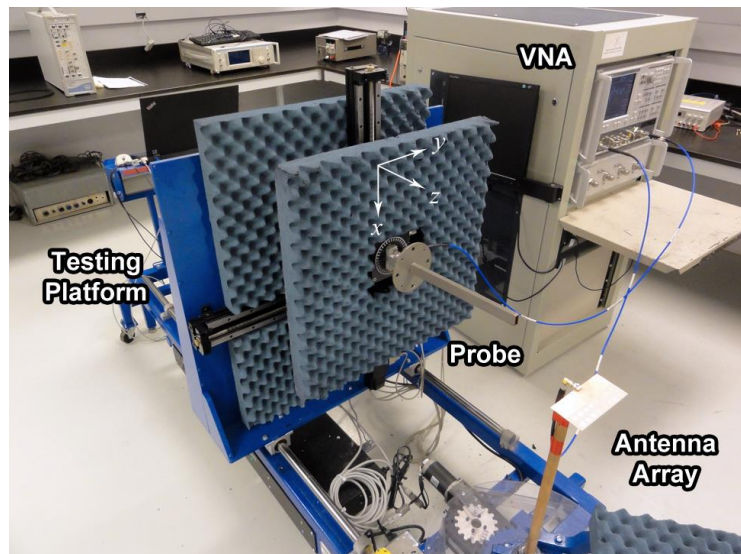
Figure 3.14 Facilities and testing environment.
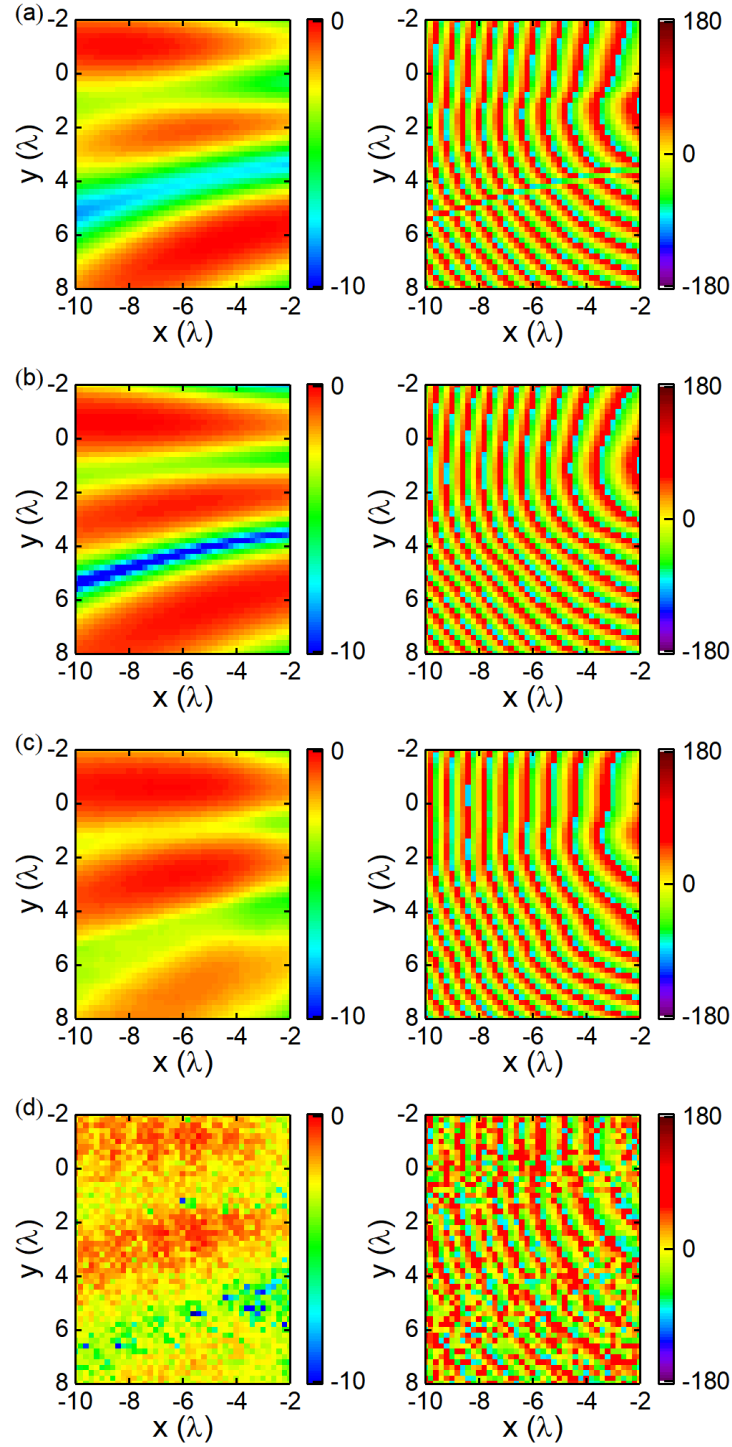
Figure 3.15 Amplitude and phase distribution on focal plane z = -8λ: (a) calculation without optimization; (b) calculation with GA optimization; (c) full-wave simulation based on optimized case; (d) experimental results based on optimized case.

The connection between device parts is also displayed. Port 1 of VNA drives the antenna array as the feed, and a waveguide probe aligned to Port 2 of VNA serves as the receiving port, so that S_{21} can be measured by VNA. The probe is controlled by a PC-driven platform to scan the focal plane ($z = -8\lambda$) with a step of 0.2 wavelength at 10 GHz to yield the near-field map of a specified area. S_{21} data measured by VNA on the scanned plane is sent to PC for further processing. The photo of testing environment is shown in Figure 3.14.

With the above-configured experimental set-up, the testing results are shown in Figure 3.15(d). E-field distributions on the focal plane are well coincident with the calculated results of the optimized NFMF generally except some points. The inaccuracy may possibly be caused by manufacturing tolerance or assembling deviation of the antenna array, and noise floor while testing. Mutual coupling between antenna elements may also introduce some error although we set a relatively large spacing between array elements. This effect should be taken into consideration in our future work. According to Table 3.4, the testing results of the focal points have an error of 8.3% on amplitude and 2.59º on phase, which is slightly larger than that of the calculated results. Overall, the testing has successfully demonstrated that the proposed NFMF method and the corresponding approach of optimization can be very useful for practical implementations.

3.6 Conclusion

In this chapter, a method for designing a near-field multi-focusing antenna array with an element tuning-based algorithm is proposed and studied theoretically and experimentally. The principle of the method is concerned with the conjugate-phase approach, superposition theorem and iterative optimization method, by which multi-focusing features with specified field requirements in the near-field region can be obtained.

The rapid semi-analytical NFMF method can define multi-focusing not only on specified locations but also certain amplitude and phase conditions on or around the focal points. Examples of multi-focusing with different forms illustrate that the proposed method is adequate for various situations. The conventional focal shift issue introduced by a near-field focusing can be well corrected or reduced by the proposed method. Equal-amplitude and in-phase multi-focusing is also well described and exemplified in the work. Experimental test was conducted to demonstrate the validity

of the proposed method. This method is promising for a wide range of applications such as spatially localized signal synchronization or distribution, and near-field wireless power delivery.

CHAPTER 4   PATTERN TUNING-BASED NFMF ARRAY

Element tuning-based algorithm and its corresponding design method offer a solution for designing an antenna array for NFMF. With the help of iterative optimization method, the proposed algorithm is able to shape the near-field pattern on discrete points. As a result, NFMF with specified amplitude and phase can be achieved.

However, the proposed algorithm has its own constrains. First, the computational speed is limited by the convergence rate of iterative optimization, which degrades the rapidity of the proposed algorithm mostly. Second, the proposed algorithm supports a limited number of the focal points, as the SLL will influence the performance of resolution as the number of focal points increases to a large scale. Moreover, the algorithm only supports the development of discrete focal points.

Under this circumstance, another type of algorithm is developed in this thesis to mitigate the above-stated problems, which is presented in this chapter. Different from the element tuning-based algorithm, the algorithm proposed in this part of the thesis aims at tuning patterns that are ready to be superimposed. Pattern tuning-based algorithm is an analytical solution with a rapid computational speed. Moreover, it works on not only discrete focal points with a large scale, but also continuous focal areas with specified shapes.

Furthermore, more functions of NFMF array are realized due to the proposed highly efficient algorithm, which is discussed in the following. For example, power combining, power splitting, and phase shifting for signal processing can be all realized spatially with the pattern tuning-based algorithm. In this chapter, the design and test methods are discussed in detail.

4.1   Pattern tuning-based algorithm for NFMF

In a similar vein as the algorithm developed in the last chapter, the proposed pattern tuning-based algorithm also takes advantage of the conjugate-phase approach for multi-focusing in the near-field region. Therefore, the configuration of the near-field array is also linear or planar array with identical elements.

It is assumed that the antenna array has N elements, simultaneously concentrated at specified M targets on a near-field pattern. As is discussed in the previous chapters, in order to accomplish multi-target focusing, we propose an analytical solution in connection with the conjugate-phase

approach and the superposition principle of waves. Here we introduce one tuning factor for each focal point for signal processing purpose. Therefore, the excitation of each antenna can be estimated by the following equation

$$I_n{}'' = \sum_{m=1}^{M} T_m \exp\left(j\varphi_{nm}\right) \quad n \in [1, N].$$ (4.1)

where $\varphi_{nm} = kl_{nm}$, represents the conjugate-phase of n_{th} antenna for m_{th} pattern. According to Chapter 2, when superimposing the injection-phase condition of target 1 to M as the injection voltage, a linearly superimposed near-field pattern is formed directing at target 1 to M simultaneously. However, this straightforwardly superimposed pattern cannot be tuned for specific requirements such as power intensity of target point or phase delay.

As such, vector $\mathbf{T}$ with a dimension of M (the same as the number of targets) is introduced as tuning vector, and T_m represents the tuning factor for pattern m, which is illustrated in Figure 4.1. By tuning each value T_m of vector $\mathbf{T}$, intensity and phase delay of each single pattern focused at its corresponding target can be adjusted independently. When these M patterns are superimposed, they can maintain the linearity of superposition. Therefore, with these tuned excitations, the near-field pattern of antenna elements can concentrate on designated targets with specified amplitude and phase delay.

Near-field pattern is decided by not only the amplitude and phase condition of each antenna, but also by the propagation feature of antennas themselves. By introducing the infinitesimal dipole equivalent model [33, 39] as the field model in the near-field region, we can derive the near-field pattern of each antenna element. Combined with the excitation of elements we mentioned above, the superimposed pattern in the near-field region can be expressed as

$$\mathbf{F} = \sum_{m=1}^{M} \left[T_m \sum_{n=1}^{N} \mathbf{E}_{nm} \exp\left(j\varphi_{nm}\right) \right],$$ (4.2)

where $\mathbf{E}_{nm}$ is the vector field value of the n_{th} antenna element transmitted to the m_{th} focal point estimated by either method above with a unit excitation. When these antenna elements are excited by specified excitations as in (4.1), the superimposed vector field value at M focal points is presented as $\mathbf{F}$ in (4.2).
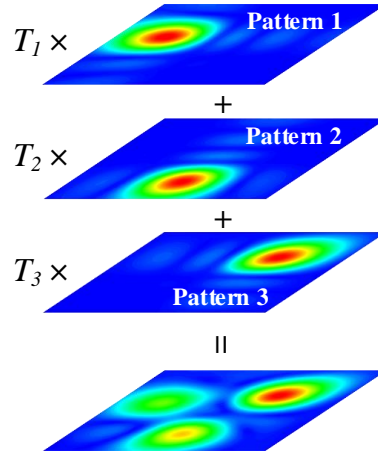
Figure 4.1 Illustration of pattern-tuning based algorithm including three focal points with different amplitude.

This equation describes the universal derivation of a superimposed pattern in the Fresnel region. Therefore, the field values of special points like focused targets can be definitely generated by this equation with certain tuning vector $\mathbf{T}$ where $\mathbf{T} = [T_1, T_2 \ldots T_M]^{\mathrm{T}}$. Conversely, when targeting points with a designated intensity and phase delay, the corresponding $\mathbf{T}$ is determined by this equation as the number of targets is equal to the dimension of $\mathbf{T}$. The solution of $\mathbf{T}$ can be expressed in matrix form as

$$\mathbf{T} = \left(\mathbf{C}^{\mathrm{T}}\mathbf{E}\right)^{-1}\mathbf{F} . \tag{4.3}$$

In the above equation, $N{\times}M$ matrix $\mathbf{C}$ consists of conjugate-phase coefficients where $C_{nm} = \exp(j\varphi_{nm})$. Matrix $\mathbf{E}$ shares the same scale of the $\mathbf{C}$ matrix, representing the vector field values on M targets contributed by N antenna elements with unit excitation; M column vector $\mathbf{T}$ is the tuning vector for M targets; and $\mathbf{F}$ is the designated field value at these targets.

As the intensity and phase delay of targets are defined by $\mathbf{F}$ at single/multiple discrete locations or continuous regions, the corresponding tuning vector $\mathbf{T}$ is derived through (4.3). Subsequently, the excitation condition of antenna elements can be obtained by calculating product $\mathbf{CT}$.

In the above-proposed theory and its related algorithm, the excitations of the antenna array for a specific superimposed pattern with multiple designated points can be calculated. It is worth mentioning that the algorithm offers an efficient analytical solution for a multi-targeting problem

in a near-field region without resorting to a large scale full-wave simulation or optimization process. The succinct form of an algorithm leads to a rapid calculation and capability of processing a large number of patterns focusing on corresponding focal spots. In all, the proposed algorithm offers an analytical solution for near-field pattern shaping at multiple discrete targets or continuous regions.
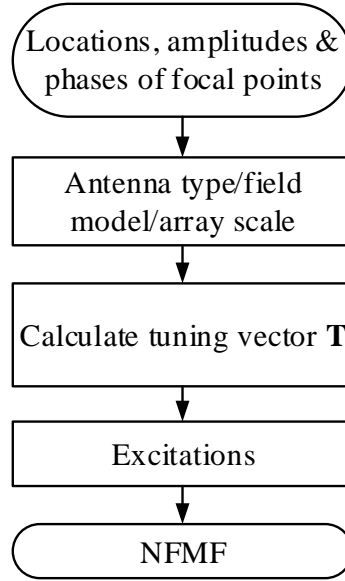
Figure 4.2 Block diagram for pattern tuning-based NFMF array.

The procedure of the proposed algorithm is shown in Figure 4.2. The first step is specifying the spatial location, amplitude and phase condition of the target focal points in order to get vector $\mathbf{F}$. The second step is similar as that governed by the algorithm proposed in the previous chapters, including selection of the antenna type as array element; calculation of the field model of the selected antenna with infinitesimal dipole model; and estimation of array scale by resolution R discussed in Chapter 2. With the field model derived in step 2, matrix $\mathbf{E}$ for field distribution and matrix $\mathbf{C}$ for conjugate-phase can be yielded. With $\mathbf{F}$, $\mathbf{C}$ and $\mathbf{E}$, the pattern tuning-based factor can be calculated by (4.3). Afterwards, the excitations of the antenna array can be calculated by $\mathbf{CT}$. Then at last, the NFMF pattern of the antenna array can be estimated.

4.2 Spatial signal processing

As the classical approach, interactions among localized or discrete signal processing devices are usually accomplished by electromagnetic waves guided in conductor and/or dielectric bounded structures featuring specific circuit functions. Such electromagnetic circuits are now set to face the issues of geometry complexity and/or power capacity when they are used in large scale electromagnetic systems such as a massive MIMO. In this part of the thesis, we propose and present an unconventional approach to accomplish the function of interaction among devices. Interaction or transmission relies on field interferences induced by NFMF array and carried by the free space in the Fresnel region where signal processing can be accomplished spatially. Typical applications are demonstrated by examples below. It is worth mentioning that the proposed approach is universally applicable to all physical wave devices and systems, such as acoustic waves and the demonstrated electromagnetic waves.

In the pattern tuning-based algorithm, we devise and demonstrate a fundamental theory to define the amplitude and phase condition of array. In this way, the designated array is able to produce controllable near-field patterns and wirelessly deliver signal or energy to multiple targets or regions with a predefined amplitude and phase conditions, which allows performing near-field or remote signal processing functions instead of wired local circuit operations.

As mentioned above, the devised scheme enables arbitrary and flexible spatial power delivery and wireless signal processing through near-field focusing. To be more specific, signal transmission and processing are all accomplished spatially for electromagnetic devices free from physical transmission line contacts, guided-wave or wired connections. A basic graphic and operational illustration and procedure of the proposed near-field focusing approach are shown in Figure 4.3, which mainly include the signal transmitting part (one or more antenna arrays), wireless channels (a free space among devices) and the receiving part (one or more electromagnetic RF frontends for receiving signals with the purpose of further processing).

In this near-field wireless approach, the input signals of pre-stage devices, which are ready for transmission or processing, are collected by NFMF arrays with transmission lines or wirelessly, as shown in Figure 4.3, at flexible but pre-designated spatial locations either wirelessly or wired. Subsequently, the inputs are processed by the NFMF arrays then transferred to multiple target

locations in free space with designated technical features. In this spatially transferring route, electromagnetic interference properties are carefully calculated and applied in order to combine, split or modify the input power. Target points or regions are defined according to the location and form of receiving devices. Spatial plane(s) where the target points or regions are physically located is (are) defined as receiving plane(s). The antennas of the receiving devices are located in such designated areas to receive signals transmitted by the antenna arrays. With this approach, an interaction between those localized devices is accomplished. In this way, the locations of these devices can be flexibly defined without the constraint of a conventional circuit system and complex passive network electrically wired for transmission between multiple routes or layers, which are also simplified in the proposed scheme with an interference transmission in the open space.
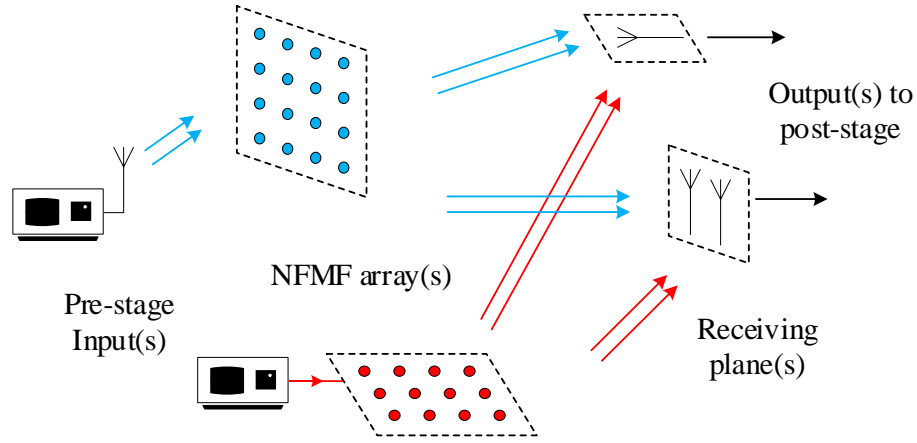
Figure 4.3 Configuration and procedure of the spatial signal processing.

To accomplish accurately both directional transmission and signal processing for spatially distributed multiple targets or regions, the near-field pattern of NFMF array regulated by phase compensation and superposition principle is adopted to define each phase difference of an array in section 4.1. As a novel approach of signal processing, the fundamental functions in conventional signal processing are discussed below spatially, which realized by NFMF arrays.

4.2.1 Spatial power splitting

The devised spatial transmission approach is to specify the vector field on multiple spots or areas within a Fresnel region; namely, it can accomplish power or signal transfer to a specified location(s)

with designated field parametric properties. In taking advantage of this scenario, this approach can realize a fundamental function of passive circuits in a spatial or wireless manner.

In a communication or sensing system, the splitting of signal or power is a common operation utilized in most signal processing and routing. A power divider or directional coupler serves as a usual circuit for an equal or arbitrary power splitting. Such solutions work well for conditions with regular and planar distributed loads. However, they may introduce a bulky or complex passive circuitry in the case of massive, irregularly, and spatially distributed loads, such as multi-inputs and multi-outputs.

Therefore, the proposed spatial-interference approach offers an unprecedented solution for massive-way spatial power splitting with diversified equal or unequal distributed intensity for which the locations of loads can be arbitrarily assigned, as in Figure 4.4, without considering the construction of a complex multilayer circuit.
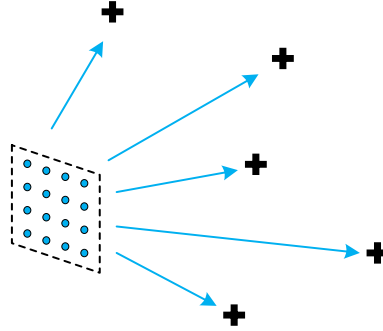
Figure 4.4 Schematic of spatial power splitting with one input and spatially distributed multiple outputs with equal or unequal power ratio.

At the target locations of power splitting, vector $\mathbf{F}$ is defined as follows,

$$\mathbf{F} = \left[A_1 \exp\left(j\varphi_1 \right), \cdots, A_M \exp\left(j\varphi_M \right) \right]^{\mathrm{T}}. \tag{4.4}$$

In the case of an equal splitting, $A_1 = A_2 = \cdots A_M$ and $\varphi_1 = \varphi_2 = \cdots \varphi_M$. Whereas, for an unequal splitting, each item of vector $\mathbf{F}$ is independently defined for each target.

In conventional design of circuits, it is a common type of power splitter that features equally distributed power on multiple output ports. Then in the spatial power splitting, this requirement or

configuration can be converted to equal splitting on selected focal points. Therefore, examples of spatial equal splitting in the near-field region are proposed.

The near-field antenna array adopted in this work is a 16×16 patch antenna array, where the spacing between neighboring antennas is 0.5λ. The spatial locations of outputs can be arbitrarily defined as required. Two cases of spatial power splitting are shown with equally distributed intensity for each output on a receiving plane ($x = -8\lambda$).
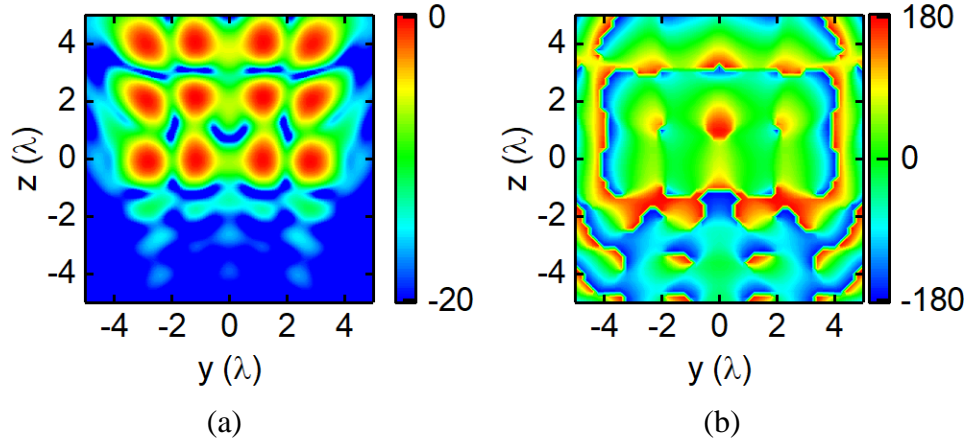
Figure 4.5 Example of spatial power splitting with matrix-form distributed targets: (a) normalized amplitude (dB); (b) phase (degree).

Table 4.1 Focal points and corresponding focal shift of matrix-form NFMF (unit: λ)

Focal point (y_f, z_f)	(-3, 0)	(-1, 0)	(1, 0)	(3, 0)
Focal shift	(0.2, -0.1)	(-0.2, 0)	(0.2, 0)	(-0.1, -0.1)
Focal point (y_f, z_f)	(-3, 2)	(-1, 2)	(1, 2)	(3, 2)
Focal shift	(0.2, 0)	(-0.1, 0.2)	(0.2, 0.1)	(-0.1, 0.1)
Focal point (y_f, z_f)	(-3, 4)	(-1, 4)	(1, 4)	(3, 4)
Focal shift	(0.1, 0)	(-0.1,0.1)	(0.2, 0.1)	(-0.1,0)

In the first example, the focal points are arranged with matrix-form, which have an equal spacing of 2λ in the y-direction and 1.5λ in the z-direction (Figure 4.5). The detailed locations and the

amplitudes of focal points are listed in Table 4.1, slight focal shift occurs according to the results. All the target points share the same normalized amplitude of -0.55 dB and phase of 0 degree.

Another example of NFMF featuring unequally spaced focusing is presented. In the case of circular form, 13 focal spots are distributed on two concentric circles with radiuses of 2λ and 4λ, with another focal spot located at the center. Detailed information of coordinates is listed in Table 4.2. The transmitting antenna array adopted for this case is the same as that for that in Figure 4.5. Then the near-field pattern of NFMF is estimated and shown in Figure 4.6.

Similar to the lattice form pattern, amplitude of each focal point has an identical normalized value of -0.17 dB, and the phase is 0 degree. And the average focal shift among focal points is lower than that of matrix-form as the average spacing among focal points is larger, which reduces the disturbance of superposition.
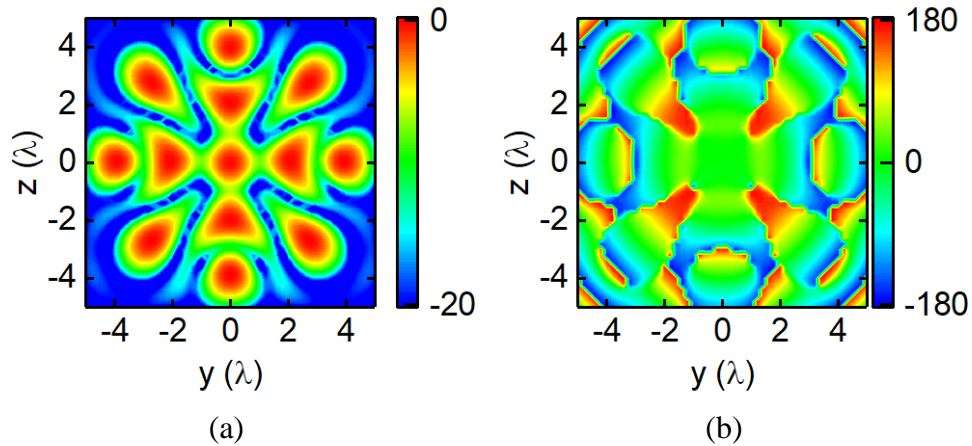
Figure 4.6 Example of spatial power splitting with circular distributed form distributed targets: (a) normalized amplitude (dB); (b) phase (degree).

Compared with conventional circuit-based power splitter, the proposed near-field spatial power splitter is more flexible. For equal or unequal power splitting, the physical configurations of antenna array share the same form as the power distribution is fully controlled by excitations calculated by the proposed algorithm. While for conventional power splitter, lumped element-defined loading conditions with different value or topology are required for different power distribution.

Another feature of the spatial power splitter is related to space utilization. The length in transmission direction is enlarged when utilizing conventional power splitters with massive outputs. As the frequency increases, transmission loss increases as well. Whereas, for a spatial power splitter, the number of outputs does not influence the device's length along the transmission direction, and it would focus on locations arbitrarily selected in the Fresnel region as outputs.

Table 4.2 Focal points and corresponding focal shift of circular form NFMF (unit: λ)

Focal point (y_f, z_f)	(-4, 0)	(-2.8, 2.8)	(0, 4)	(2.8, 2.8)
Focal shift	(0.1, 0)	(0.1, 0)	(0, 0)	(-0.1, 0)
Focal point (y_f, z_f)	(4, 0)	(2.8, -2.8)	(0, -4)	(-2.8, -2.8)
Focal shift	(-0.1, 0)	(0, 0.2)	(0, 0.1)	(0, 0.2)
Focal point (y_f, z_f)	(-2, 0)	(0, 2)	(2, 0)	(0, -2)
Focal shift	(-0.1, 0)	(0, 0.1)	(0.1, 0)	(0, 0)
Focal point (y_f, z_f)	(0, 0)			
Focal shift	(0, 0)			

As the spatial power splitter is able to allocate power flexibly in space, it can serve as a wireless local oscillator (LO) for driving quasi-optical mixers [40] which are able to receive LO and RF signals by their antennas. It can also act as a signal synchronization since no complex feeding networks are required for power splitting, and the wireless feeding points can be arbitrarily adjusted according to the locations of mixers. Definitely, this technique is promising for systems involving massive channels or large scales of devices like massive MIMO in much-discussed 5G networks.

4.2.2 Spatial power combining

In the last section, we have demonstrated the examples of spatial power splitting schemes at multiple discrete points. The proposed approach can also be applied to a power allocation in continuous regions with both regular and irregular shapes. In the designated regions or spots, field

intensity and phase delay could keep constant or vary continuously according to a predefined value in each region.
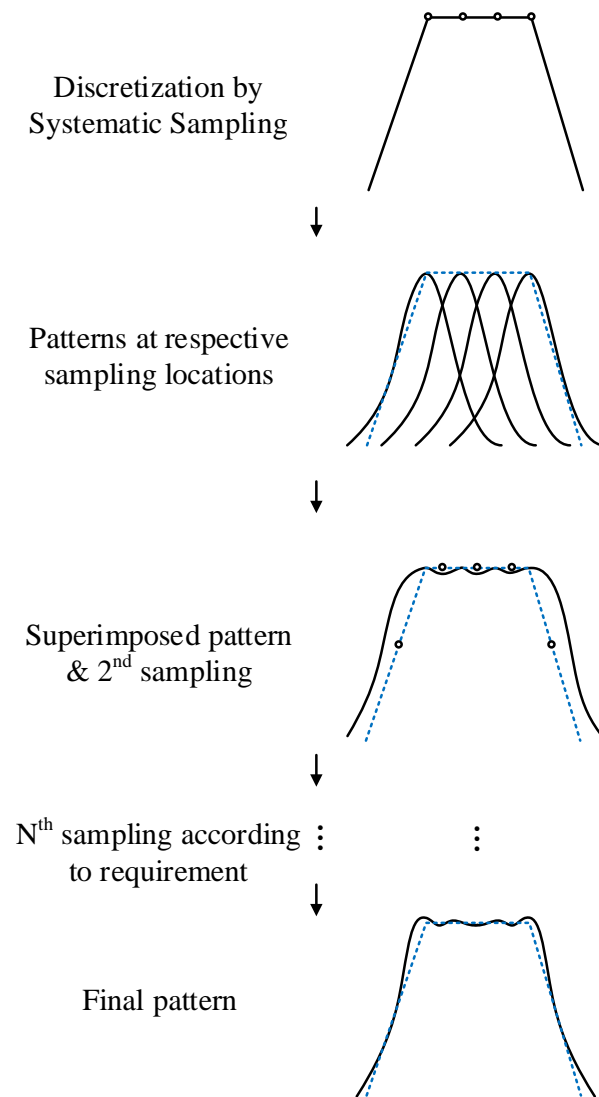
Figure 4.7 Procedure of pattern shaping on continuous focal region.

With reference to discretization, continuous focal region(s) is equivalent to a group of sampling spots in a desired area or space with a tolerable deviation from the exact design target. Based on this fundamental idea, the proposed algorithm for discrete points focusing can be converted and made available for the continuous region(s).

Its process can be explained in Figure 4.7. The first step is a discretization of the focal region(s). The selection of discretized spots abides by a uniformly sampling rule in the desired area or space.

Then, the problem of a continuous region is converted to that of discrete targets on the second step. The coordinates, intensity and phase delay of sampling spots are defined as complex values in vector **F**, and the excitations of source array are calculated by the proposed approach according to these specified conditions. As the third step, an initial solution is generated by a superimposed pattern, which is formed by the antenna elements with given excitations. Furthermore, this pattern can be further adjusted to fulfill the requirement of field or wave focusing, such as SLL and ripple effect, by assigning new sampling spots for a second time with further calculation by the proposed approach. Ultimately, the final pattern which satisfies the design requirements comes out with one or more iterative adjustments.
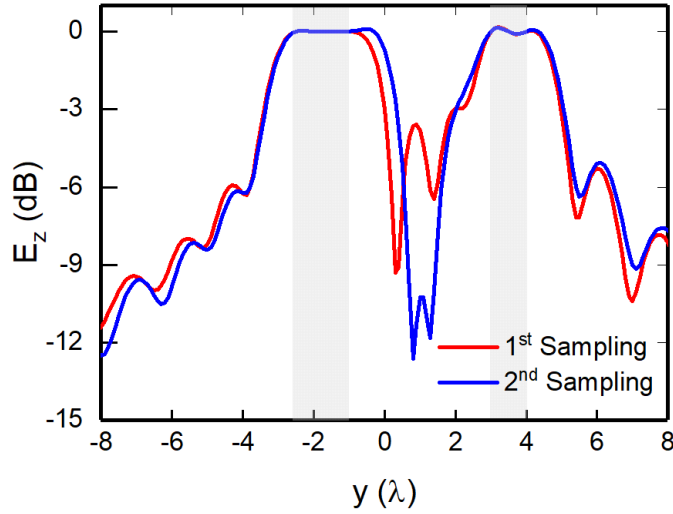
Figure 4.8 Example of 1-D converging case with dual sub-regions.

A one-dimensional case study is shown in Figure 4.8. In this example, a linear antenna array with 16 elements along the y-axis is adopted as antenna elements. The focused region is defined as $y \in (-2.5\lambda, -\lambda) \cup (3\lambda, 4\lambda)$ on the straight-line $x = -8\lambda$, $z = 0$ with uniform intensity. The initial solution is derived by a uniform sampling at two focused regions with a spacing of 0.5λ. However, the power level between the two focused regions is high and needs adjustment. In the second sampling on spots $y = 0.7\lambda$ and $y = 1.4\lambda$, with a designated suppression of -10 dB, the optimized pattern has higher contrast and power efficiency.

Furthermore, the case of convergence over the two-dimensional continuous region(s) shares a similar solution as the above example, but the sampling should be applied along each axis. Therefore, we can realize power combining in the spatially continuous region(s) by extending the proposed approach.

As a common example of the two-dimensional case, we assume a converging case with a single continuous region where the vector field maintains constant. Therefore, vector $\mathbf{F}$ is defined as

$$\mathbf{F} = \left[A_0 \exp\left(j\varphi_0 \right), \cdots, A_0 \exp\left(j\varphi_0 \right) \right]^{\mathrm{T}}. \tag{4.5}$$

The amplitude and phase delay of sampling spots are identical to accomplish a continuously uniform distributed pattern in the target region(s).
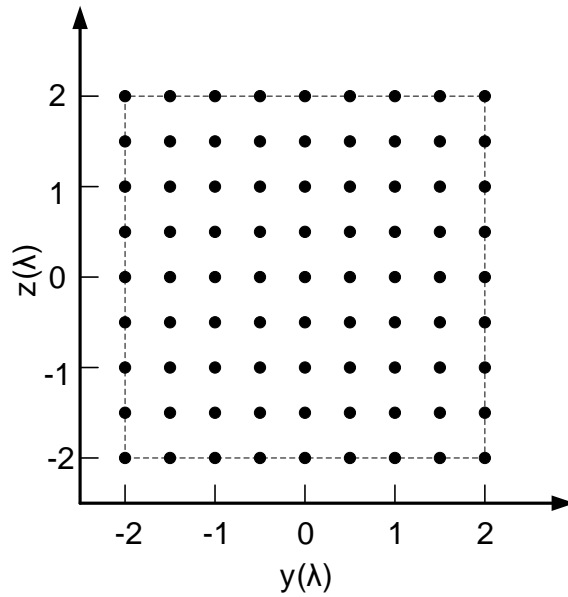
Figure 4.9 Distribution of sampling spots for NFMF in a square region (dashed line).

The target regions of two examples shown below have different shapes, while the intensity and phase delay maintain uniformity in each area on the receiving plane 4λ away from the antenna elements realized by the 16×16 matrix formed antenna array located at the center of the yoz plane with a spacing of 0.5λ between elements.

The first example shows a case of electric power converging on a square area with a side length of 4λ having uniform amplitude and phase. The sampling of the square region is shown in Figure 4.9,

where the spacing between sampling spots along *y*- and *z*-direction are both 0.5λ. On each sampling spot, the target amplitude and phase are the same to maintain the flatness of amplitude and phase distribution in the target area (inside dashed line in Figure 4.9).

(a)   (b)
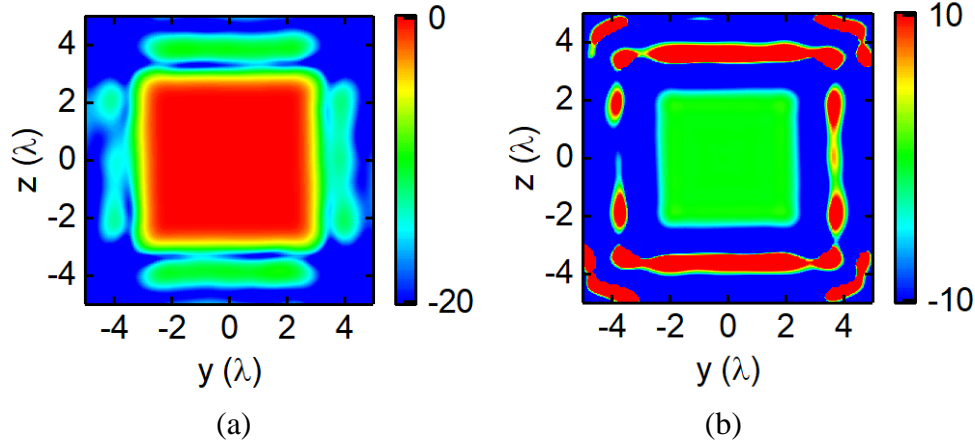
Figure 4.10 Spatial power combining on square region with uniform distribution: (a) amplitude (dB); (b) phase (degree).
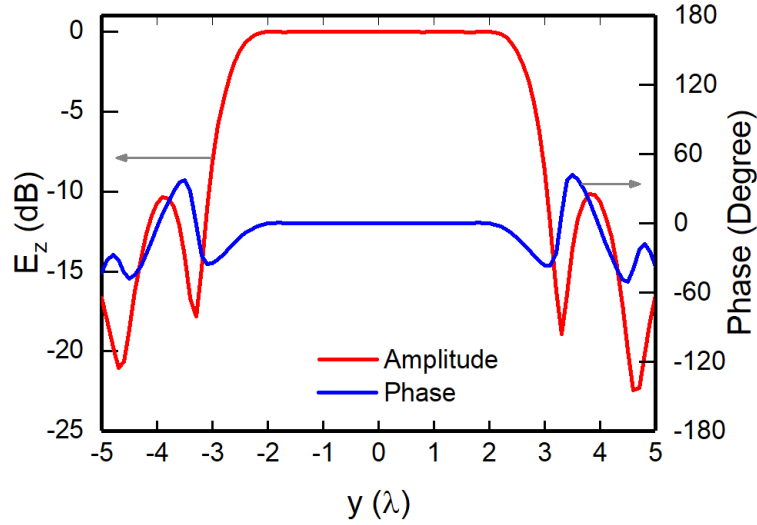
Figure 4.11 Field distribution of spatial power combining on square region along $z = 0$ on focal plane.

By adopting the pattern tuning-based algorithm, the near-field pattern is estimated and shown in Figure 4.10, where the amplitude and phase are uniformly distributed in the target focal region. The maximum difference of amplitude is 0.2 dB and the -3dB point of the focal region is 0.8λ away

from the focal region along each axis according to Figure 4.11. The maximum phase difference is 7.70 degrees in the focal region. The results indicate that NFMF can be accomplished in regular areas with systematic sampled focal points.

And the second example shows a circular region located on yz plane with a radius of λ (dashed line in Figure 4.12) with the same antenna elements but different excitations yielded by the proposed approach. Different from the case mentioned above, in this example, the boundary is not regular as a straight line neither along y- nor z-direction.
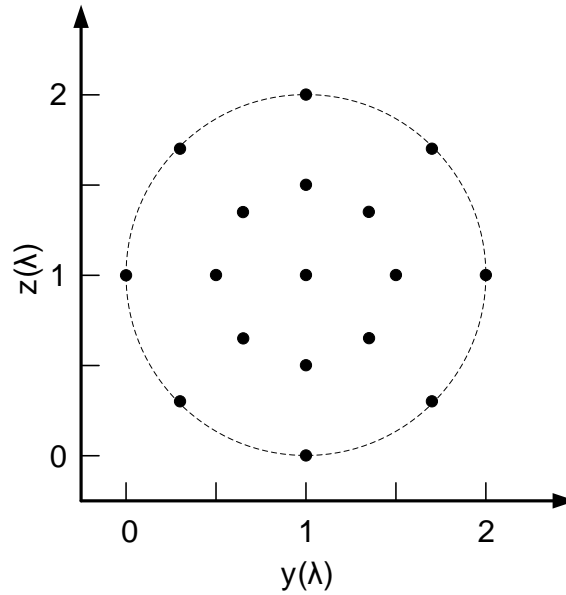
Figure 4.12 Distribution of sampling spots for NFMF in a circular region (dashed line).

To get a curved boundary coincident with the preset target in the near-field pattern, a reasonable sampling approach needs to be adopted. The sampling spots assigned for this example are concentric from the center of the circular region, which is illustrated in Figure 4.12. The sampling spots are uniformly distributed along the edge of corresponding concentric circles in the circular area. For example, the outer circle for sampling has a radius of λ, and the inner one has that of 0.5λ. The example is suitable for focal areas with curved boundaries as it maintains a relatively uniform sampling along radial and axial directions.
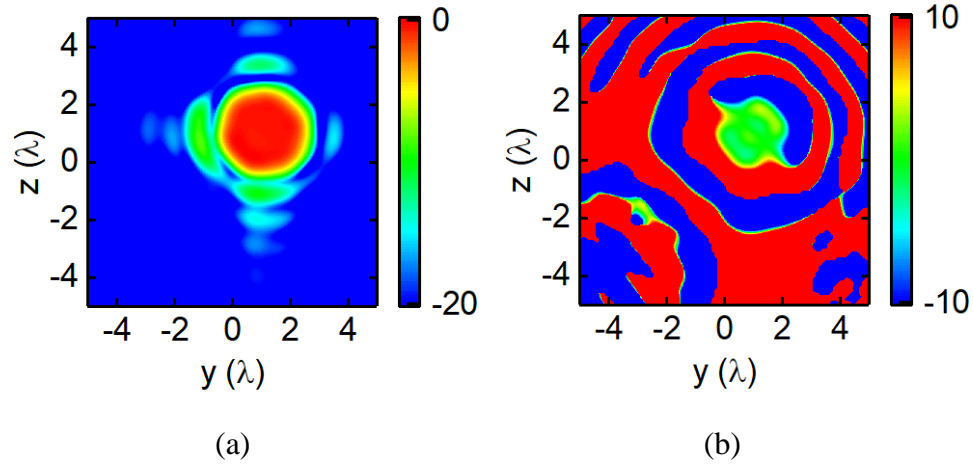
Figure 4.13 Spatial power combining on circular region with uniform distribution: (a) amplitude (dB); (b) phase (degree).
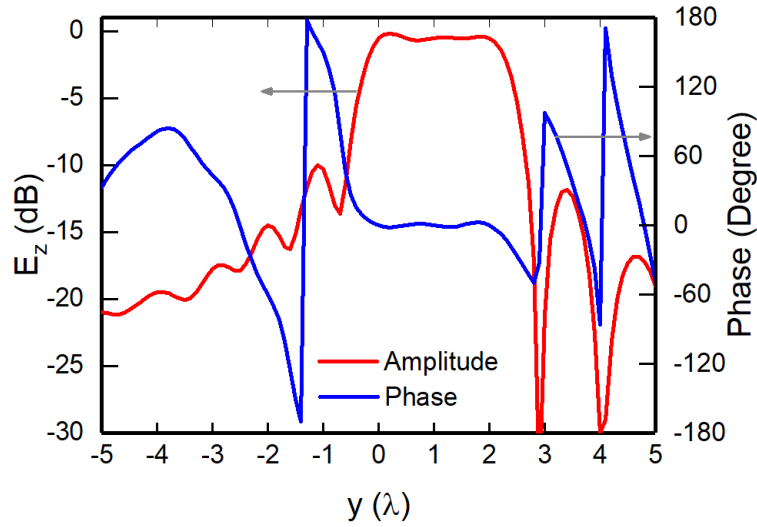
Figure 4.14 Field distribution of spatial power combining on circular region along $z = \lambda$ on focal plane.

By assigning the sampling spot with identical amplitude and phase condition, the proposed algorithm is applied for deriving the near-field pattern, which is shown in Figure 4.13. The maximum difference of amplitude in the target region is 1.09 dB, and the maximum phase difference is 10.13 degrees, which is displayed in Figure 4.14. It can be noticed that the fluctuation of this case is larger than that of the square region case, as the sampling spots are more uniformly distributed in the square region case. In addition, the -3 dB point is 0.4λ away from the circular

edge of the focal region. In all, the NFMF array accomplishes a focusing on the circular region with a clear boundary in the near-field pattern for both amplitude and phase condition.

In two examples discussed above, the amplitude of power combining in the focal area is uniformly distributed. However, amplitude can be distributed consciously with different intensity according to the requirement of power combining. The vector $\mathbf{F}$ can be defined as

$$\mathbf{F} = \left[A_1 \exp\left(j\varphi_0 \right), \cdots, A_M \exp\left(j\varphi_0 \right) \right]^{\mathrm{T}}, \tag{4.6}$$

where the amplitude of each sampling spot can be arbitrarily defined, and the phase on each focal point is identical.

One example is shown for a power combining case with varied distributed amplitude in the focal area. The antenna array adopted has the same configuration as presented by the two examples above. The amplitude is identical along the z-axis, and it obeys sinusoidal distribution along the y-axis. The focal area is a square region with the same scale and location as the previous square region case.
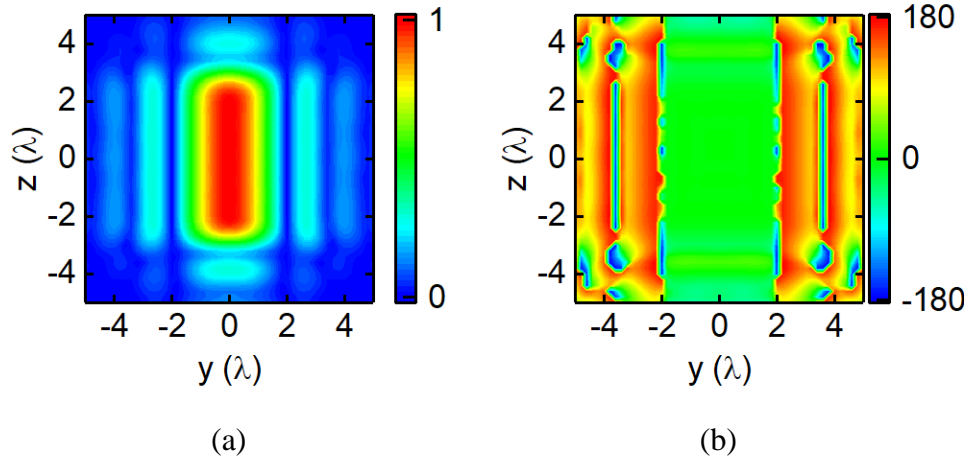
Figure 4.15 Spatial power combining on square region with: (a) sinusoidal amplitude (dB); (b) uniform phase (degree) distribution.

With the proposed algorithm, the near-field pattern is estimated and shown in Figure 4.15. The sampling spots have the same distribution as in Figure 4.9 but with different amplitude and phase. Along the y-direction the amplitude is distributed with sinusoidal distribution in (-2λ, 2λ). Along the z direction the amplitude is uniformly distributed, and the -3 dB point is located 0.6λ away from

the target focal region. The maximum phase difference in the focal area is 2.63 degrees (Figure 4.16). This example demonstrates that the spatial power combining can be accomplished with not only uniform but also specified assigned amplitude distribution.
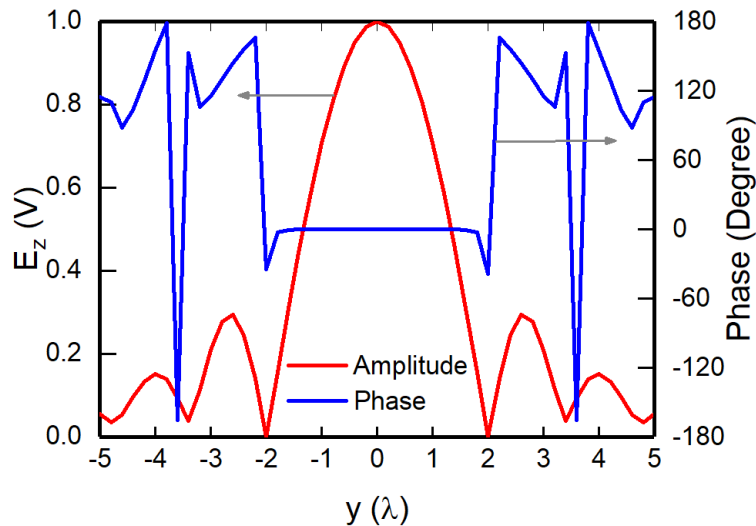
Figure 4.16 Field distribution of spatial power combining on square region with sinusoidal amplitude along $z = 0$ on focal plane.

To conclude, the proposed approach in this chapter is suitable for the outputs of special spatial distribution of certain shape or intensity. It is worth mentioning that the continuous region with either regular shape like in the above examples or irregular shape can be realized by the proposed method thanks to its ability of pattern shaping.

This focusing property results in energy directionally converging to certain region(s), which can be seen as a spatial power combining realized by a cluster of antenna elements with designated excitations (Figure 4.17(a)).

This approach also fits the power combining of multiple inputs with multiple clusters of antenna elements, where the signals of all inputs are projected in the identical region by different antenna element arrays with the identical distribution. The final output is the superimposed results at the targeting region(s), whose schematic is shown in Figure 4.17(b).
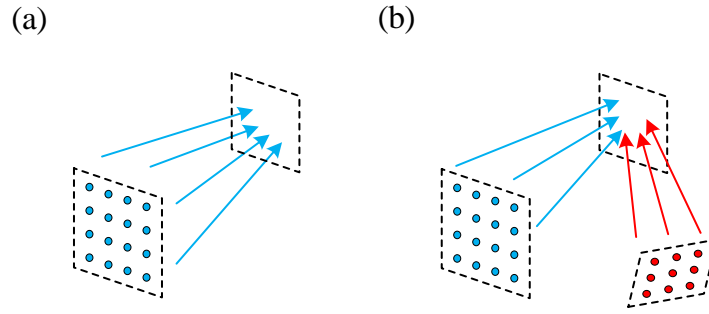
Figure 4.17 Spatial power combining: (a) schematic of spatial power combining with single source; (b) schematic of spatial power combining with multiple sources.

4.2.3 Spatial phase shifting

In the signal processing of devices or systems, the phase adjustment is a necessary segment for modulation, demodulation and other processes. The conventional approach of creating phase delay relies on a transistor-based phase shift module or transmission line formed phase shifter loaded with diodes or transistors. The common idea of phase shifters is based on the circuit model of a 2-port network. By tuning the parameter permanently or dynamically, the phase of S_{21} or S_{12} can fulfill the required phase delay. However, as the main idea of conventional solutions is based on the circuit model, it may come across some issues in dealing with the field model, particularly phase shift for multiple inputs and multiple outputs simultaneously, or with the phase shift for a vector field in spatially distributed areas.
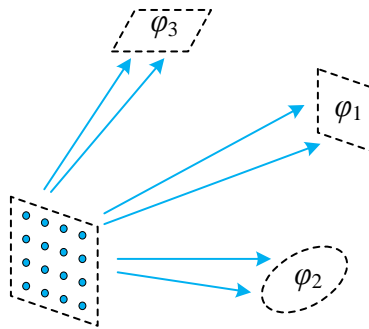
Figure 4.18 Schematic of multiple areas spatial phase shifting with identical or different phase delay in each region with specified shapes.

As we propose a spatial signal transmitting and processing approach with free space transmission, the main idea of our approach is based on the field model as we discussed in the last section. By taking advantage of this feature, phase shifter spatially distributed over single or multiple regions can be realized. For a spatial phase shifter, the phase of a vector field is uniform according to the required phase delay in each region. While for different regions, the phase delay is individually specified. Therefore, phase delay value on targeting spatial areas and the shape of each area can be arbitrarily defined as shown in Figure 4.18.

We take a common example of spatial phase shifter involving M sub-regions and uniform phase delay in each region, and their corresponding vector $\mathbf{F}$ is performed as

$$\mathbf{F} = \left[\overbrace{A_1 e^{j\varphi_1} \cdots A_1 e^{j\varphi_1}}^{Region\,1} \overbrace{A_2 e^{j\varphi_2} \cdots A_2 e^{j\varphi_2}}^{Region\,2} \cdots \overbrace{A_M e^{j\varphi_M} \cdots A_M e^{j\varphi_M}}^{Region\,M} \right]^{\mathrm{T}}. \tag{4.7}$$
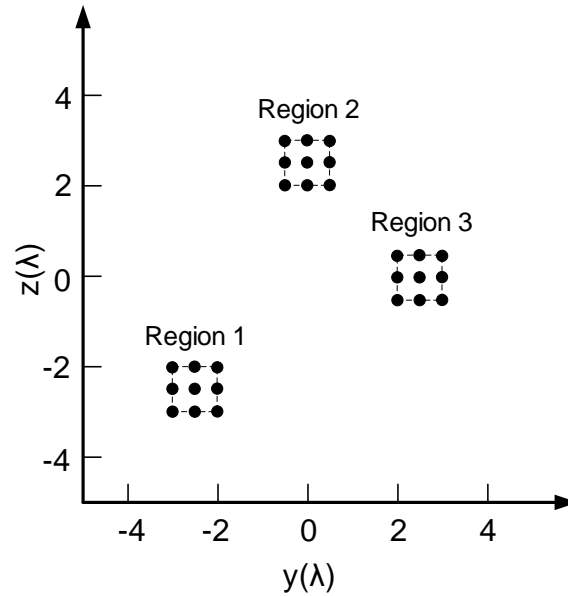
Figure 4.19 Distribution of sampling spots for NFMF in triple square regions (dashed line).

An example of the spatial phase shifter is estimated involving three square regions. The configuration of three focal regions is shown in Figure 4.19 with an edge of dashed line. Each region has a side length of λ, which is sampled by nine spots with a spacing of 0.5λ. In each focal region, the amplitude and phase are uniformly distributed. And the phase shift for each region is

different. The phase shift for regions 1, 2, and 3 is 90, 0, -90 degrees, respectively. The antenna array adopted has a scale of 16×16 patch antennas, and the focal plane is located at $x = -4\lambda$. The estimated results are shown in Figure 4.20 with a maximum difference of 0.77 dB in amplitude and a maximum phase difference of 6.29 degrees. The -3 dB point is 0.4λ away from the edge of focal areas.

(a)   (b)
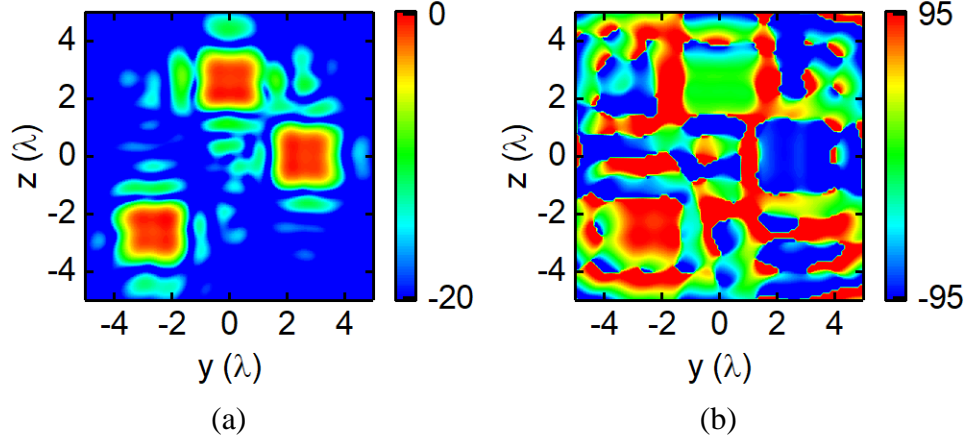
Figure 4.20 Spatial phase shifter: (a) example of spatial phase shifting on three square regions with uniform amplitude in each region; (b) corresponding phase delay of -90, 0, 90 degrees in each region.

The example presented in the above section demonstrates that spatial phase shifting can be accomplished in multiple areas with different phase conditions. And the phase shifting keeps a uniform distribution in each area. Moreover, the phase condition can be controlled to realize a specified distribution in single or multiple focal areas. Then the vector F for this condition should be defined as

$$\mathbf{F} = \left[\overbrace{A_1 e^{j\varphi_1} \cdots A_1 e^{j\varphi_{M_1}}}^{Region\,1} \; \overbrace{A_2 e^{j\varphi_2} \cdots A_2 e^{j\varphi_{M_2}}}^{Region\,2} \; \cdots \; \overbrace{A_M e^{j\varphi_M} \cdots A_M e^{j\varphi_{M_M}}}^{Region\,M} \right]^{\mathrm{T}}. \tag{4.8}$$

With the vector $\mathbf{F}$ defined in (4.8), an NFMF case with uniform amplitude and varied phase can be estimated. An example is shown in Figure 4.21, where the single focal region is the same as that shown in Figure 4.9, so does its corresponding antenna array and the locations of sampling spots. Moreover, the phase shift is continuously varied along the y-direction from -180 to 180 degrees and keeps constant along the z-direction in the focal area.

The results in Figure 4.22 illustrate that the phase is linearly varied along the *y*-direction as defined and the amplitude keeps uniform. The maximum variation of amplitude is 0.22 dB and the -3 dB point is 0.5λ away from the focal area. The linearity of phase variation is good and covers the entire 360 degrees in the focal area. It is worthwhile mentioning that regions with irregular shape or phase shifting with an arbitrary degree can be realized by adjusting the distributions of sampling spots and their corresponding vector **F** as (4.8).

(a) (b)
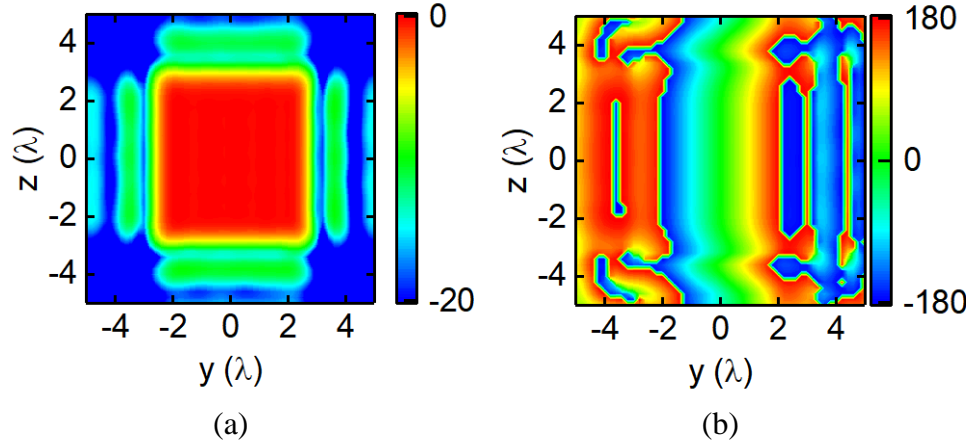
Figure 4.21 Spatial phase shifting on single square region with: (a) uniform amplitude (dB); (b) linearly varied phase (degree) distribution.
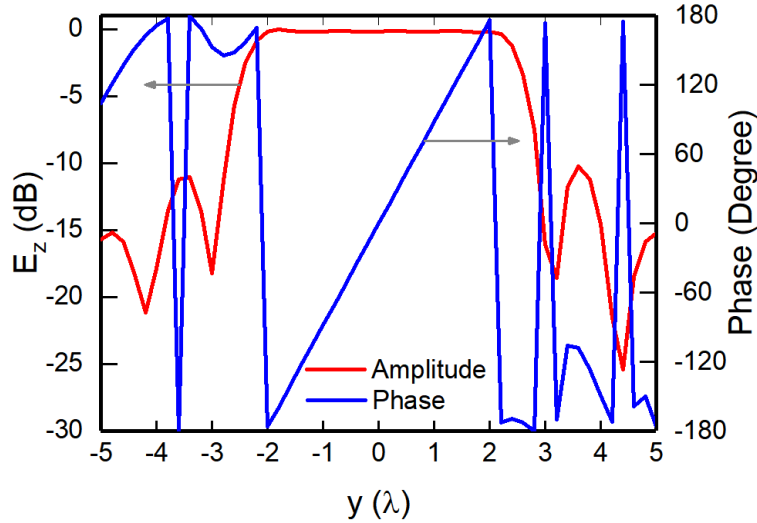
Figure 4.22 Field distribution of spatial phase shifting on square region with linearly varied phase along $z = 0$ on focal plane.

4.3 Components design

In the previous experimental validations (Section 3.5), the microstrip line-based experimental prototype of NFMF array was fabricated and tested in X-band with a good performance coincident with the theoretical estimation. As is known to all, microstrip line has a good transmission feature in low-end RF band. However, microstrip line introduces higher transmission loss as frequency increases to millimeter-wave band, while substrate integrated waveguide (SIW) features low transmission loss in the millimeter-wave band. In order to realize NFMF in the 5G and beyond systems with high power efficiency, feeding networks based on SIW transmission line are designed for the millimeter-wave band. In this chapter, the demonstration works are carried out over 28 GHz.

In order to feed the planar array with a large scale, an SIW based feeding network is designed with a schematic shown in Figure 4.23(a). The proposed feeding network has one input port located at the center of the entire feeding network, and the output ports are parallelly placed. The configuration is compact, which fulfills the requirement of an array design for millimeter-wave band. However, the feeding network itself can only accomplish a uniform power distributing on all output ports. Therefore, phase shifters and impedance transformers need to be designed and integrated into the feeding network to ensure the requirement of unequal feeding in both amplitude and phase.

4.3.1 End-loaded SIW feeding networks

One solution is loading phase shifter and attenuator before each end of the output port, which is displayed in Figure 4.23(b). In addition, the loaded devices need to have compact sizes as the space is limited for a compact feeding network for integrating multiple phase shifters and attenuators.

Several types of SIW-based phase-shifters have been proposed over the past decades. One typical sort of phase-shifter is derived from transmission line techniques such as delay-line, equal-length unequal-width [41] and self-compensating phase-shifter [42]. These phase shifters can change the electrical length of devices over certain frequency bands by either modifying the physical length of devices directly or adjusting the characteristic impedance of the transmission line. Therefore, changing the electrical length will lead to a phase shift. The second type of phase-shifter is based on loaded structures. Periodic posts loaded on SIW would form a resonator-based phase-shifter

[43], while posts distributed by certain shapes serve as a loaded network to modify the response of a phase-shifter [44]. Another type of phase-shifter is based on hybrid coupler topologies. In this case, reflected wave received by the output port is adjustable with variable loads of the hybrid coupler [45, 46].
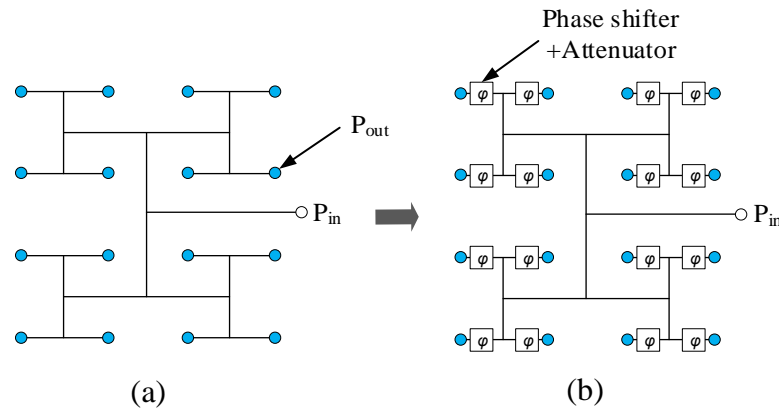
Figure 4.23 Configuration of parallel feeding networks: (a) conventional SIW based parallel feeding network for equal power distribution; (b) end-loaded parallel feeding network for unequal power distribution.

On the other hand, investigations and designs about SIW attenuators have also been carried out through several types. One is based on absorbing materials. In this case, the absorbing materials are pasted on the surface or inserted to the inner part of SIW to absorb travelling waves, and its absorbing capability can be enhanced with a zigzagged shape material [47, 48]. Another sort of attenuator is resistor-loaded, where the assigned attenuation is realized by loading resistors of different values calculated by a circuit model [49]. It can be concluded from the discussion that the SIW structures can effectively be used to realize phase-shifter and attenuator individually with required performances.

In our design, we combine these two functions together through one single SIW-based device with a compact profile, which would make it easy for its integration within large-scale SIW feeding networks with compact size [50].

The proposed circuit is sketched in Figure 4.24, whose building architecture is based on a folded SIW structure with two pieces. The top SIW serves as the input while the bottom one is the output part. These two pieces of SIW are connected with a coupling aperture by waiving part of the metal

on the metal layer shared by both top and bottom SIW geometries. Therefore, the signal from the input port is transmitted through the coupling aperture shared by those two SIW structures to the output port.
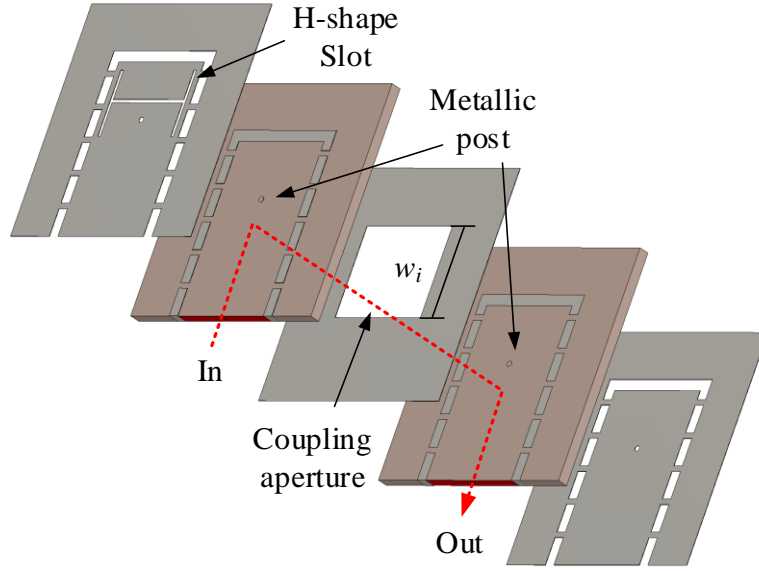
Figure 4.24 Architecture of SIW-based phase-shifter-attenuator.

Regarding the topology, the proposed folded SIW architecture is basically derived from the concept of a planar hybrid coupler. The schematic of a conventional hybrid coupler is shown in Figure 4.25(a). In this case, port 1 and port 2 serve as the input and output respectively while port 3 and port 4 are connected to the reflective loads. By tuning the reflecting phase of the loads, the output phase at port 2 changes. Thanks to this feature, the reflectively loaded hybrid coupler offers a way of phase-shifter design. However, this planar architecture is bulky for circuit integration especially in a compact feeding network. Therefore, the hybrid coupler is restructured through a folded SIW scheme (Figure 4.25(b)), which is compact and easy-to-design tailored for multi-layer integration. The red path indicated with a dashed line in Figure 4.24 shows the transmission of the proposed folded hybrid coupler. Then, an H-shaped slot load and a metallic post is adopted to serve as a common reflective load instead of two separate loads as deployed in a conventional hybrid coupler to reduce the complexity.

Based on this architecture, an equivalent circuit model of the entire device is shown in Figure 4.25(b). Power from the input port is transmitted through the coupling aperture, whose characteristic impedance Z_{02} can be changed with the width of the aperture along the longitudinal direction (w_i). As a result, the frequency response including phase and amplitude of the two-port network changes with w_i, which serves as a tuning element of the proposed circuit.
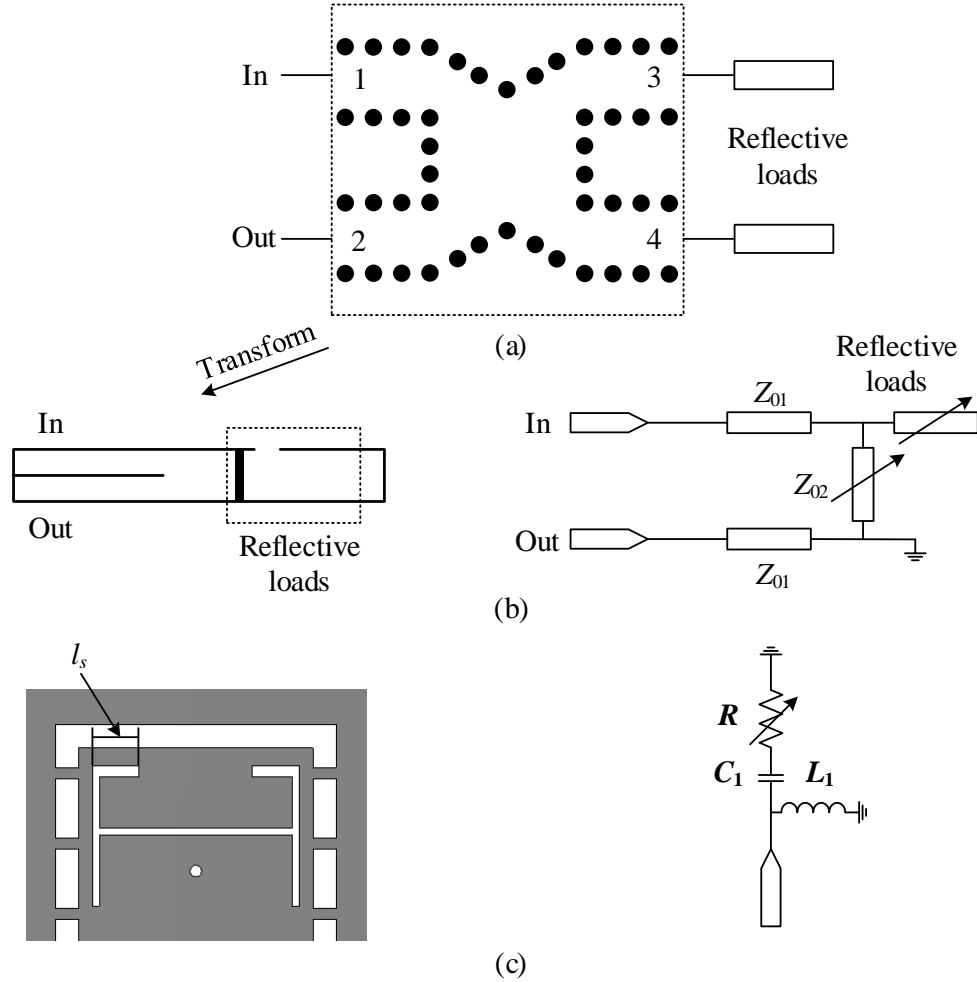
Figure 4.25 Configurations of conventional and proposed components: (a) conventional schematic of planar SIW hybrid coupler reflection type phase-shifter; (b) side view of the proposed folded SIW structure and its equivalent circuit; (c) reflective load in the proposed design and its equivalent circuit.

The reflective load in the proposed design also plays an important role in the output power tuning. As shown in Figure 4.25(c), the reflective load is a resonating structure in nature. Two slots parallel

to the longitudinal direction of SIW serve as a transformer in dealing with the characteristic impedance of SIW. The transverse slot connected to the longitudinal ones serves as a capacitive loading, which is represented by C_1 in the equivalent model in Figure 4.25(c). And the metallic post passing through the SIW structure acts as a shunt inductance (L_1). It is worth mentioning that two narrow slots symmetrically loaded near the shorted end serve as the resistors R in the equivalent circuit. As a result, the impedance of the reflected load can be tuned by the length of two short slots l_s. Moreover, l_s can be used as another tuning element of the entire circuit.
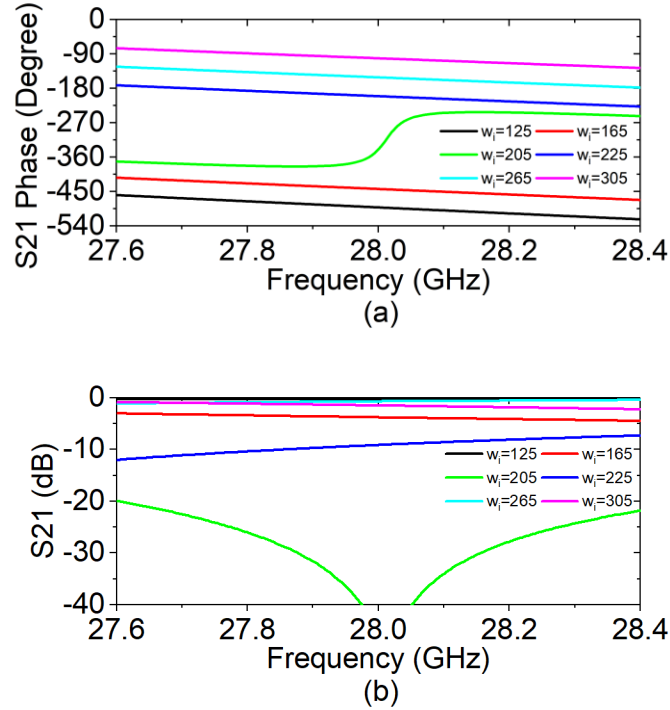
Figure 4.26 Frequency response of proposed device by tuning w_i (l_s = 46 mils): (a) S_{21} phase; (b) S_{21} amplitude.

To demonstrate the validity of the proposed device, multiple prototypes with an operating frequency of 28 GHz are fabricated. Each piece of the SIW structure is fabricated on RT/duriod 6002 substrates with thickness of 20 mils. To ensure a single-mode transmission at 28 GHz and also a quality impedance matching, the cut-off frequency of SIW is set around 18 GHz. The total length and width of this joint function device are respectively 0.75 λ and 0.56 λ, which feature a compact profile.

Full wave simulation is adopted for discussing the tuning effect of w_i and l_s by CST Microwave Studio. Simulated results versus w_i is displayed in Figure 4.26, suggesting that the output phase and amplitude of the proposed device can be tuned simultaneously. With a fixed $l_s = 46$ mils, the phase shift of S_{21} can cover more than 360 degrees with a varied amplitude at 28 GHz.

Figure 4.27 shows S_{21} results of the proposed device with reference to different l_s for a fixed $w_i =$ 185 mils. The amplitude of S_{21} varies with l_s as it mainly influences the resistance of the reflective load. However, the phase of S_{21} also changes in a certain range as the impedance of the reflective load also influence the entire output phase.

It can be observed that the output phase and amplitude tuning cannot be done independently as the influence of two tuning elements is correlated. Therefore, w_i and l_s must be tuned simultaneously to achieve certain phase and amplitude condition.
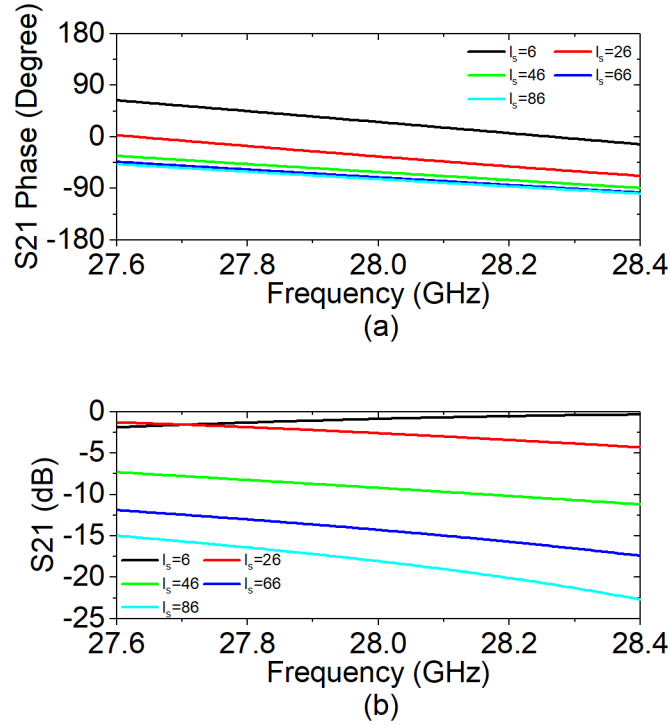
Figure 4.27 Frequency response of proposed device by tuning l_s ($w_i = 185$ mils): (a) S_{21} phase; (b) S_{21} amplitude.
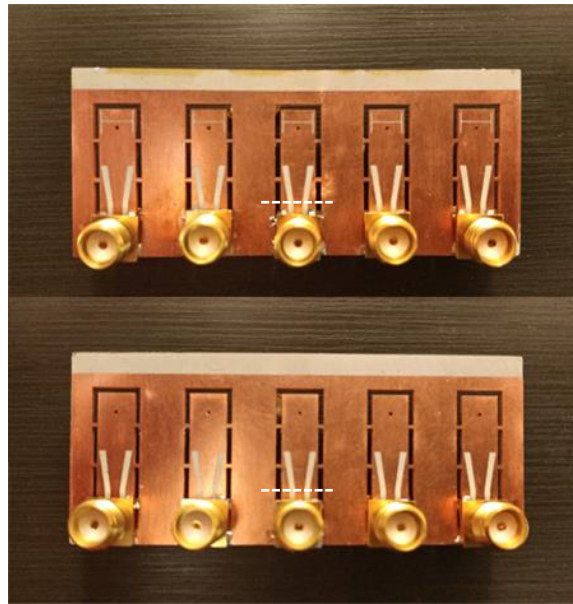
Figure 4.28 Top and bottom view of the prototypes of phase-shifter-attenuator circuit with microstrip to SIW transitions.

To further demonstrate the performance of the proposed design, several prototypes are fabricated and measured, which are shown in Figure 4.28. For the simplicity in measurements and comparisons, the input and output impedances of the proposed device are selected to be 50 Ohm with transitions from SIW to microstrip line. As the architecture is a folded SIW structure, the input and output ports are located back-to-back on the top and bottom sides of the proposed device. In order to test the two-port characteristics, SMA connectors are soldered vertically to input and output ports.

With the help of a TRL calibration, the two-port results are calibrated and measured. The dashed lines in Figure 4.28 are the reference line of calibration for top and bottom layer, respectively. The measured results are compared with simulated ones, as shown in Figure 4.29. The amplitude and phase results agree with each other well around 28 GHz in general with some discrepancy. This discrepancy is mainly introduced by the soldering conditions of the connectors and fabrication tolerance.

It is worthwhile mentioning that the transitions and connectors adopted in the prototypes are for the purpose of measurement only. For practical applications, the proposed device can be connected directly to other circuits with SIW ports without any vertical connectors, and it is easy to integrate,

especially for multilayer and compact topologies thanks to its SIW structure and compact profile. Therefore, by loading the proposed circuit to each end of the output port, the end-loaded feeding networks are accomplished.
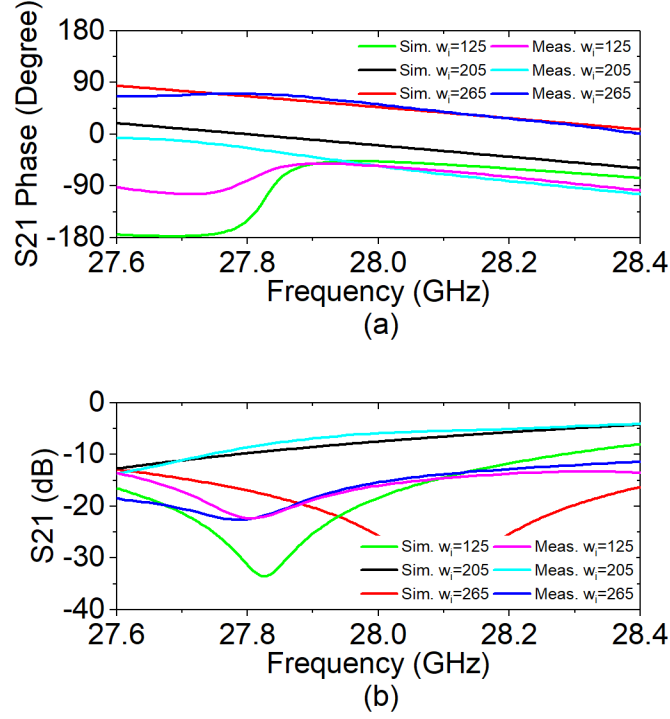
Figure 4.29 Results of prototypes with different w_i ($l_s = 0$ mil): (a) measured and simulated results of S_{21} phase; (b) measured and simulated results of S_{21} amplitude.

4.3.2 Distributed SIW feeding networks

The proposed end-loaded feeding networks offer a solution for unequal feeding. However, this configuration of feeding networks has its own disadvantages. The phase shifting and power splitting tasks are all accomplished by each device located at the end of output port as proposed in the last section. It leads to a problem of heavy load of phase shifting and power attenuating at each output port when the required phase and amplitude of each end differs a lot. Furthermore, the proposed devices would perform an obvious difference in their own characteristic impedance when they are assigned phase shift and attenuation with large difference. Therefore, the end-loaded feeding network is suitable for antenna array with small scale. In order to feed a large-scaled array, a distributed configuration of feeding networks is developed, which is displayed in Figure 4.30.
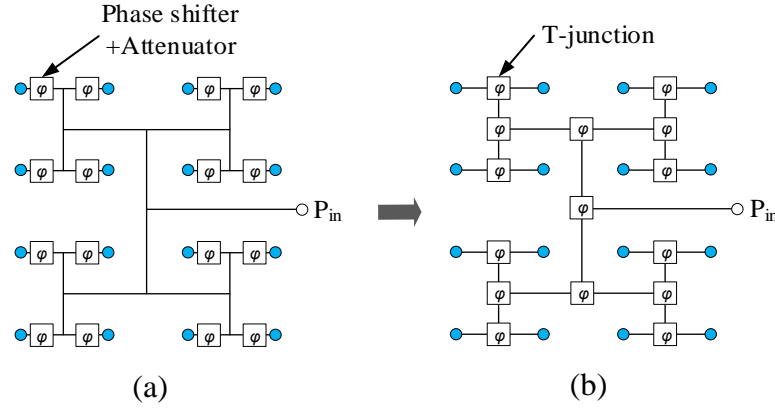
Figure 4.30 Configuration of feeding networks: (a) end-loaded parallel feeding network; (b) distributed parallel feeding networks.

Different from the early discussed end-loaded feeding networks, the distributed feeding networks distributes the task of phase shifting and power splitting to the entire feeding networks instead of only the end of each output port. In this way, the work load of allocating phase and amplitude is distributed to several levels according to the scale of feeding networks. Thus, device on each node of the parallel feeding network in Figure 4.30(b) shares only part of phase and amplitude allocating work, which reduces the designing requirement of phase and amplitude allocating devices a lot and achieve a better performance of impedance matching.

In the proposed distributed feeding networks, the component for phase and amplitude allocating on each node is the feeding network itself with metallic posts loaded. Thanks to its parallel structure, each node of the feeding network can be seen as a T-junction. In the research regarding power splitter, waveguide-based T-junctions are commonly used for unequal power splitting. As SIW shares similar features as traditional waveguides, SIW-based T-junctions are also adopted as power splitter with good performance. In a paper written by Park, etc., they added metallic posts to T-junction to control the power ratio of two output ports [51]. However, the function of the T-junction can be further extended other than allocating of output power.

Inspired by the structure shown in [51], we expand the function of T-junction as an allocator for power and phase simultaneously. The configuration of the proposed T-junction is shown in Figure 4.31. Port 1 serves as the input port of the T-junction while port 2 and port 3 are the output ports, which is coincident with the configuration of the distributed feeding networks. Different from the

conventional T-junctions, the metallic walls between two output ports are modified as curved ones to reduce the reflection to the input port, it also serves as an approach for impedance matching for the output ports. Three metallic posts are loaded through the T-junctions for tuning purpose. Post a_1 is loaded close to the curved wall, and it is originally located at the vertical axis of symmetry of the T-junction. Post a_2 and post a_3 are symmetrically placed with a fixed distance between each other. When all the posts are placed on the original place, the distance between a_1 and curved wall, and the distance between a_2 and a_3 need to be adjusted to ensure an impedance matching condition of port 1 at the target operating frequency (28 GHz) as well as equal power and phase condition at port 2 and port 3.
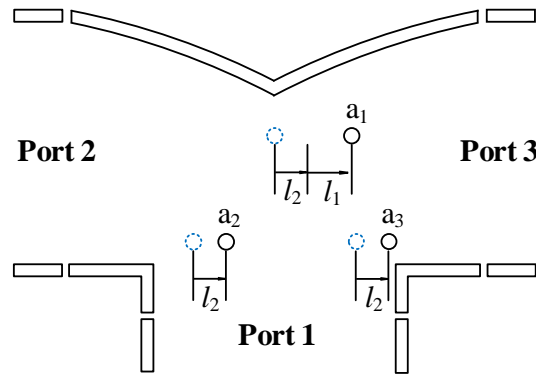
Figure 4.31 SIW T-junction featuring a function of power and phase allocation.

Afterwards, the location of a_1 is adjusted horizontally with a distance of l_1 to realize unequal power allocation between the two output powers. Then, three metallic posts are moved together horizontally with a distance of l_2 to adjust the phase difference between the two output ports. With this approach, the phase and amplitude of the two output ports can be allocated simultaneously.

By shifting the location of three posts horizontally, the phase difference and power ratio between the two output ports (port 2 and port 3) are shown in Figure 4.32. For power allocation, the power ratio between port 2 and port 3 increases as l_1 increases (a_1 moves from left to right side). For phase tuning, the phase difference increases when l_2 decreases (all posts move from right to left side). Compared with what is presented in the last section, the variance of amplitude and phase is more regular and easier to estimate as they are almost linear according to the simulation results.

Furthermore, the T-junction needs to keep a good matching condition as they are cascaded in the feeding networks, where a good matching of the input port would reduce the reflection and thus keep the accuracy of phase and amplitude allocating.

In this case, the region where S_{11} has a value lower than -10 dB as shown in Figure 4.32(c) is defined as the available area of amplitude and phase tuning. The boundary of this area is also depicted with the dashed line in Figure 4.32(a) and (b). According to the simulation results, the proposed single T-junction can accomplish outputs with maximum (-90, 90) degree phase difference and (-10, 10) dB power ratio. This range can be further extended with multiple T-junctions cascaded in the proposed feeding networks.

To conclude, the proposed T-junctions are able to adjust the phase difference and power ratio simultaneously when they are loaded at the nodes of distributed feeding networks. This solution has a better performance compared with the end-loaded feeding networks proposed in the last section when the feeding networks have a large scale of outputs.

(a)   (b)   (c)
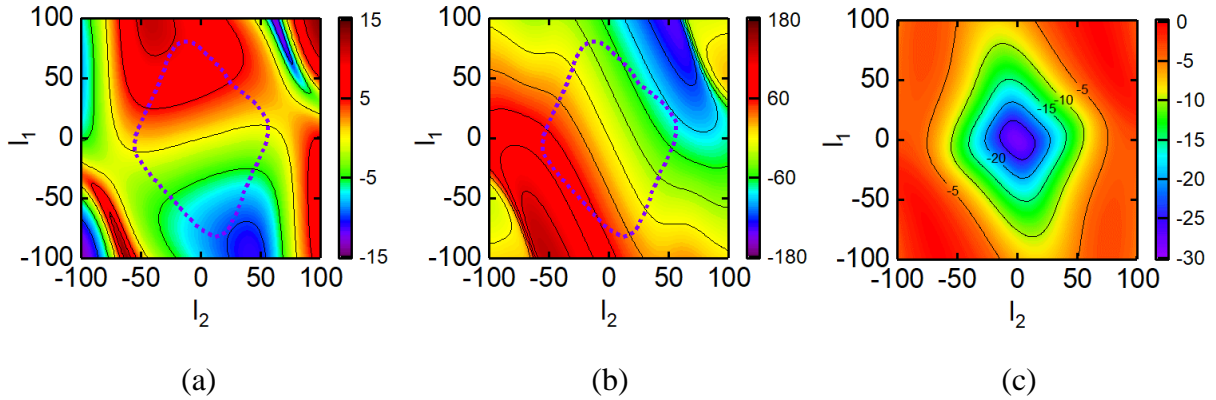
Figure 4.32 Simulation results of amplitude and phase tuning of SIW T-junction with different l_1 and l_2: (a) amplitude ratio (dB) between output ports 2 and 3; (b) phase difference (degree) between output ports 2 and 3; (c) S_{11} (dB) of T-junction.

4.4 Fabrication and experiments

To demonstrate the proposed concept, an example of power splitter in the millimeter-wave band (28 GHz) and its configuration are described as follows. As mentioned above, the distributed parallel feeding networks are adopted as the feeding mechanism of the entire antenna array, which is located at the bottom layer of entire circuits on substrate 2 which is shown in Figure 4.33.

Electromagnetic power transmitted to each output port of feeding networks serves as the excitation of corresponding antenna element on the top layer, which is transmitted through a vertical coaxial probe between two layers of substrates. The top layer on substrate 2 is occupied by the antenna array, where the patch antenna is designed and simulated through CST Microwave Studio and its field model is estimated by the infinitesimal dipole model. So far, the NFMF array is accomplished through antenna array and its corresponding distributed feeding networks.

To verify the performance of the proposed approach and architecture, an experimental prototype of the NFMF array is designed and fabricated. The prototype is designed with a function of power splitting on nine discrete points. The focal points are located on the plane x = -8λ with a 3×3 matrix form, whose central focal point is located at (-8λ, 0 ,0) and the neighboring focal points share a common spatial distance of 2.8λ along *y*- and *z*-direction on the same plane.
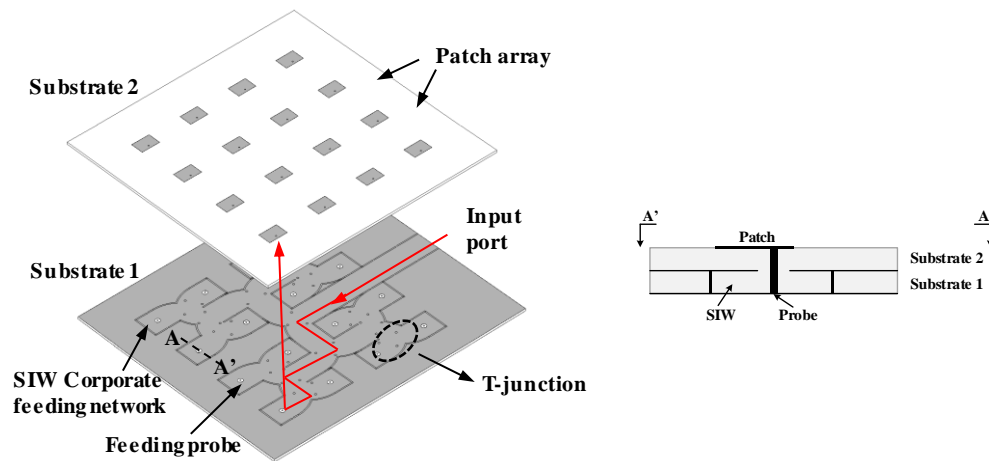
Figure 4.33 Configuration of millimeter-wave NFMF array and corresponding feeding networks.

By applying the NFMF method proposed in this chapter, the configuration of the prototype is designed and fabricated, which is shown in Figure 4.34. The prototype contains two layers. The top layer is a printed 4×4 linear polarized patch antenna array on an RT/duroid® 6002 substrate (20 mil) with a spacing of λ at 28 GHz. The bottom layer is a printed SIW based distributed feeding network with a single input and 4×4 outputs connecting to the corresponding patch antenna through a vertical pin traversing the two layers. The feeding of the entire prototype is accomplished by the end-launch connector located at the input port of feeding networks.

(a)   (b)
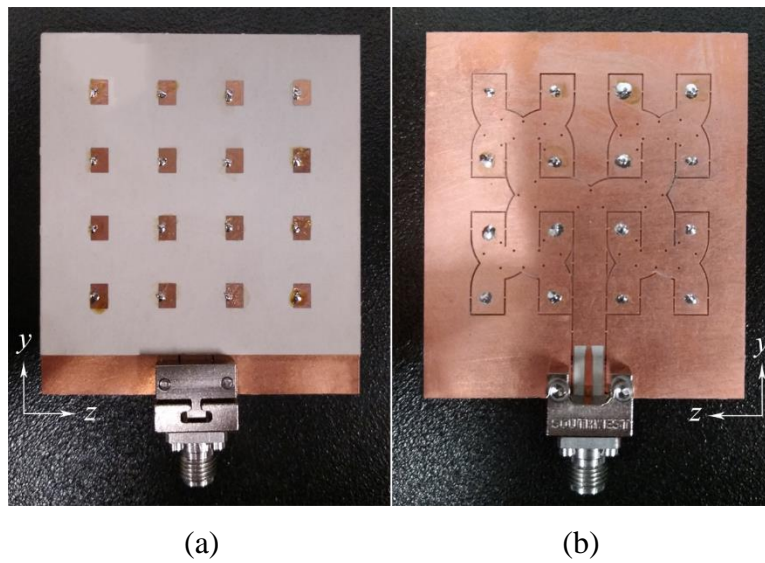
Figure 4.34 Prototype of 4×4 NFMF array: (a) antenna array as top layer; (b) corresponding distributed feeding network as bottom layer.

The experimental demonstration is accomplished in the Poly-Grames Research Center with a near-field testing platform. The schematic of the entire testing environment and the connection scenario between devices are shown in Figure 4.35.
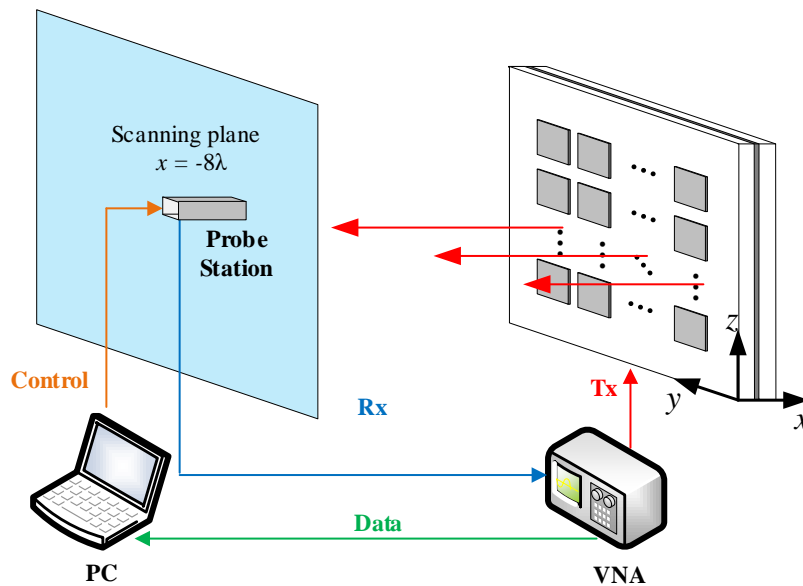
Figure 4.35 Schematic of testing environment.
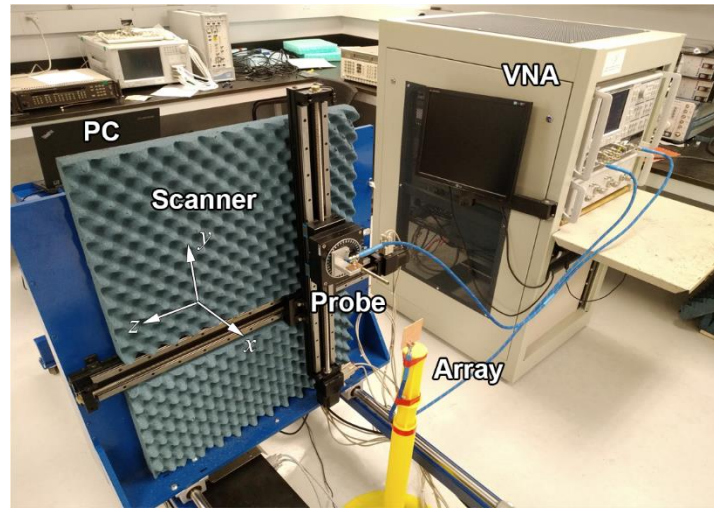
Figure 4.36 Practical testing environment for near-field scanning of 4×4 NFMF array.

Different from the configuration in Chapter 3, E-field values in the near-field region are collected by a waveguide probe at 28 GHz, which scans the focal plane parallel to the antenna array with a distance of 86 mm (approximate 8λ). The probe's movement is controlled by the probe station based on the motion controller with a step of 2 mm (0.18λ) in a range of (-54, 54) mm (10λ) in both the y- and z-direction. The E-field value is measured from 27 to 29 GHz (101 points). The photo of the experimental setup is depicted in Figure 4.36.
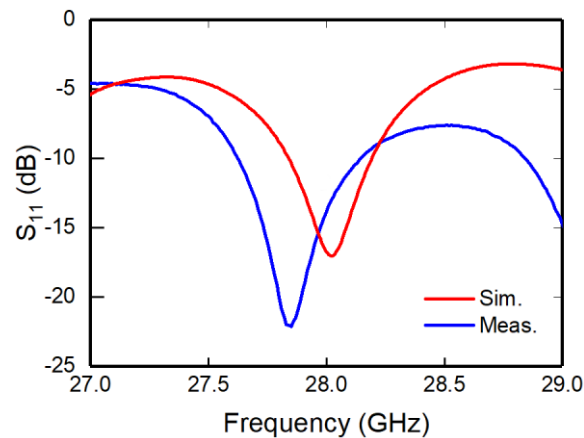
Figure 4.37 Simulated and measured S_{11} of fabricated prototype.

The reflection coefficient of the antenna array is measured by PNA network analyzer Keysight N5224B. Measured S_{11} has the same trend as its simulated counterpart with a 150 MHz frequency

shift compared with a designed operating point (28 GHz), which is displayed in Figure 4.37. This deviation is mainly caused by the limitation of accuracy in the process of fabricating and assembling PCB boards.

(a)   (b)
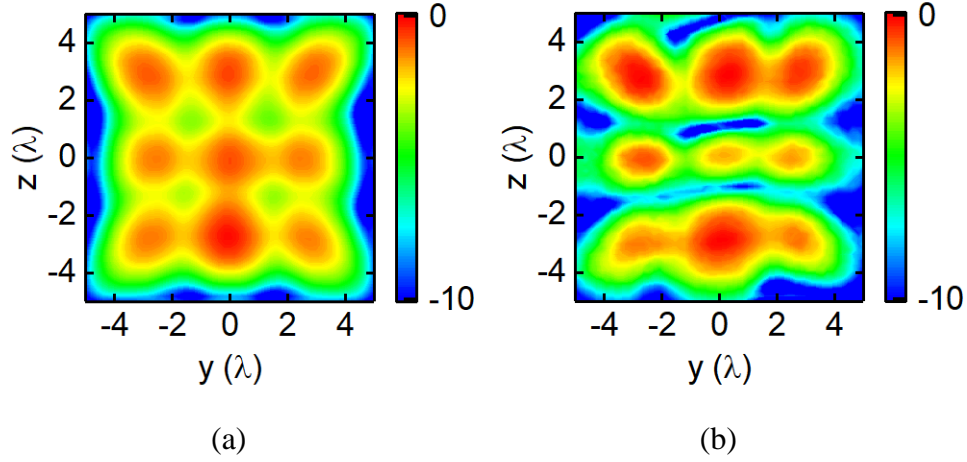
Figure 4.38 Near-field pattern of prototype: (a) simulated performance of prototype involving nine discrete converging targets on plane $x = -8\lambda$ with a matrix form distribution; (b) measured performance of prototype.

Table 4.3 Focal points and normalized amplitude of NFMF array prototype

Focal point (y_f, z_f)	(-2.8, -2.8)	(-2.8, 0)	(-2.8, 2.8)
Simulation (dB)	-1.20	-0.15	-1.28
Measurement (dB)	-0.12	-0.08	-0.57
Focal point (y_f, z_f)	**(0, -2.8)**	**(0, 0)**	**(0, 2.8)**
Simulation (dB)	-1.33	-0.78	-1.30
Measurement (dB)	-0.78	-1.67	-1.50
Focal point (y_f, z_f)	**(2.8, -2.8)**	**(2.8, 0)**	**(2.8, 2.8)**
Simulation (dB)	-0.92	-0.70	-1.02
Measurement (dB)	-1.28	-0.05	-1.15

Simulated and measured results are shown in Figure 4.38. The maximum displacement of focal points of measured results is 0.27λ in Figure 4.38(b). The normalized amplitude of each focal points is shown in Table 4.3 for simulated and measured results, respectively. The maximum difference is 1.18 dB for simulation and 1.62 dB for measurement.

The measured results show a good agreement at each central position of targets. However, the shape of each target is slightly different from the simulated results. The deviation from the measured results is mainly introduced by the fabrication process and testing deviation.

4.5 Conclusion

In this chapter, we have developed a pattern tuning-based method for designing NFMF array. With this method, the excitations for the NFMF array can be calculated analytically to deal with multi-focus on either discrete points or continuous areas with specified field distributions.

Furthermore, a novel signal processing approach called spatial signal processing approach is proposed based on the proposed method. With this method, the traditional transmission route is converted into a more flexible spatial radiation route between localized devices to reduce complexity. Simulation and experimental works indicate that the fundamental function of circuit-model-based signal processing including power splitting, power combining, and phase shifting can be accomplished. The proposed approach is also promising for applications that rely on spatially distributed vector fields, which offers an exciting way of designing field-model-based wireless systems.

CHAPTER 5   NFMF ARRAY FOR POLARIZATION DIVERSITY

Polarization is an essential index influencing the quality of the communication systems involving multiple users and multiple targets. In this chapter, a method of developing antenna array with a function of polarization allocation at multiple targets in the near-field region is presented. An algorithm for modeling NFMF array with a function of arbitrarily specified polarization of multiple focal points or focal regions is proposed and developed. The formulation of the proposed modeling algorithm is based on the conjugate-phase approach, which is further improved in this chapter with a function of defining the polarization direction and isolation at multi-targets. With regards to the physical realization, a hybrid near-field array is proposed, and an SIW-based arbitrary amplitude and phase feeding network is developed and adopted to feed the showcased near-field patch array. Several examples are presented and discussed to demonstrate the performance in different application scenarios. Again, an experimental prototype is fabricated and tested to verify the validity and accuracy of the proposed method.

5.1 NFMF algorithm for polarization allocation

The polarization direction of an antenna or array is fundamentally determined by its radiated E-field. E-field, as a vector field, can be regarded as a combination of orthogonal field components in a common coordinate system. Therefore, theoretically arbitrary polarization direction on certain spatial location can be achieved by a group of antennas with orthogonal polarizations. In the near-field region, a numerical algorithm based on weighting functions [14] is able to tune the field component along each axis. However, the analytical algorithm based on the conjugate-phase approach discussed in the previous chapters is only suitable for pattern shaping along single polarization as the antenna elements are assumed to be identical.

5.1.1 Polarization allocation

In order to develop an analytical solution for spatial polarization allocation in the near-field region, the conjugate-phase approach is thus improved and further expanded in this thesis. According to the NFMF method presented in Chapter 2, the multi-focusing technique for the near-field region is the result of a superposition of multiple field patterns. For each pattern, E-field concentrated at one target in the near-field region as the excitations of antennas obeying conjugate-phase approach.

Furthermore, by tuning the intensity of each pattern prepared for superposition, the superimposed pattern would create specified intensity on multiple targeting locations. For instance, a planar array with N identical elements focuses on M focal points with specified amplitude and phase in the near-field region. Then at the target points, the E-field can be generated by the solution formulated in Chapter 4 as follows.

$$\mathbf{F} = \sum_{m=1}^{M}\left[T_m \sum_{n=1}^{N}\mathbf{E}_{nm}C_{nm}\right],$$ (5.1)

where $\mathbf{F}$ is a vector representing the complex field value of M focal points; T_m is the tuning factor for m_{th} pattern; $\mathbf{E}_{nm}$ is the vector E-field transmitted by n_{th} antenna to m_{th} focal point with unit excitation and $C_{nm}=\exp(j\varphi_{nm})$ is the corresponding conjugate-phase. Rewriting (5.1) as a matrix form, we have

$$\left[\mathbf{F}\right]_{M\times1} = \left[\mathbf{C}\right]_{N\times M}^{T}\left[\mathbf{E}\right]_{N\times M}\left[\mathbf{T}\right]_{M\times1}.$$ (5.2)

Upon specification of the coordinates, amplitude and phase of focal points $\mathbf{F}$, the corresponding tuning vector can be derived by (5.2), and the excitations of antenna array are then calculated by $[\mathbf{C}][\mathbf{T}]$.

However, the above-stated algorithm is only suitable for single polarization as all the elements in the array shares the same polarization. To extend the algorithm for a diversified polarization allocation, a hybrid array consists of sub-arrays with different polarizations are introduced. Let us assume that the entire array is composed of two sub-arrays with vertically and horizontally linear polarization, respectively. The conjugate-phase approach is applied to the vertically polarized sub-array for vertically polarized focal points, whereas the same is applied to the horizontal polarization scenarios. The equation for this hybrid case is formulated as

$$\begin{bmatrix} F_V \\ F_H \end{bmatrix} = \begin{bmatrix} C_V & 0 \\ 0 & C_H \end{bmatrix}^{T} \begin{bmatrix} E_{V,V} & E_{V,H} \\ E_{H,V} & E_{H,H} \end{bmatrix} \begin{bmatrix} T_V \\ T_H \end{bmatrix},$$ (5.3)

where $F_V(F_H)$ stands for E-field at the vertically(horizontally) polarized focal points; $C_V(C_H)$ represents the conjugate-phase coefficient for vertical(horizontal) sub-array; $T_V(T_H)$ means the tuning vector for vertical(horizontal) sub-arrays; $E_{V,H}$ is the vertical E-field component on

horizontally polarized focal points which is radiated by the vertical sub-array. According to (5.3), the total field distribution radiated by both vertical and horizontal sub-arrays on all focal points are subject to the principle of superposition. Thus, the excitations for vertical sub-array can be calculated by $[C_V][T_V]$ and similarly for horizontal sub-array, the excitations are $[C_H][T_H]$. It is worth mentioning that the coordinates and quantities of vertical and horizontal focal points can be separately defined as fields on the focal points, which are mainly determined by their corresponding sub-array according to their polarization.

If the polarization direction of a focal point is arbitrary defined neither along horizontal nor vertical direction, vector $\mathbf{F}$ needs to be redefined. As the E-field can be decomposed into the horizontal and vertical components for the i_{th} focal point with arbitrary polarization,

$$\vec{F_i} = F_{iV}\mathbf{v} + F_{iH}\mathbf{h} , \tag{5.4}$$

where $\mathbf{v}$ and $\mathbf{h}$ are the unit vectors along vertical and horizontal direction respectively. As a result, the focusing along an arbitrary location with an E-field, $\vec{F_i}$, is equivalent to the superposition of one vertical polarized focusing pattern with field value of F_{iV} and one horizontal polarized focusing pattern with field value of F_{iH} at the same location. Thus, for multiple focal points with a scale of M, the scale of F is doubled as $2M$:

$$\mathbf{F} = \left[F_{1V} ,\cdots, F_{MV} , F_{1H} ,\cdots, F_{MH} \right]^{T} . \tag{5.5}$$

And the corresponding pattern is

$$\mathbf{F} = \begin{bmatrix} C_V & 0 \\ 0 & C_H \end{bmatrix}^{T} \begin{bmatrix} E_{V,V} & E_{V,V} \\ E_{H,H} & E_{H,H} \end{bmatrix} \begin{bmatrix} T_V \\ T_H \end{bmatrix}. \tag{5.6}$$

It is worth mentioning that $E_{V,H}$ and $E_{H,V}$ in (3) are replaced by $E_{V,V}$ and $E_{H,H}$ as each vertical pattern has its corresponding horizontal pattern with the same location. T_V and T_H share the same scale of M.

It should also be noticed that if the focal points are polarized along either vertical or horizontal direction, the number of the focal points is equal to the dimension of $\mathbf{F}$. However, in the arbitrarily polarized case, the quantity of the focal points is a half of the dimension of $\mathbf{F}$ as two elements in $\mathbf{F}$ represent one focal point in this case.

5.1.2 Cross-polarization isolation

Cross-polarization isolation is an important feature for polarization diversity, which influences the signal-to-noise ratio (SNR) of communication and other wireless systems. For NFMF, multiple focal points are distributed in the near-field region, a cross-polarization level of one focal point influences not only itself but also the other nearby focal points. As a result, an effective method of controlling such a cross-polarization should be studied and developed.

According to the algorithm developed in the last section, tuning vector T_V and T_H are derived, which is concerned with a specified E-field on focal points, leading to an excellent estimation of focal points or areas. However, the side-lobe of each pattern would influence the surrounding areas of other focal points when the patterns are superimposed. In order to manage the cross-polarization isolation, the SLL of pattern for each single focal point needs to be controlled.

Since each pattern used for single point focusing is based on the principle of the conjugate-phase approach, amplitudes of all antenna elements in a sub-array are identical. As a result, this sub-array can be seen as a uniform array with the assigned conjugate phase. For example, a conjugate-phase uniform linear array with 16 elements can yield a near-field AF shown in Figure 5.1 with green curve. It is noticeable that the side-lobes occur around the main lobe with suppression of 13 dB. If these side-lobes can be further suppressed or controlled, better cross-polarization isolation can be achieved.

The conjugate-phase approach aims at constructing an in-phase condition at a specified focal point, which converges a maximum superposition of power at the focal point. Therefore, the amplitude of each antenna is not a decisive factor for the conjugate-phase approach. Therefore, we can improve the amplitude distribution of the conjugate-phase approach to achieve the goal of controlling the SLL.

In the conventional design process of far-field arrays, binomial and Dolph-Chebyshev weights [52] were adopted as amplitude weights to control the SLL. In this work, these two weights are also adopted as amplitude weights for the near-field array. Moreover, the revised conjugate-phase coefficient can be rewritten as

$$\overline{C}_{nm} = w_{nm} C_{nm} , \tag{5.7}$$

where $\bar{C}_{nm}$ is the conjugate-phase coefficient modulated with corresponding weight w_{nm}, and w_{nm} is decided by the type of weight adopted and the spatial location of antenna elements.

Similar to the conclusion drawn in the conventional array theory applicable to the far-field cases, the modulated amplitude conjugate-phase array has its own features on its pattern through different types of weights. Figure 5.1 displays the near-field AF for binomial and Dolph-Chebyshev linear arrays where the uniform array has the thinnest beam width and highest SLL; the binomial array has the widest beam width with the lowest SLL; and the Dolph-Chebyshev array has both intermediate beam width and SLL. Compared with the other two arrays, the Dolph-Chebyshev weights give out a good trade-off between beam width and SLL and it can be controlled by side-lobe parameter α according to its definition [53]. Consequently, the Dolph-Chebyshev array is adopted for the side-lobe controlling method in the near-field array. Furthermore, specified cross-polarization isolation on multiple focal points can be achieved by multiple patterns adopting multiple Dolph-Chebyshev weights with corresponding side-lobe parameter α.
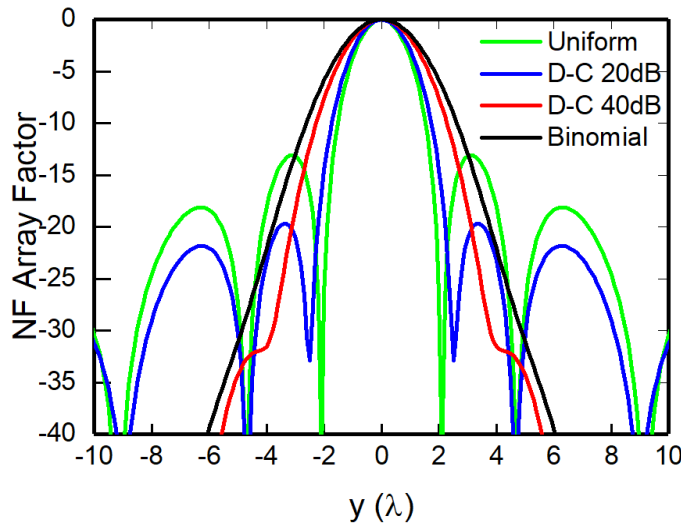
Figure 5.1 Near-field AF calculated at a distance of 8λ away from linear array of 10 antenna elements with conjugate-phase and different amplitude weights w including: uniform weight (green line); Dolph-Chebyshev weight with 20 dB SLL (blue line); Dolph-Chebyshev weight with 40 dB SLL (red line); binomial weight (black line).

5.2 Components design

A physical realization of the polarization diversity on multiple targets requires two conditions, namely, a near-field array whose polarization direction can be flexibly tuned and excitations with varied amplitude and phase for each antenna in the array. To fulfill the requirements, hybrid dually-polarized array and an SIW-based arbitrary amplitude and phase feeding network are developed and presented.

5.2.1 Interwoven array

In the conventional design of a dually-polarized array for far-field transmission, each antenna features dual-polarization and the entire array consists of identical antenna elements. This topology can ensure a stable polarization in the far-field region. However, it is not suitable for multi-target polarization allocation since it cannot offer a controllable E-field ratio between horizontal and vertical field components. Therefore, a hybrid array that contains both horizontally and vertically polarized antennas is studied and developed. In the hybrid array, identical linearly polarized antennas are adopted, which are organized along horizontal or vertical direction as two sub-arrays are set to generate the E-field with orthogonal polarizations.

The topology of the sub-arrays is mainly determined by the spatial distribution of the focal points. As it was discussed in the previous chapters that the focusing resolution and corresponding focal width reach the minimum value when a focal point is placed along the broadside of array, and these two parameters get degraded as the focal point moves to the end-fire of array. Thus, each sub-array should be arranged to ensure the focal points are distributed close to its broadside so to enhance the cross-polarization isolation.

For instance, in one condition that vertically polarized focal points and the horizontally polarized points are respectively concentrated in two different areas, the topology shown in Figure 5.2(a) is adopted, where each sub-array is placed to cover the corresponding polarized focal points along the broadside of sub-array. However, if the focal points are arbitrarily distributed or their polarizations are arbitrarily assigned, the above-mentioned topology cannot work decently as it is not able to realize an identical focal width and resolution at the same coordinate in both vertical and horizontal polarization scenarios.

Therefore, a hybrid array made of "interwoven" topology is developed and presented in Figure 5.2(b). In this array, vertical and horizontal polarization-based antennas are closely interwoven like fabric products. With this topology, the vertically and horizontally polarized sub-arrays share similar apertures with almost the same resolution and focal width at the same spatial location. Therefore, a focal point with arbitrary polarization can be realized with decent cross-polarization isolation in its neighboring area. Furthermore, each antenna in the array is surrounded by antennas with its orthogonal polarization, which allows reducing the mutual coupling among antennas compared with conventional linear polarized arrays. In addition, in an $N_a \times N_b$ array, each sub-array has an exact or nearly half-number of antennas due to the interwoven architecture of array. However, each sub-array has a multi-focus performance comparable with an $N_a \times N_b$ linear array even though it has only a half of the antennas. This phenomenon can be explained by the principle of the conjugate-phase approach. The focusing performance is mainly decided by the number of antennas along each axis. Even though in a sub-array, the neighboring element of each antenna is not in the same column and row, it still serves as an effective element when considering the resolution along vertical or horizontal directions. In all, the proposed interwoven array can be a broadly applicable solution for polarization diversity in NFMF.
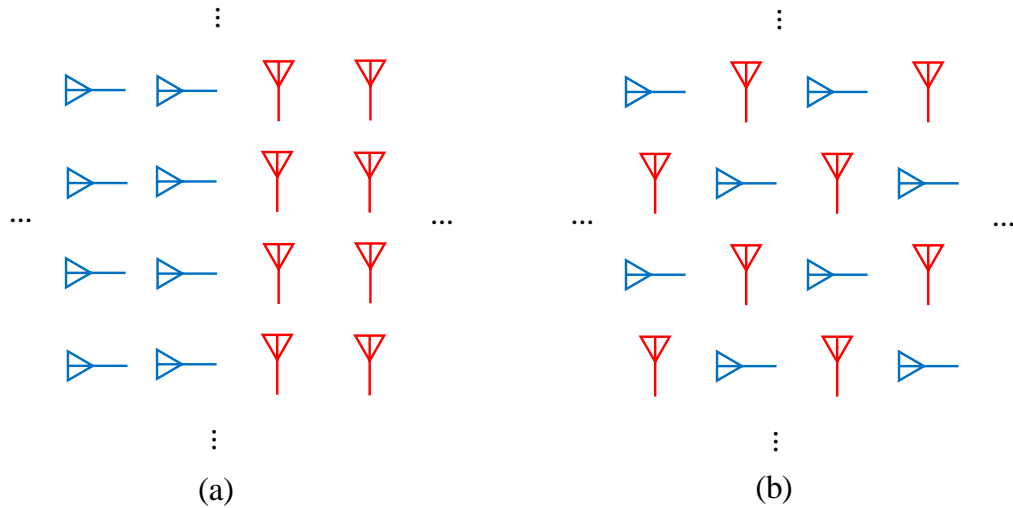
Figure 5.2 Two types of architectures of dual-polarization near-field antenna array: (a) hybrid array with separated vertically and horizontally polarized sub-arrays; (b) hybrid array with interwoven-style vertically and horizontally polarized sub-arrays.

5.2.2 Feeding network

As the values of excitations for antennas in the NFMF are independent from each other, feeding networks with multiple outputs that offer arbitrarily defined amplitude and phase are necessary. Therefore, SIW-based multi-output feeding networks were developed as the excitations of the near-field array in Chapter 4.

Figure 5.3 Proposed T-junction for amplitude and phase allocation: (a) original design of feeding networks tuned by two parameters along horizontal direction; (b) schematic of improved T-junction including three geometric parameters l_1, l_2 and l_3 introduced for tuning purpose.

Figure 5.4 Equivalent model of the proposed T-junction.

The general architecture of the proposed design is a parallel feeding network for a planar array. The parallel feeding network has been widely used as the feeding network of antenna arrays [54] as it offers a balanced power to all output ports with regular locations, which can meet the

requirement of a uniform array for far-field radiation. Furthermore, this feeding network fits the condition of unequal feeding.

As was discussed in Chapter 4, the parallel feeding network is a combination of T-junctions, and each T-junction can be used as a power and/or phase divider when it is loaded by metallic posts as shown in Figure 5.3(a). With the help of cascaded T-junctions where metallic posts are loaded at carefully calculated locations, the output ports offer varied amplitude and phase in a certain range. However, the tuning range of the entire feeding networks is affected by the performance of each T-junction. S_{11} of each T-junction needs to be low enough, for example lower than -10 dB, to keep a stable impedance of the entire feeding network. With this restriction, the tuning range of a T-junction is limited, as is displayed in Chapter 4, to maximum (-90, 90) degree phase difference and (-10, 10) dB power ratio.
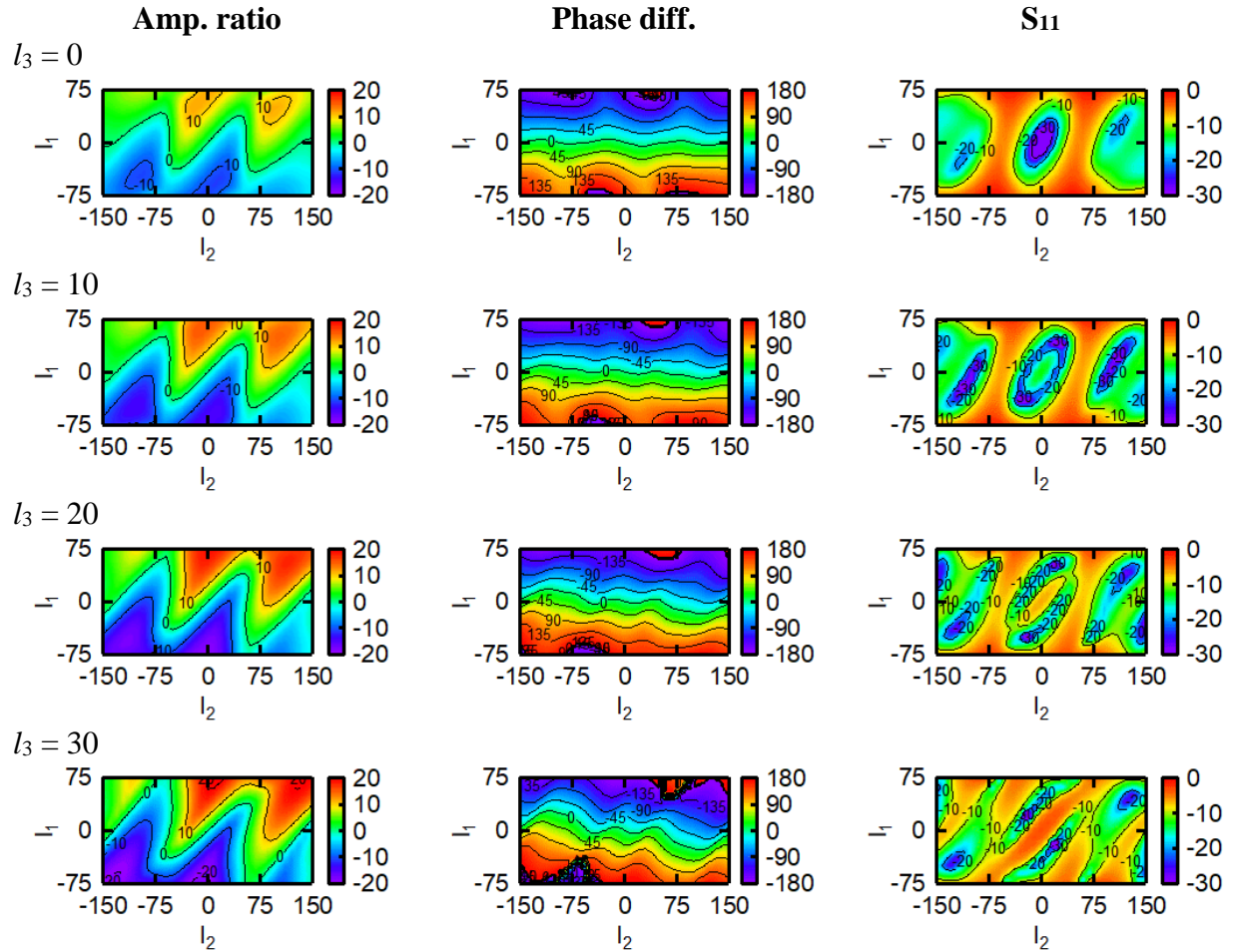
Figure 5.5 Amplitude and phase tuning results of the T-junction with different l_1, l_2 and l_3.

To further improve the performance of T-junctions in the parallel feeding networks, more geometric parameters are introduced for impedance matching, which is displayed in Figure 5.3(b). The curved wall and three metallic posts are able to change the impedance and phase condition of the T-junction, which is represented by an equivalent circuit in Figure 5.4. The horizontal position of metallic post a_1 (represented by l_1) is set to control the power ratio between Port 2 and Port 3, and the curved wall is loaded for reducing the reflection to Port 1. By tuning l_1, electric power is allocated with certain ratio between the two output ports. To further improve the return loss of Port 1, the curved wall moves along with a_1 in the tuning process instead of a fixed one in the center of T-junction [51]. The horizontal position of a_2 and a_3 (represented by l_2) determines the phase difference between the two output ports. Then by tuning l_2, the function of phase shifting is achieved. However, the phase and amplitude tuning is limited by the S_{11} of Port 1, which cannot reach a decent value (-10 dB or lower) as the power ratio or phase difference increases. Therefore, one more parameter is employed to improve return loss. As is shown in Figure 5.4, the input impedance is mainly influenced by Z_1, Z_2, and Z_3. To improve the total impedance matching condition, vertical movement of posts a_2 and a_3 (represented by l_3) is introduced to tune Z_2 and Z_3 simultaneously for improving the impedance matching condition. By doing so, the effective tuning range of both amplitude and phase is enlarged.

Figure 5.5 displays the amplitude, phase and S_{11} with different l_3. By shifting this parameter around, most of points in the tuning range can be covered by an S_{11} lower than -10 dB. In all, the proposed T-junction has a dynamic range of (-10, 10) dB in amplitude tuning and (-180,180) degree in phase tuning for the two output ports. And the SIW feeding network based on these T-junctions is suitable for arbitrary amplitude and phase allocation on the output ports.

5.2.3 Design procedure

According to the algorithm and the component design method discussed above, a design procedure of the NFMF array for polarization diversity is presented and discussed in this section. The block diagram is shown in Figure 5.6.

At first, the polarization direction needs to be defined besides the location, amplitude and phase condition of each focal point, which is different from the previous procedures.

For the second step, the focal points are regrouped or reformed, which depends on their target polarization conditions. According to (5.4), focal points with arbitrary polarization can be converted to two groups of focal points with vertical and horizontal polarization, respectively.

The third step is related to the selection of antenna type and building up the corresponding field model by introducing the infinitesimal dipole model, which is similar to the previous procedures.

```
  ┌──────────────────────┐
  │  Location, amplitude, │
  │ phase, and polarization│
  │    of focal points    │
  └──────────────────────┘
            │
  ┌──────────────────────┐
  │  Covert focal points to V │
  │    or H polarization   │
  └──────────────────────┘
            │
  ┌──────────────────────┐
  │  Antenna type & field  │
  │         model          │
  └──────────────────────┘
            │
  ┌──────────────────────┐
  │   Sub-array type & scale │
  └──────────────────────┘
            │
  ┌──────────────────────┐
  │  Sub-array amplitude    │
  │  weight for X-pol define │
  └──────────────────────┘
            │
  ┌──────────────────────┐
  │  Calculate tuning vector │
  │        T_H & T_V        │
  └──────────────────────┘
            │
  ┌──────────────────────┐
  │      Excitations       │
  └──────────────────────┘
            │
  ┌──────────────────────┐
  │         NFMF           │
  └──────────────────────┘
```

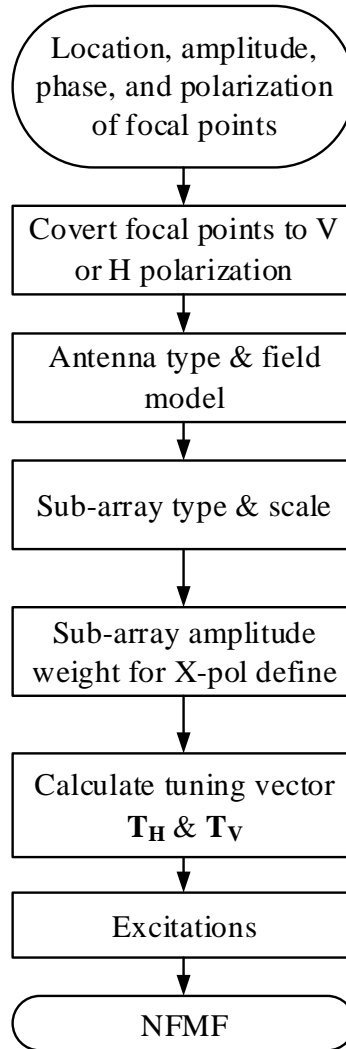Figure 5.6 Block diagram for design NFMF array with polarization diversity.

For the fourth step, the sub-array type and its topology should be selected according to the distribution of the focal points. As mentioned earlier, interwoven or separated array is to be adopted according to the distribution and polarization of focal points. Afterwards, the corresponding scale of each sub-array can be estimated by resolution R.

For the fifth step, the amplitude weight for each sub-array needs to be defined according to the target cross-polarization isolation for each focal point or direction.

With the data and model derived above, the tuning factor for the two groups of focal points is derived by (5.3) or (5.6), which serves as the sixth step of the entire procedure.

Then, the excitations of each sub-array can be estimated by $[C_V][T_V]$ for vertical sub-array and $[C_H][T_H]$ for horizontal sub-array. Moreover, the pattern of NFMF with polarization diversity can be estimated and prepared for further applications.

5.3 Polarization diversity

According to the discussion in the last section, an NFMF with polarization diversity can be realized with the help of the proposed algorithm and the corresponding design method formulated above. Furthermore, the detailed features of the focusing phenomenon are shown and discussed in this section.

5.3.1 Multi-targets and multi-areas

It is demonstrated that the multi-focus at discrete points or continuous areas can be realized by the NFMF design method in Chapter 4. Therefore, the polarization allocation on multiple points or areas would be realized since the proposed algorithm is developed by expanding the previous algorithm with two orthogonal polarization directions.

The first example shows a case of multi-focus on discrete targets. Three focal points with coordinate (y, z) at $(-3\lambda, 2\lambda)$, $(0\lambda, 2\lambda)$, and $(3\lambda, 2\lambda)$ are assigned with vertically polarized E-field (Figure 5.7(a)) and other three points $(-3\lambda, -2\lambda)$, $(0\lambda, -2\lambda)$, and $(3\lambda, -2\lambda)$ are assigned with horizontal polarization (Figure 5.7(b)). In the following examples, the 0 degree polarization is defined along positive z-direction and then 90 degree polarization is along positive y-direction. This case is realized by an 8×8 interwoven array with a spacing of 0.5λ between antennas. The results show that on each focal point the E-field is regulated with the corresponding polarization.
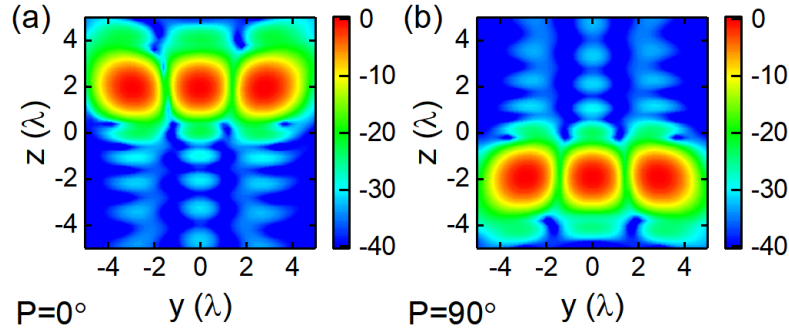
Figure 5.7 NFMF on multiple targets with orthogonal polarizations at plane $x = -8\lambda$: (a) E-field components along horizontal direction; (b) E-field components along vertical direction.
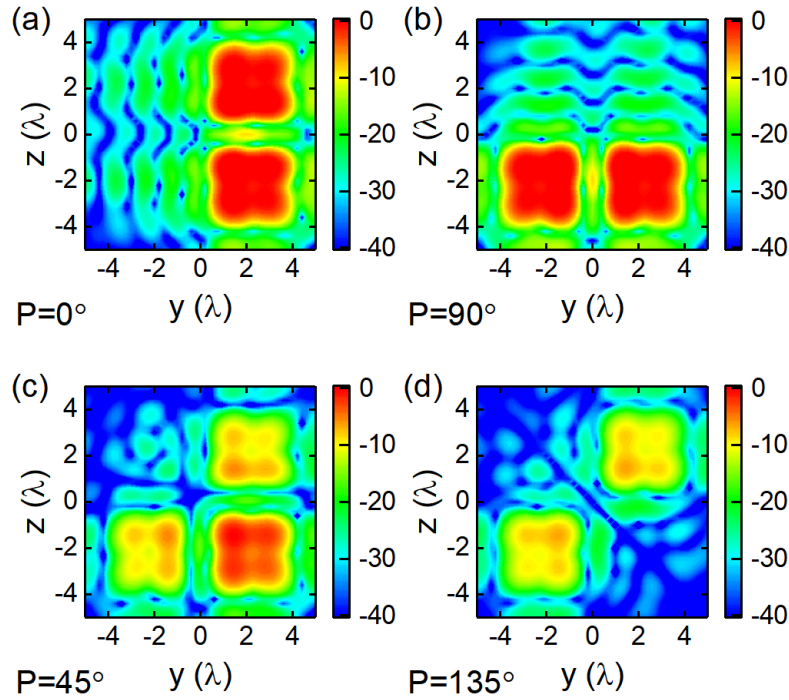
Figure 5.8 Normalized E-fields of NFMF on triple square regions with horizontal, vertical and 45° polarization respectively at $x = -8\lambda$: (a) E-field component along horizontal direction; (b) E-field component along vertical direction; (c) E-field component along 45° direction; (d) E-field components along 135° direction.

Another example is the case of multi-areas. Three square areas with a side length of 2λ are assigned as focal areas. Centers of these areas are located with a coordinate (y, z) at $(-2\lambda, -2\lambda)$, $(2\lambda, 2\lambda)$, and $(2\lambda, -2\lambda)$ with horizontal, vertical and 45° polarization, respectively. In each focal area, the

amplitude and phase are uniformly distributed. Among three areas, the vertical and horizontal polarized areas have a normalized amplitude (0 dB), and the 45° polarized area is constructed by superimposing vertical and horizontal polarized E-field with normalized amplitude. A 16×16 interwoven array with 0.5λ spacing is adopted in this case. Figure 5.8 shows the E-field components along horizontal, vertical, 45° and 135° direction. On each focal area, the polarization direction is coincident with the assigned value with cross-polarization isolation lower than -37.6 dB. Two examples discussed above demonstrate that the proposed method features multi-focus with arbitrary polarization for both discrete points and continuous regions. It is worth mentioning that the antenna array regulated by the proposed method is promising for developing the frontend of a duplex system as it can focus at multiple locations or areas with orthogonal polarizations simultaneously.

5.3.2 Cross-polarization control

As it was discussed in section 5.1.2, SLL of a field pattern affects the cross-polarization isolation of focal points or focal areas. Therefore, a two-dimensional array which is modulated by different amplitude weights is discussed and compared for cross-polarization controlling in this section.

With the help of a 16×16 interwoven array with 0.5λ spacing, a multi-focus case of two square focal areas is realized. One focal area is located at $(2\lambda, 2\lambda)$ with a side length of 2λ, which acts as a horizontal polarized area; and the other area is located at $(-2\lambda, -2\lambda)$ with the same side length, where the E-field is vertically polarized. Both areas are -8λ away from the planar array. By adopting several types of weights, patterns with different cross-polarization conditions are shown in Figure 5.9.

According to the cross-polarization isolation data in Table 5.1, we can draw a similar conclusion with that shown in section 5.1.2. The uniform array has the clearest edge of focal areas, but having the highest level side-lobe, which leads to cross-polarization isolation of -42.8 dB on average (Figure 5.9(a)). The Dolph-Chebyshev arrays with the side-lobe parameter of -20 and -40 dB are simulated and shown in Figure 5.9(b) and 5.9(c), respectively. A better isolation performance of cross-polarization is obtained with lower side-lobe effects, which is -43.0 dB and -63.6 dB on average, respectively.
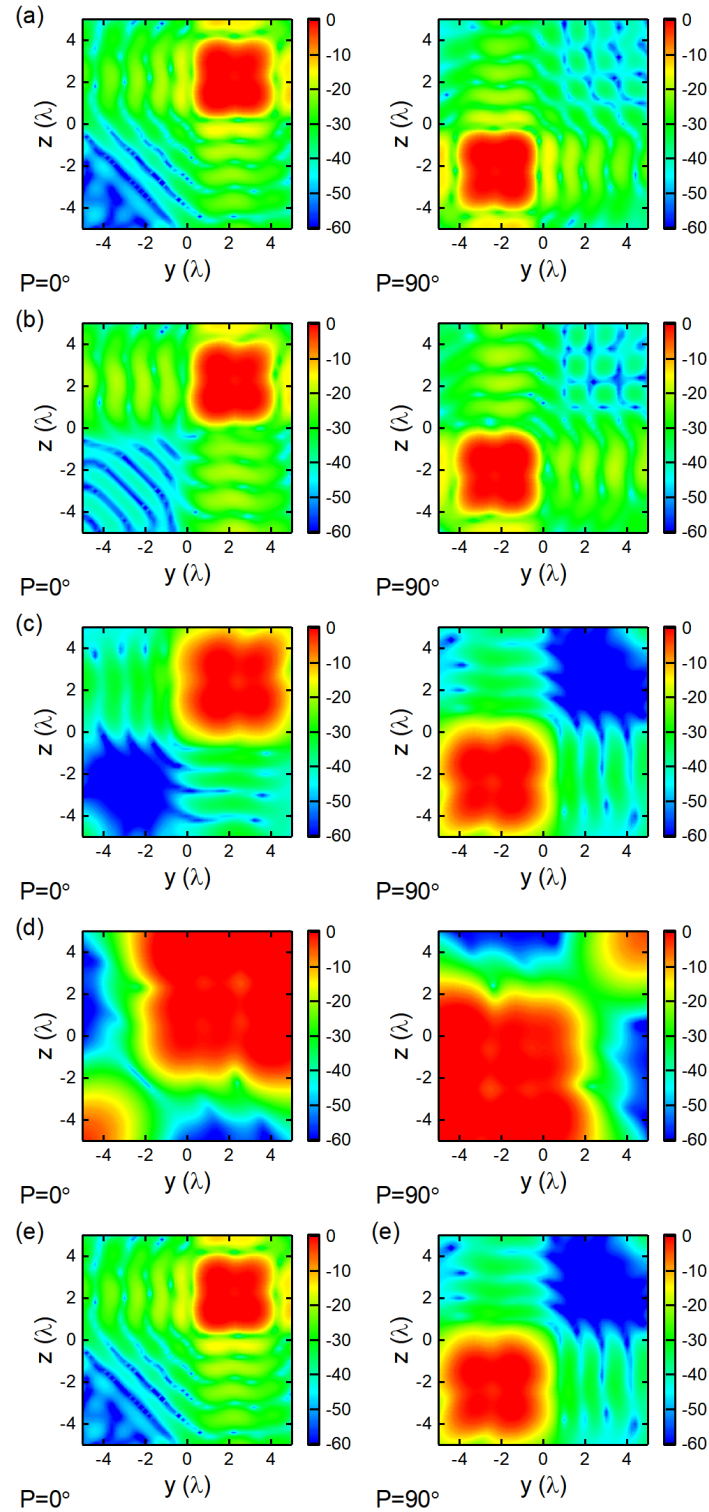
Figure 5.9 NFMF array focuses on two square areas having orthogonal polarizations with different amplitude weights: (a) uniform; (b) Dolph-Chebyshev with -20 dB SLL; (c) Dolph-Chebyshev with -40 dB SLL; (d) binomial; (e) hybrid (uniform and Dolph-Chebyshev with -40 dB SLL).

However, the focal area is extended when we decrease the side-lobe parameter, and it finally becomes a problem when we look into the case of a binomial array (Figure 5.9(d)). It is known that the binomial weight leads to a pattern with zero SLL and the widest main lobe simultaneously. It decreases the focal resolution of NFMF, especially when the focal points are distributed with a compact topology, which leads to a degraded polarization isolation of -22.7 dB on average. Therefore, a trade-off between cross-polarization isolation and resolution needs to be considered in the development of an antenna array.

Furthermore, an antenna array with hybrid weights is shown and presents a solution to balance the two aspects. As it is shown in Figure 5.9(e), a uniform weight is adopted for the vertically polarized area and a Dolph-Chebyshev weight with -40 dB SLL is adopted for the horizontally polarized area. The results show that the upper focal area features a clearer edge with better cross-polarization isolation, and the lower focal area has a blur edge with worse cross-polarization isolation. Similar adjustments can be made according to the specified requirement for different focal areas or points.

Table 5.1 Cross-polarization on $x = -8\lambda$ (Unit: dB)

Case	Uniform	Dolph-Chebyshev SLL = -20 dB	Dolph-Chebyshev SLL = -40 dB	Binomial	Hybrid
X-pol. H	-40.6	-40.3	-65.2	-22.6	-40.2
X-pol. V	-44.9	-45.6	-62.0	-22.8	-61.9

5.4 Fabrication and experiments

To further demonstrate and validate the proposed method, an experiment work is carried out in our Poly-Grames Research Center. The general architecture of the antenna array was discussed earlier, including the dually-polarized antenna array and corresponding feeding networks. A multi-focus case involving two focal points is prepared for the experimental demonstration, where one point is located at $(0, -2\lambda)$ with 45° polarized E-field and another point at $(0, 2\lambda)$ with 135° polarized E-field. Both points are -8λ away from the broadside of the NFMF array. Considering the scale of focal points and their spatial locations, a 4×4 interwoven antenna array is adopted. Antennas in this

array are all back-fed patch antenna operating at 28 GHz and the following experiment is also carried out at the same frequency (Figure 5.10).
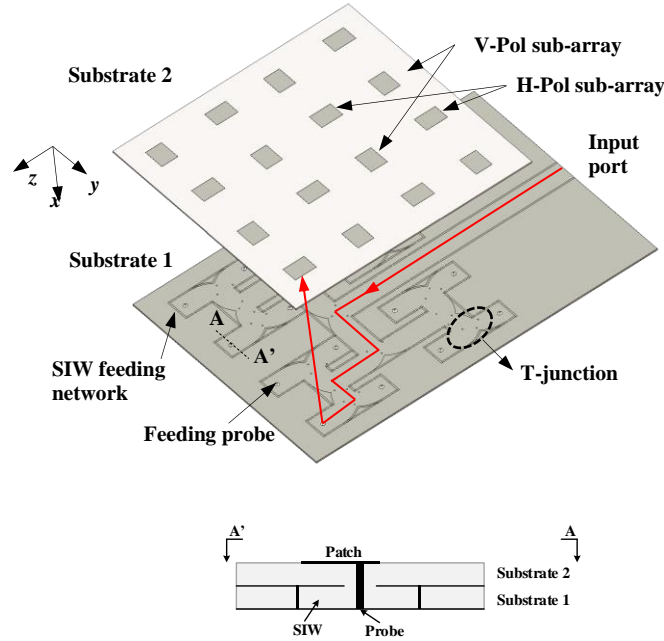
Figure 5.10 4×4 interwoven array and the corresponding SIW feeding networks.

As discussed in the previous chapters, the quasi-analytical field model of single antenna is estimated and applied for calculating the excitations with the help of the infinitesimal dipole equivalent model. Calculation results in Figure 5.14(a) and Table 5.2 are derived by the proposed algorithm with the help of Matlab, where the antenna array is estimated by the infinitesimal dipole model and fed by the ideal excitations calculated through (5.6).

Subsequently, the excitations serve as the reference for the output power allocation of the SIW feeding network. Each antenna is fed by the corresponding output port of the feeding network through a vertically loaded metallic pin, which is shown in Figure 5.10. Then, the feeding network and antenna array are modeled and simulated with CST Microwave Studio, and the simulation results are shown in Figure 5.14(b) and Table 5.2.

According to the process described above, an experimental prototype of the selected NFMF array is fabricated, which is shown in Figure 5.11. The top layer of the prototype is the dually-polarized patch array working at 28 GHz, which is fabricated on RT/duroid® 6002 with a thickness of 10

mils. The bottom layer is prepared for the improved distributed feeding network, where RT/duroid® 6006 (10 mils) is used as the substrate for better phase-shifting performance. Metallic wires are soldered vertically through two layers as the feeding pins of the back-fed configuration.

(a)   (b)

Figure 5.11 Prototype of 4×4 NFMF array: (a) top layer for dual-polarization array; (b) bottom layer for improved distributed feeding network.
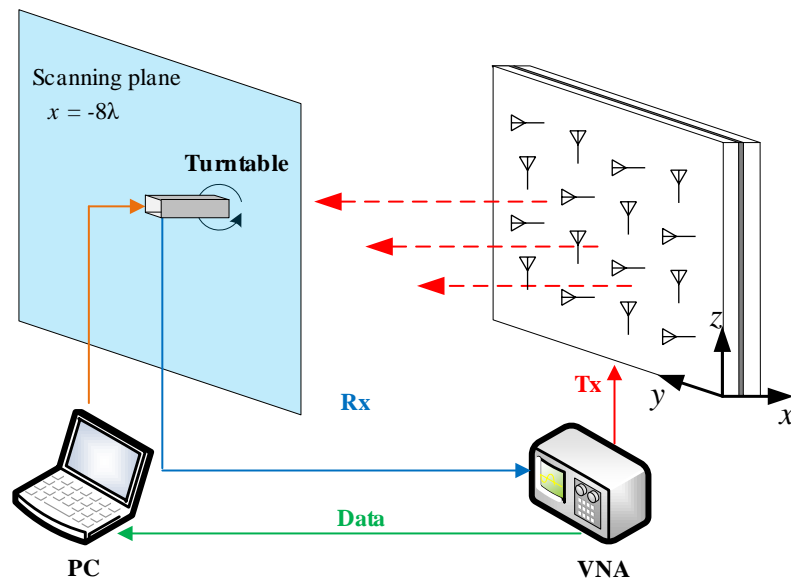
Figure 5.12 Schematic of dual-polarization test of NFMF array.
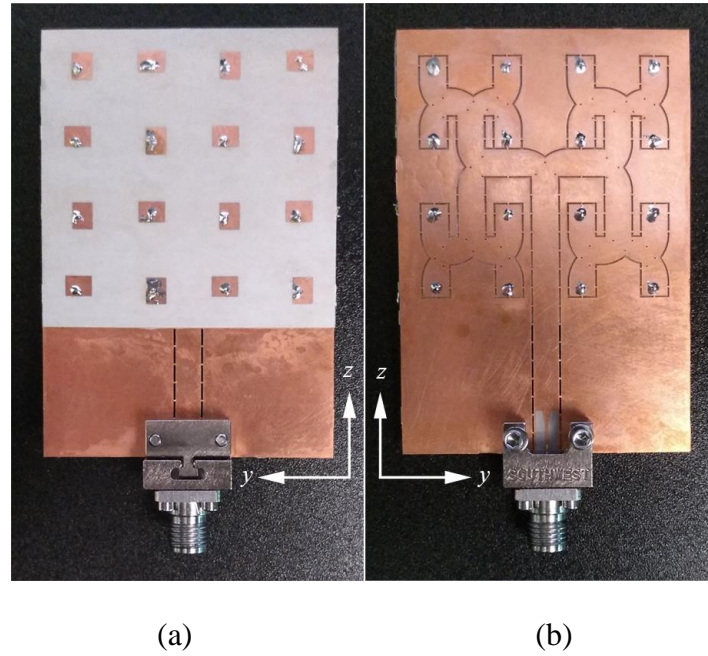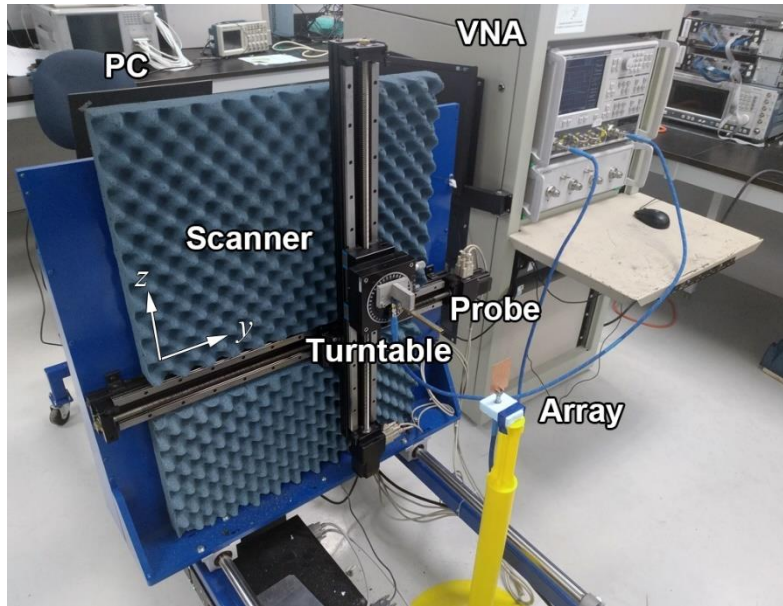
Figure 5.13 Configuration of the testing platform and the installation of NFMF array.

Based on the designed model, the prototype is tested by our near-field testing platform, which is described in Figure 5.12 and 5.13. A probe station is controlled by a motion controller for E-field scanning along the yz plane in the near-field region with a step of 0.18λ (2 mm) along both the y- and z-direction. A waveguide-form probe operating at Ka band is adopted for the vertical and horizontal E-field probing, the direction of field collection can be controlled by the turntable located behind the probe. Field data in different directions are collected by VNA Anritsu 37369D and then transferred to PC for post-processing. The 45° and 135° polarized E-field components are calculated by the data of vertical and horizontal E-field components through the test results (Figure 5.14(c)).

Table 5.2 lists the spatial location, focal width, polarization direction, and cross-polarization isolation of the calculation, simulation, and measurement, respectively. The tested E-component of the 45° polarized focal point located at $(0, -2\lambda)$ has a deformation when compared with its calculated and simulated counterparts, which is mainly caused by the disturbance of the extended SIW feedline and 2.92 mm connector shown in Figure 5.11. In addition, it degrades the cross-polarization isolation at the same time. In general, the three different groups of results are coincident with each other, which indicates the accuracy of the proposed method.
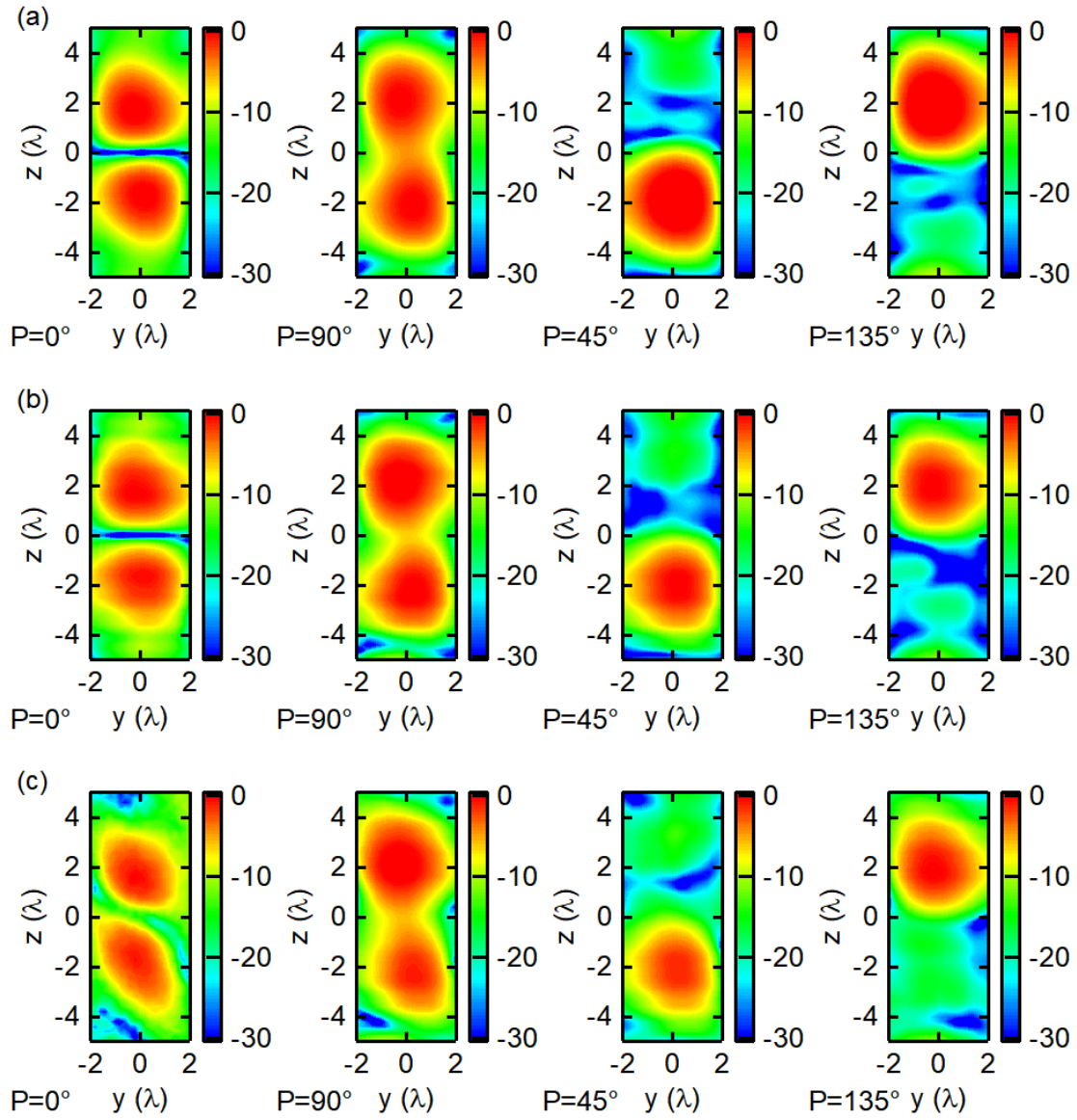
Figure 5.14 NFMF on two discrete focal points with 45° and 135° polarization respectively: (a) Calculation results of E-field components along different directions; (b) Simulation results of E-field components along different directions; (c) Experimental results of E-field components along different directions.

Table 5.2 NFMF with polarization diversity on $x = -8\lambda$

	Location (λ)	Focal width (λ)	Pol. direction (°)	X-pol. Isolation (dB)
Calculation	(0,-2)	2.4	45	-26.3
	(0,2)	2.4	135	-26.7
Simulation	(0,-2)	2.2	45	-23.0
	(0,2)	2.2	135	-21.4
Test	(0.2,-2)	2.1	45	-16.1
	(-0.2,1.8)	2.2	135	-19.0

5.5 Conclusion

In this chapter, we have proposed, studied and validated theoretically and experimentally a method including the algorithm, antenna array and circuit design for an effective NFMF development featuring polarization allocation.

With the improved conjugate-phase approach proposed in this chapter, a polarization allocation on multiple points and areas in the near-field region is realized. This technique is demonstrated as a method of polarization diversity in the near-field region, and features controllable cross-polarization isolation. It is promising for a wide range of applications such as RF frontend of duplex system with multi-users in LoS range and massive MIMO in 5G networks.

CHAPTER 6   CONCLUSIONS AND FUTURE WORK

In this research work, several methods for the multi-focus technique are proposed, studied, and developed with aim at a wide range of explorations of the near-field region. Detailed investigations of different features of multi-focus are carried out through both theoretical and experimental aspects and also the multi-focusing functions are effectively demonstrated with attractive characteristics.

The first contribution of this work is the investigation and development of algorithms for NFMF. In this work, four types of algorithms are developed for constructing the near-field antenna array for NFMF. In the first algorithm, the conjugate-phase approach, a classical approach for defining the excitations of the antenna array for single-point focusing in the near-field region, is improved by introducing a principle of superposition. With these two theories, the pattern for a multi-focus condition is converted to a superposition of patterns, where each pattern converges at one focal point. However, the near-field pattern cannot be fully estimated in a more accurate manner without an effective antenna model in the near-field region. Therefore, an infinitesimal dipole model is introduced as a quasi-analytical field model for estimating the near-field pattern with a high accuracy. With this analytical method, the excitations of the antenna array and the corresponding near-field pattern can be estimated rapidly with high accuracy.

The second algorithm is developed and stemmed from the first algorithm, called element tuning-based algorithm. In this algorithm, the amplitude of each excitation for antenna element can be tuned for near-field pattern adjusting and optimizing purpose. Compared with the first algorithm, the amplitude and phase condition around the focal points can be specified, which performs as an approach for pattern shaping around multiple discrete points. The optimization process is carried out by introducing iterative optimization method.

The third algorithm developed in this work is called a pattern tuning-based algorithm. Different from the element tuning-based algorithm, this algorithm aims at tuning the patterns for single focal points that are ready to be superimposed for NFMF. Therefore, by defining the location and complex field value of focal points, the excitations of each antenna array can be calculated directly without introducing any kind of iterative optimization method. Therefore, this algorithm is suitable for estimating the NFMF with a large number of focal points. Moreover, it is further extended for

defining multiple focal areas with specified shape, amplitude and phase distribution, which go beyond the pattern shaping. Therefore, the algorithm upgrades the NFMF research as a novel way of spatial signal processing in a short range.

The fourth algorithm is an extension of the third algorithm by accommodating a function of polarization diversity. The previous algorithms are valid for antenna array having an identical polarization. Under this circumstance, the third algorithm is further improved with a function of polarization allocation of multiple focal points. A hybrid antenna array is introduced and studied, and corresponding equations are developed for defining the polarization of focal points on arbitrary directions. With this algorithm, the antenna array can realize a multi-focus with specified location, amplitude, phase and polarization, which makes it more convenient to be applied in the current and future wireless systems.

The second contribution of the thesis research is related to the design method of components and RF sub-systems. In the research work, the feeding networks for RF and millimeter-wave bands are studied and developed, respectively, which fulfill the requirements of different bands. Microstrip line-based feeding networks are developed with a combination of Pi networks, which is designed and demonstrated in X-band. Two types of SIW based feeding networks are designed and tested in Ka band with a parallel feeding topology. The end-loaded feeding is suitable for feeding networks with small scale and compact size with multiple layers, while the distributed feeding fits the condition of large-scale feeding networks. All the feeding networks developed in this work can offer unequal amplitude and phase conditions to multiple output ports simultaneously to fulfill the requirement of NFMF. Moreover, a hybrid antenna array with interwoven topology is proposed and studied for polarization diversity in NFMF. With this antenna array, the performance of multi-focus is improved when a large number of focal points with different polarizations are allocated compactly in space.

The third contribution is concerned with the investigation of the properties of NFMF. In order to explore the capabilities of NFMF of certain antenna array, the parameters called near-field AF and focusing resolution are proposed and demonstrated through rigorous theories and analyses. With these parameters, the minimum scale of antenna array for NFMF with certain focal point distributions can be estimated, which allows creating an effective reference for designing NFMF arrays. Moreover, the properties of NFMF itself are also investigated in detail. The conventional

problem of the focal shift in NFF can be improved by applying the proposed element tuning-based algorithm. In the polarization diversity of NFMF, the cross-polarization level can be controlled by introducing a set of amplitude weights to entire array.

The fourth contribution is related to the extension of the functions and applications of NFMF. As mentioned above, the NFMF is not limited to a multi-beam technique when it is developed with the proposed algorithms. Due to its flexibility of pattern definition, it would play a role as an interesting approach of pattern shaping in the near-field region. Moreover, spatial power combining, power splitting, and phase shifting can be realized by the proposed NFMF arrays, which serve as a new wireless technique called spatial signal processing. In addition, this technique is promising for signal synchronization and power supply for a largely scaled system such as massive MIMO because of its focusing ability on a large number of targets distributed spatially. As the algorithm developed is universal with the principle of interference of waves, the proposed algorithms can be applied to others physical areas such as acoustic and optical communications.

However, the research work also has its own constrains, which may serve as a reference for the further work of NFMF.

Mutual coupling is an essential problem in developing array theories and in designing practical antenna arrays. This is also an important aspect of the research of NFMF. In future work, the mutual coupling issue should be considered in estimating and evaluating the near-field pattern of NFMF for a more accurate solution.

As the design and test in X-band and Ka-bands are carried out, NFMF is promising for its practical realizations in higher frequency bands such as sub-THz and THz. Therefore, component design techniques including arrays and feeding networks should be studied and developed, and the corresponding algorithms may be adjusted and improved for higher frequency applications.

As the proposed algorithms are of rapid speed for estimating the excitations and near-field patterns, it may be suitable as an approach for multi-target locating and real-time tracing, which would require further developments and refinements in connection with NFMF algorithms and corresponding hardware components.

REFERENCES

[1] N. Hassan and X. Fernando, "Massive MIMO wireless networks: An overview," *Electronics,* vol. 6, p. 63, 2017.

[2] V. Jungnickel, K. Manolakis, W. Zirwas, B. Panzner, V. Braun, M. Lossow*, et al.*, "The role of small cells, coordinated multipoint, and massive MIMO in 5G," *IEEE Communications Magazine,* vol. 52, pp. 44-51, 2014.

[3] W. Cheng-Xiang, F. Haider, G. Xiqi, Y. Xiao-Hu, Y. Yang, Y. Dongfeng*, et al.*, "Cellular architecture and key technologies for 5G wireless communication networks," *Communications Magazine, IEEE,* vol. 52, pp. 122-130, 2014.

[4] A. Kay, "Near-field gain of aperture antennas," *IRE Transactions on Antennas and Propagation,* vol. 8, pp. 586-593, 1960.

[5] R. Hansen, "Focal region characteristics of focused array antennas," *IEEE transactions on antennas and propagation,* vol. 33, pp. 1328-1337, 1985.

[6] A. Buffi, P. Nepa, and G. Manara, "Design criteria for near-field-focused planar arrays," *IEEE Antennas and Propagation Magazine,* vol. 54, pp. 40-50, 2012.

[7] P. Nepa and A. Buffi, "Near-Field-Focused Microwave Antennas: Near-field shaping and implementation," *IEEE Antennas and Propagation Magazine,* vol. PP, pp. 1-1, 2017.

[8] C. G. Wade, N. Šibalić, N. R. de Melo, J. M. Kondo, C. S. Adams, and K. J. Weatherill, "Real-time near-field terahertz imaging with atomic optical fluorescence," *Nature Photonics,* vol. 11, p. 40, 11/07/online 2016.

[9] R. I. Stantchev, B. Sun, S. M. Hornett, P. A. Hobson, G. M. Gibson, M. J. Padgett*, et al.*, "Noninvasive, near-field terahertz imaging of hidden objects using a single-pixel detector," *Science Advances,* vol. 2, 2016.

[10] S. Karimkashi and A. A. Kishk, "Focused Microstrip Array Antenna Using a Dolph-Chebyshev Near-Field Design," *IEEE Transactions on Antennas and Propagation,* vol. 57, pp. 3813-3820, 2009.

[11] S. Karimkashi, "Characteristics of different focusing antennas in the near field region," University of Mississippi, 2011.

[12] T. Isernia, P. D. Iorio, and F. Soldovieri, "An effective approach for the optimal focusing of array fields subject to arbitrary upper bounds," *IEEE Transactions on Antennas and Propagation,* vol. 48, pp. 1837-1847, 2000.

[13] D. A. M. Iero, L. Crocco, and T. Isernia, "Constrained power focusing of vector fields: an innovative globally optimal strategy," *Journal of Electromagnetic Waves and Applications,* vol. 29, pp. 1708-1719, 2015/09/02 2015.

[14] J. Álvarez, R. G. Ayestarán, G. León, J. A. López-Fernández, and F. Las-Heras, "Phase optimization for near field focus on simultaneous targets using antenna arrays," in *Antennas and Propagation (EUCAP), 2012 6th European Conference on*, 2012, pp. 2779-2783.

[15] J. Alvarez, R. Ayestarán, and F. Las-Heras, "Design of antenna arrays for near-field focusing requirements using optimisation," *Electronics letters,* vol. 48, pp. 1323-1325, 2012.

[16] J. Álvarez, R. G. Ayestarán, G. n. León, L. F. Herrán, A. Arboleya, J. s. A. López-Fernández*, et al.*, "Near field multifocusing on antenna arrays via non-convex optimisation," *IET Microwaves, Antennas & Propagation,* vol. 8, pp. 754-764, 2014.

[17] J. Álvarez, R. G. Ayestarán, G. León, J. A. López-Fernández, L. F. Herrán, and F. Las-Heras, "Optimization framework on antenna arrays for near field multifocusing," in *Proceedings of the 2012 IEEE International Symposium on Antennas and Propagation*, 2012, pp. 1-2.

[18] J. Á. Muñiz, R. G. Ayestarán, J. Laviada, and F. Las‑Heras, "Support vector regression for near‑field multifocused antenna arrays considering mutual coupling," *International Journal of Numerical Modelling: Electronic Networks, Devices and Fields,* vol. 29, pp. 146-156, 2016.

[19] R. G. Ayestarán, "Fast Near-Field Multifocusing of Antenna Arrays Including Element Coupling Using Neural Networks," *IEEE Antennas and Wireless Propagation Letters,* vol. 17, pp. 1233-1237, 2018.

[20] Y. F. Wu and Y. J. Cheng, "Proactive Conformal Antenna Array for Near-Field Beam Focusing and Steering Based on Curved Substrate Integrated Waveguide," *IEEE Transactions on Antennas and Propagation,* vol. 67, pp. 2354-2363, 2019.

[21] W. M. Hassan, S. H. Zainud-Deen, and H. A. Malhat, "Multi-focus transmitarray antenna in near/far field design," in *2016 33rd National Radio Science Conference (NRSC)*, 2016, pp. 17-24.

[22] K. T. Selvan and R. Janaswamy, "Fraunhofer and Fresnel Distances : Unified derivation for aperture antennas," *IEEE Antennas and Propagation Magazine,* vol. 59, pp. 12-15, 2017.

[23] C. H. Wilcox, "An expansion theorem for electromagnetic fields," *Communications on Pure and Applied Mathematics,* vol. 9, pp. 115-134, 1956.

[24] S. M. Mikki and Y. M. M. Antar, "A Theory of Antenna Electromagnetic Near Field—Part I," *IEEE Transactions on Antennas and Propagation,* vol. 59, pp. 4691-4705, 2011.

[25] S. M. Mikki and Y. M. M. Antar, "A Theory of Antenna Electromagnetic Near Field—Part II," *IEEE Transactions on Antennas and Propagation,* vol. 59, pp. 4706-4724, 2011.

[26] W. C. Chew, *Waves and Fields in Inhomogeneous Media*: Van Nostrand Reinhold, 1990.

[27] T. B. Hansen and A. D. Yaghjian, *Plane-Wave Theory of Time-Domain Fields: Near-Field Scanning Applications*: Wiley, 1999.

[28] P. Petre and T. K. Sarkar, "Planar near-field to far-field transformation using an equivalent magnetic current approach," *IEEE Transactions on Antennas and Propagation,* vol. 40, pp. 1348-1356, 1992.

[29]   P. Petre and T. K. Sarkar, "Planar near-field to far-field transformation using an array of dipole probes," *IEEE Transactions on Antennas and Propagation,* vol. 42, pp. 534-537, 1994.

[30]   F. Las-Heras, B. Galocha, and J. L. Besada, "Equivalent source modelling and reconstruction for antenna measurement and synthesis," in *IEEE Antennas and Propagation Society International Symposium 1997. Digest*, 1997, pp. 156-159 vol.1.

[31]   F. L. Heras and C. Ortiz-Valbuena, "Antenna diagnosis and pattern reconstruction using near field amplitude data and iterative source reconstruction," in *IEEE Antennas and Propagation Society International Symposium. 1998 Digest. Antennas: Gateways to the Global Network. Held in conjunction with: USNC/URSI National Radio Science Meeting (Cat. No.98CH36*, 1998, pp. 1343-1346 vol.3.

[32]   T. S. Sijher and A. A. Kishk, "Antenna modeling by infinitesimal dipoles using genetic algorithms," *Progress In Electromagnetics Research,* vol. 52, pp. 225-254, 2005.

[33]   S. Clauzier, S. M. Mikki, and Y. M. M. Antar, "Design of Near-Field Synthesis Arrays Through Global Optimization," *IEEE Transactions on Antennas and Propagation,* vol. 63, pp. 151-165, 2015.

[34]   J. Laurin, J. Zurcher, and F. E. Gardiol, "Near-field diagnostics of small printed antennas using the equivalent magnetic current approach," *IEEE Transactions on Antennas and Propagation,* vol. 49, pp. 814-828, 2001.

[35]   R. W. Bickmore, "ON FOCUSING ELECTROMAGNETIC RADIATORS," *Canadian Journal of Physics,* vol. 35, pp. 1292-1298, 1957/11/01 1957.

[36]   G. Borgiotti, "Maximum power transfer between two planar apertures in the Fresnel zone," *IEEE Transactions on Antennas and Propagation,* vol. 14, pp. 158-163, 1966.

[37]   D. A. Hill, "A Numerical Method for Near-Field Array Synthesis," *IEEE Transactions on Electromagnetic Compatibility,* vol. EMC-27, pp. 201-211, 1985.

[38]   M. Narasimhan and B. Philips, "Synthesis of near-field patterns of arrays," *IEEE Transactions on Antennas and Propagation,* vol. 35, pp. 212-218, 1987.

[39]   R. Liu and K. Wu, "Antenna Array for Amplitude and Phase Specified Near-Field Multifocus," *IEEE Transactions on Antennas and Propagation,* vol. 67, pp. 3140-3150, 2019.

[40]   R. Liu, Y. Zhao, and K. Wu, "Millimeter-wave sourceless receiver embedded with DoA estimation," in *2016 46th European Microwave Conference (EuMC)*, 2016, pp. 69-72.

[41]   K. Morimoto, J. Hirokawa, and M. Ando, "Design of a 180-Degree Single-Layer Divider to control Sidelobe and Crossover Levels in Butler-Matrix Beam-Switching Antenna," in *2007 Asia-Pacific Microwave Conference*, 2007, pp. 1-4.

[42]   Y. J. Cheng, W. Hong, and K. Wu, "Broadband Self-Compensating Phase Shifter Combining Delay Line and Equal-Length Unequal-Width Phaser," *IEEE Transactions on Microwave Theory and Techniques,* vol. 58, pp. 203-210, 2010.

[43]   T. Yang, M. Ettorre, and R. Sauleau, "Novel Phase Shifter Design Based on Substrate-Integrated-Waveguide Technology," *IEEE Microwave and Wireless Components Letters,* vol. 22, pp. 518-520, 2012.

[44] K. Sellal, L. Talbi, and M. Nedil, "Design and implementation of a controllable phase shifter using substrate integrated waveguide," *IET Microwaves, Antennas & Propagation,* vol. 6, pp. 1090-1094, 2012.

[45] E. Sbarra, L. Marcaccioli, R. V. Gatti, and R. Sorrentino, "Ku-band analogue phase shifter in SIW technology," in *2009 European Microwave Conference (EuMC)*, 2009, pp. 264-267.

[46] Y. Ding and K. Wu, "SIW varactor-tuned phase shifter and phase modulator," in *2012 IEEE/MTT-S International Microwave Symposium Digest*, 2012, pp. 1-3.

[47] Y. M. Huang, H. Jin, Y. Sun, S. Leng, T. Wang, and G. Wang, "Small-reflected substrate integrated waveguide termination with multi-step shape and absorbing material," in *2017 IEEE International Symposium on Antennas and Propagation & USNC/URSI National Radio Science Meeting*, 2017, pp. 2605-2606.

[48] H. Uchida, M. Nakayama, A. Inoue, and Y. Hirano, "A post-wall waveguide (SIW) matched load with thin-film resistor," in *2010 Asia-Pacific Microwave Conference*, 2010, pp. 1597-1600.

[49] D.-S. Eom and H.-Y. Lee, "An X-band substrate integrated waveguide attenuator," *Microwave and Optical Technology Letters,* vol. 56, pp. 2446-2449, 2014.

[50] R. Liu and K. Wu, "Compact Millimeter-Wave SIW Circuit that Combines Phase-Shifting and Attenuating Functions," in *2019 IEEE MTT-S International Wireless Symposium (IWS)*, 2019, pp. 1-3.

[51] S. Park, D. Shin, and S. Park, "Low Side-Lobe Substrate-Integrated-Waveguide Antenna Array Using Broadband Unequal Feeding Network for Millimeter-Wave Handset Device," *IEEE Transactions on Antennas and Propagation,* vol. 64, pp. 923-932, 2016.

[52] C. L. Dolph, "A Current Distribution for Broadside Arrays Which Optimizes the Relationship between Beam Width and Side-Lobe Level," *Proceedings of the IRE,* vol. 34, pp. 335-348, 1946.

[53] R. G. Lyons, *Understanding Digital Signal Processing*: Prentice Hall, 2011.

[54] Y. Miura, J. Hirokawa, M. Ando, Y. Shibuya, and G. Yoshida, "Double-Layer Full-Corporate-Feed Hollow-Waveguide Slot Array Antenna in the 60-GHz Band," *IEEE Transactions on Antennas and Propagation,* vol. 59, pp. 2844-2851, 2011.